



NATIONAL OPTICAL ASTRONOMY OBSERVATORY



NSF Research Experiences for Undergraduates

Site Program in Astronomy at
Kitt Peak National Observatory (KPNO)
(AST 1262829)

Student Final Research Reports 2013



December 2, 2013

RESOLVE'd AGN: Refining Active Galactic Nuclei Classification Techniques

Aida Behmard, Dara Norman, RESOLVE Team
Kitt Peak Nat'l Observatory REU Program

Abstract

We used multi-wavelength methods to select a sample of nearby Active Galactic Nuclei (AGN) for further environmental study. Data from the RESOLVE survey, a volume-limited census within $<50,000$ cubic Mpc (Kannappan et al. 2013), was merged with Wide-Field Infrared Survey Explorer (WISE) data and the Sloan Digital Sky Survey (SDSS) DR7 re-release to identify AGN in the nearby ($z \sim 0.02$) cosmic web. The volume-limited nature of RESOLVE is of particular interest as it allows for close examination of AGN environments and fueling mechanisms. We identified a group of objects that are classified as star forming galaxies with the Baldwin-Phillips-Terlevich diagnostic diagram, but have mid-IR colors that suggest they may be AGN. The ambiguous nature of these objects makes them interesting targets for further investigation.

I. INTRODUCTION

Active galactic nuclei are highly compact central regions of galaxies that emit enormous amounts of energy. Tight correlation between black hole mass and bulge velocity dispersion indicate the presence of a massive central object, widely considered to be a supermassive black hole powered by an accretion disk (Fabian et al. 1999). Due to their extreme luminosity across the electromagnetic spectrum, AGN are used as probes to examine the distant universe.

The mechanics that govern AGN behavior are not well understood. Galaxy mergers are often cited as a common fueling mechanism. Indeed, a number of morphological studies identify post-merger systems in AGN samples (Bahcall et al. 1997; Urrutia et al. 2008; Letawe et al. 2010; Smirnova et al. 2010). Activity such as minor merger frequency, galaxy harassment, and galaxy infall into more dense environments may also trigger AGN activity. The frequencies of such alternative fueling methods are unknown.

Extensive literature supports the idea that AGN are influenced by environment. Ruderman & Ebeling (2005) sampled 508 x-ray point sources (XPSs) detected in Chandra ACIS-I observations. They found that XPS surface density exhibits pronounced excess within 3.5 Mpc of the galaxy cluster centers. The excess is attributed to AGN within the clusters and supports the idea that AGN concen-

tration increases with galaxy density. Kauffman et al. (2004) also report that numbers of AGN vary significantly across different galactic density regimes (K.A. Pimbblet et al. 2013).

Hierarchical simulations suggest that the gravitational processes governing the formation and evolution of galaxy clusters also influence AGN triggering. Confirmation of these simulations requires sampling of AGN at low redshifts. This would allow for close examination of AGN distribution within local environments. We rely upon the RESOLVE survey for selecting a sample of low redshift AGN. Equatorial footprints make matching with other surveys feasible. Sources were selected from the RESOLVE, Sloan Digital Sky Survey (SDSS) data, and Wide-field Infrared Survey Explorer (WISE) data. Obtaining data across different surveys makes utilization of multi-wavelength diagnostic methods possible. By analyzing a sample of volume-limited selected objects, we hope to identify a selection of low redshift AGN whose local environments can be further investigated.

II. DATA AND METHODS

II.1. *The RESOLVE Survey and Matching*

RESOLVE is a volume-limited galactic census of gas, stellar, and dynamical mass in the nearby ($z \sim 0.02$) cosmic web (see Figure 1). It is designed to further investigate low redshift objects

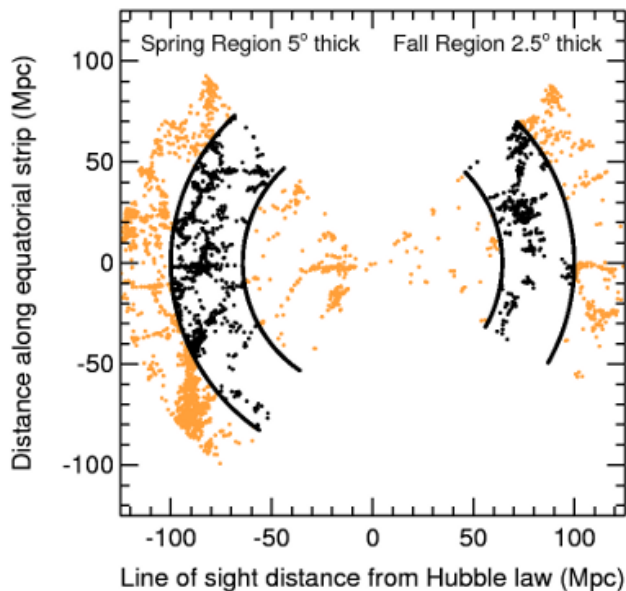


FIG. 1. The RESOLVE survey (black points) is shown within a portion of the larger SDSS Redshift Survey from which it was drawn (orange points). RESOLVE comprises ~ 1600 galaxies in two equatorial strips.

detected in the Sloan Digital Sky Survey (SDSS). This volume-limited survey provides a more accurate census to examine AGN environments. In addition, RESOLVE goes beyond other 3D spectroscopic surveys in several ways:

1. Diverse, contiguous, and uniform local/global environment data.
2. Highly complete selection extending into the gas-dominated dwarf galaxy regime.
3. High-resolution ionized gas or stellar kinematic data for each galaxy and broad 320-725nm spectroscopy with $H\alpha$ and $H\beta$ for disentangling emission, absorption, and extinction.
4. Equatorial footprints enabling synergy with deep photometric surveys (Kannappan et al. 2011).

Such equatorial footprints outlined in black on Figure 1 allow for matching between RESOLVE and Sloan Digital Sky Survey (SDSS) data. SDSS is a flux-limited spectroscopic census that covers over 35% of the sky. It selects for bright objects, providing a robust sample of

AGN candidates whose environments can be examined with RESOLVE counterpart data. Selection from the SDSS DR7 Catalog yielded 2059 objects in our cross-matched RESOLVE+SDSS sample. Objects were matched by RA/DEC position within a 10 arcsec radius. We further culled the 2059 object RESOLVE+SDSS sample by eliminating sources with the following criteria for emission lines:

1. Double negative emission line ratios for either $[OIII]/H\beta$ or $[NII]/H\alpha$
2. $H\alpha$ or $H\beta = 0$.

Further matching was carried out with Wide-field Infrared Survey Explorer (WISE) data. WISE is a NASA infrared-wavelength space telescope that conducted an all-sky astronomical survey in four mid-infrared pass bands (W1: $3.4 \mu\text{m}$, W2: $4.6 \mu\text{m}$, W3: $12 \mu\text{m}$, W4: $22 \mu\text{m}$).

We found there to be 1844 objects in the RESOLVE+SDSS+WISE sample after all criteria was met.

II.2. *Balwin-Phillips-Terlevich (BPT) Diagnostic Diagram*

The most common AGN classification tool in the optical wavelength is the Baldwin-Phillips-Terlevich (BPT) diagram. This diagnostic tool distinguishes between star-forming galaxies and AGN on the basis of their $[O III] \lambda 5007 / H\beta$, $[N II] \lambda 6583 / H\alpha$ flux ratios (Baldwin et al. 1981). We used a BPT diagram to classify the 1844 objects in our RESOLVE+SDSS+WISE sample. This diagram is shown as Figure 2.

Through a combination of stellar population synthesis models and self-consistent photoionization models, Kewley et al. created a maximum starburst line on the BPT diagrams (Kewley et al. 2001, hereafter Ke01). This line is based on the upper limit of the theoretical pure stellar photoionization models.

Kauffman et al. modified the Kewley et al. criteria to establish a composite object-star-forming galaxy line (Kauffman et al. 2003, hereafter Ka03). These selection lines are plotted on the graph in Figure 2.

1. Star-forming galaxies (shown in blue) lie below and to the left-hand side of the Ka03 classification line in the $[\text{NII}]/\text{H}\alpha$ vs. $[\text{OIII}]/\text{H}\beta$ diagram:

$$\log([\text{OIII}]/\text{H}\beta) < 0.61/[\log([\text{NII}]/\text{H}\alpha) - 0.05] + 1.3 \quad (1)$$

2. Composite galaxies (shown in yellow-orange) lie between the Ka03 and Ke01 classification lines on the $[\text{NII}]/\text{H}\alpha$ vs. $[\text{OIII}]/\text{H}\beta$ diagram:

$$0.61/[\log([\text{NII}]/\text{H}\alpha) - 0.05] + 1.3 < \log([\text{OIII}]/\text{H}\beta) \quad (2)$$

$$0.61/[\log([\text{NII}]/\text{H}\alpha) - 0.47] + 1.19 < \log([\text{OIII}]/\text{H}\beta) \quad (3)$$

3. Active galactic nuclei (shown in red) lie above and to the right-hand side of the Ke01 classification line in the $[\text{NII}]/\text{H}\alpha$ vs. $[\text{OIII}]/\text{H}\beta$ diagram:

$$\log([\text{OIII}]/\text{H}\beta) > 0.61/[\log([\text{NII}]/\text{H}\alpha) - 0.47] + 1.19 \quad (4)$$

The full Kewley et al. (2001) and Kauffman et al. (2003) BPT criteria can be found in Kewley et al. (2006).

BPT classification reveals that the RESOLVE+SDSS+WISE sample of 1844 objects is composed of 208 AGN ($\sim 11\%$), 150 composite objects ($\sim 8\%$), and 1486 star-forming galaxies ($\sim 80\%$).

II.3. Mid-Infrared Color Selection

Studies conducted on WISE+SDSS selected sources suggest that WISE colors alone help separate star forming galaxies and composite objects from strong active galactic nuclei (AGNs) and QSOs at $z \leq 3$ (Yan et al. 2013). Yan et al. found that a color-color diagram of WISE pass bands W1-W2 vs. W2-W3 (see Figure 3) provided tentative classification of WISE+SDSS sources.

We compare the Yan et al. WISE+SDSS object mid-infrared characterization results with our RESOLVE+WISE+SDSS sample. The resulting mid-infrared color-color diagram is given in Figure 4 below.

Yan et al. spectroscopically classified their objects in order to identify them on the mid-infrared diagram. Our BPT composite objects

occupy roughly the same areas in both the Yan et al. plot and our RESOLVE+SDSS+WISE sample plot as can be seen through comparison of Figure 3 and Figure 5.

Unlike the composite objects, AGN in the Yan et al. plot and our RESOLVE+SDSS+WISE mid-infrared plot do not occupy similar areas. The Yan et al. plot displays AGN up to $W1-W2 \sim 0.9$ while most RESOLVE+SDSS+WISE AGN are confined to $W1-W2 \sim 0.5$ or lower as can be seen in Figure 6 compared with Figure 3.

We find that the region of the mid-IR color-color plot where Yan et al. find AGN is occupied in our plot by BPT classified star-forming galaxies. We select these sources for further study and refer to them in the rest of the paper as 'ambiguous objects'. These ambiguous objects are highlighted as bold diamonds in Figure 7.

Errors for each ambiguous source were calculated along the W1-W2 axis by adding WISE catalog errors in the W1 and W2 pass bands together in quadrature. In the WISE catalog, pass band errors were taken to be instrumental profile-fit photometry flux uncertainty in magnitude units. These uncertainties are given by $w(1/2/3/4)\text{sigmpro}$ parameter in the WISE database. The pass band uncertainties were calculated by estimating source positions and pass band fluxes for each candidate. Candidate sources and nearby neighbors (i.e. adjacent candidates whose PSF responses overlap significantly with the primary candidate) are grouped into blends and examined with profile-fitting photometry.

Ambiguous objects with errors that fall below the star-forming boundary set by the Yan et al. contour were eliminated from our final ambiguous object selection. Our final sample contains 14 sources. These final 14 sources are over-plotted on the BPT diagnostic diagram in Figure 8 below.

III. ANALYSIS

Because the ambiguous sources are classified as star-forming galaxies by the BPT criteria, but fall in the AGN region of the mid-infrared

plot, they are possibly borderline composite objects. Thus, we expected them to fall in the star-forming region while clustering along the star-forming classification line (Ka03). Then to correctly classify the ambiguous objects, the star-forming line could be adjusted. However, instead we find that the ambiguous sources are scattered within the star-forming region. This suggests that the BPT diagram is a poor classification tool for this particular class of objects.

Visual examination of the ambiguous objects was conducted with optical images from the SDSS DR9 database, three of which are given below in Figure 9.

The left-most image shows a galaxy that is morphologically spiral and blue in color. Both indicate star-forming activity. However, it harbors a bright center suggestive of an AGN. The middle image features a source that is much more morphologically irregular, and features large blue objects. The smaller blue object is classified as a galaxy, and thus could be an AGN contaminant. It is a good candidate for further investigation. Of particular interest is the source located at RA: 146.842, DEC: 0.740839, seen as the right-most image in Figure 8. This object is morphologically elliptical as well as red in color. Red objects generally do not exhibit much current or ongoing star-formation. Additionally, this particular object has a remarkably bright center, strong evidence that the galaxy is active and hosts an AGN. The source falls close to the star-forming empirical line on the BPT diagram. This implies that if the object is an AGN, the BPT diagram may still be a valid classification method, and the star-forming classification line requires adjustment.

This object is proposed to be a dusty AGN candidate. The BPT diagnostic diagram relies upon ratios of optical emission lines to characterize objects. Dependence on optical data makes the BPT method susceptible to dust. In contrast, the mid-infrared diagram is based on infrared observations that cut through dust. Thus, the mid-infrared color-color diagram would classify dusty AGN candidates correctly while the BPT diagnostic diagram would fail for such objects.

IV. CONCLUSIONS

In this study, we used multi-wavelength selection criteria to identify AGN in the RESOLVE survey. We found that the BPT diagnostic diagram and the mid-infrared color-color diagram provided several consistent identifications of our RESOLVE+SDSS+WISE sample. However, we isolated a sample of 14 objects that was inconsistently identified according to the multi-wavelength selection criteria. The inconsistencies could be attributed to the following:

1. **Mid-Infrared Color-Color Diagram Contour Densities:** Our 14 ambiguous objects lie outside the star-forming contour plot on the Yan et al. (2013) diagram. However, we do not have information on the specific contour densities in their plot. If the density of SF galaxies is low in that region, but not zero, it is possible that we should expect 14 star-forming galaxies to lie outside the star-forming contour. In that case, the 14 ambiguous objects would become unambiguous and uninteresting in our study.
2. **Mid-Infrared Color-Color Diagram Contour Overlap:** Yan et al. (2013) found that certain objects populated certain areas on the mid-infrared color-color diagram. These areas are outlined by contours. However, these areas often overlap. Although we classified our ambiguous objects as AGN because they fell in an AGN-occupied area, the ambiguous objects also fill space populated by composite objects and high-redshift ($z \sim 1.2$) QSOs. Because of this, we cannot classify the ambiguous objects as AGN with complete confidence.
3. **WISE Area Sampling:** Source positions in the WISE catalog are determined by sampling small portions of the sky in blends. Because these blends also include surrounding area, contamination from neighboring objects is a risk. Our ambiguous objects might be contaminated by their neighbors. The middle ambiguous object

in Figure 8 may be an example. To ensure that this is not the case, we will analyze optical images for each ambiguous object in the future and verify that they are sufficiently far away from other sources.

4. **Redshift Considerations:** The WISE+SDSS sample used by Yan et al. was not volume-limited and included high redshift objects. A cyan-colored contour for QSOs lying at $z \sim 1.2$ is apparent in the mid-infrared color-color diagram. This contour notably overlaps with the area occupied by the 14 ambiguous objects. Notably, none of our objects lie at higher redshift than $z \sim 0.02$ due to the nature of the RESOLVE survey. The Yan et al. Mid-infrared color-color diagram classification could be skewed by redshift considerations and is inappropriate for our nearby sample.
5. **Dusty AGN:** In order to verify the AGN status of dusty AGN candidates, it is necessary to classify them spectroscopically. If their AGN status is verified, we can conclude that the BPT diagnostic diagram criteria must be adjusted to account for such objects. The next step would be to utilize volume-limited RESOLVE data and analyze the local environments of such dusty

AGN.

We plan to explore all of these possible issues in the future, and continue moving towards our goal of understanding what conditions allow AGN to be born and thrive.

V. ACKNOWLEDGMENTS

I would like to thank Dr. Dara Norman (NOAO) for her wonderful guidance and mentoring throughout the duration of this program. I would also like to thank our collaborators, Drs. Sheila Kannappan and Erik Hoversten (UNC Chapel Hill), Dr. Jillian Bellovary (Vanderbilt University), Angelica Rivera (Vassar College), and the entire RESOLVE team.

This research was supported by the KPNO/NOAO for Undergraduates (REU) Program which is funded by the National Science Foundation Research Experience for Undergraduates Program and the Department of Defense ASSURE program through Scientific Program Order No. 13 (AST-0754223) of the Cooperative Agreement No. AST-0132798 between the Association of Universities for Research in Astronomy (AURA) and the NSF.

-
- [1] Kannappan S., 2013, BAAS, 45, 102.3
 - [2] Yan L., Donoson E., Tsai Chao-Wei, et al., 2013, ApJ, 145, 55
 - [3] Fabian A., Iwasawa K., 1999, MNRAS, 303, L34
 - [4] Bahcall J., et al., 1997, ApJ, 479, 642
 - [5] Urrutia T., et al., 2008, ApJ, 674, 80
 - [6] Letawe Y., Letawe J., Magain P., 2010, MNRAS, 403, 2088
 - [7] Smirnova A.A., Moiseev, A.V., Afanasiev, V.L., 2010, MNRAS, 408, 400
 - [8] Ruderman, J.T., Ebeling, H., 2005, ApJ, 623, L81
 - [9] Pimbblet K.A., Shabala S.S., et al., 2013, MNRAS, 429, 1827
 - [10] Kewley L.J., Dopita, M.A., et al., 2001, 556, 121
 - [11] Kauffman G., Heckman T.M., Tremonti C., et al., 2003, MNRAS, 346, 1055
 - [12] Kewley L.J., Groves, B., Kauffman G., Heckman T., 2006, MNRAS, 372, 961

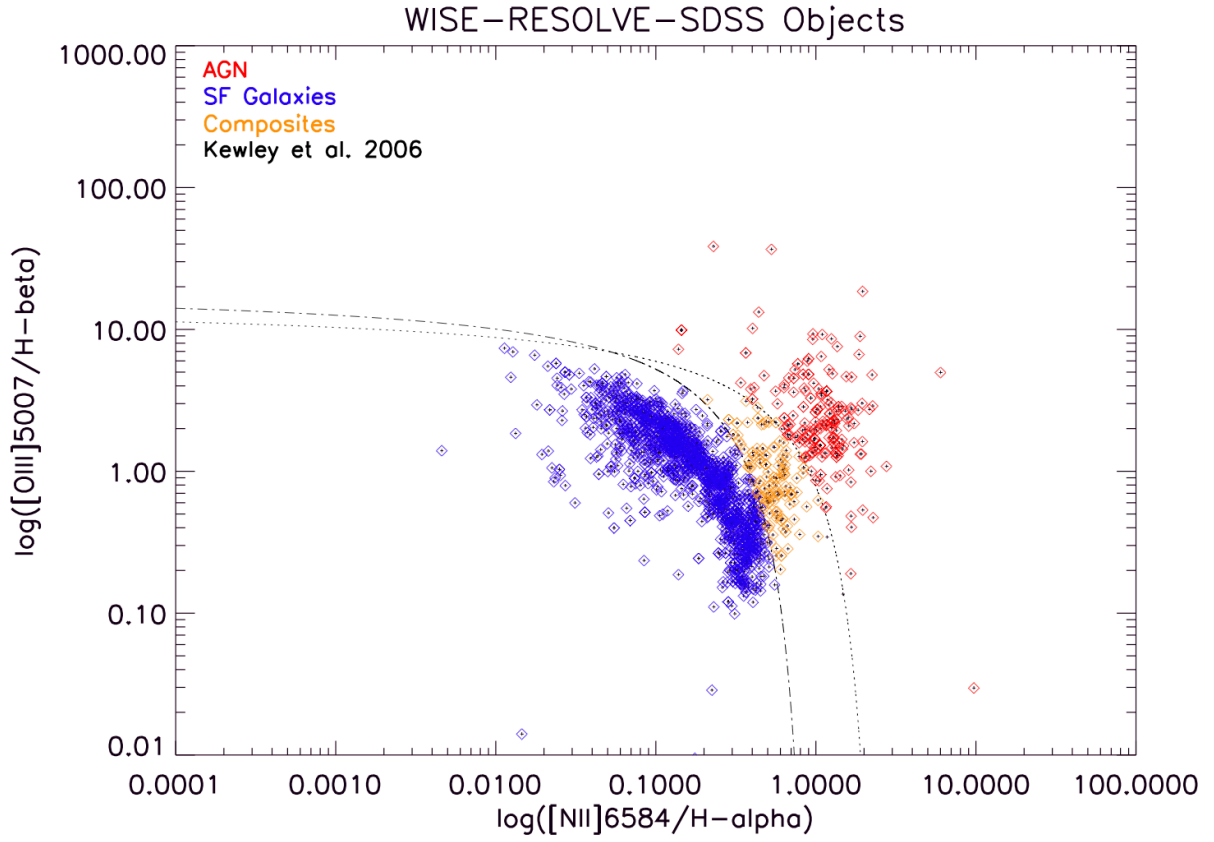


FIG. 2. This figure is a Baldwin-Phillips-Terlevich (BPT) diagram diagnostic diagram of objects in the RESOLVE survey that match sources in the SDSS DR7 spectral data and the WISE Survey. Specifically, it is a log-log plot of $\log([\text{OIII}]5007/\text{H}\beta)$ vs. $\log([\text{NII}]6584/\text{H}\alpha)$. AGN are displayed in red, composite objects in yellow-orange, and star-forming galaxies in blue.

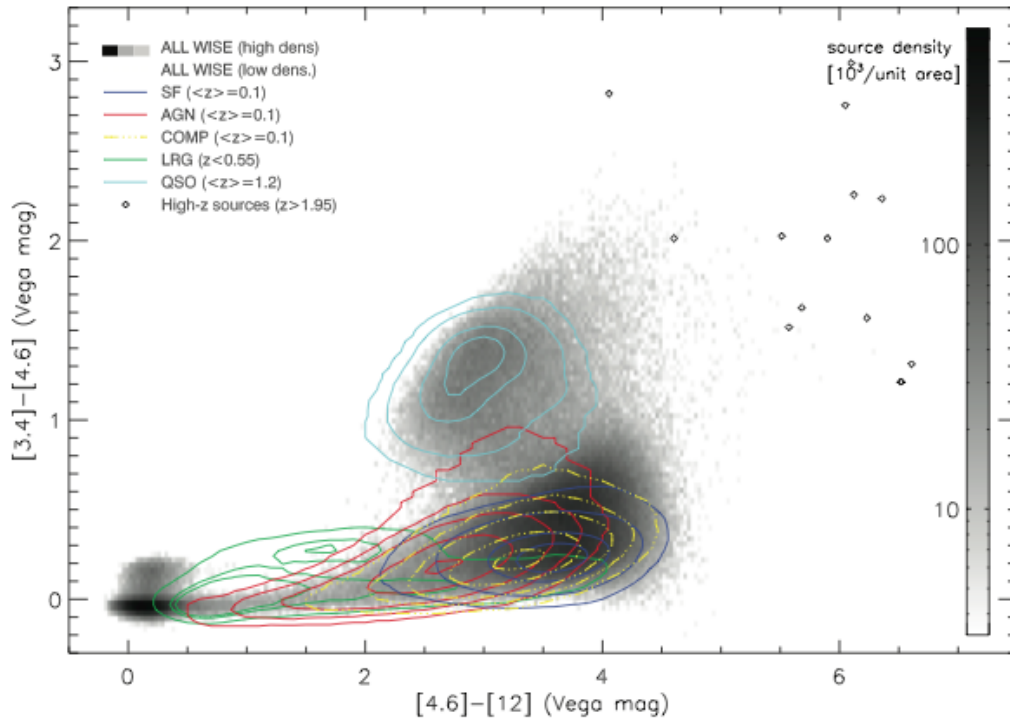


FIG. 3. This figure is the mid-infrared color-color diagram from Yan et al. (2013). Differences of WISE pass bands W1-W2 vs. W2-W3 are plotted against each other. Object classifications are based on the SDSS DR7 source catalog. The color contours are used to visually illustrate the concentrations of source distributions within this color-color space. Yellow represents composite objects, red represents AGN, and blue represents star-forming galaxies.

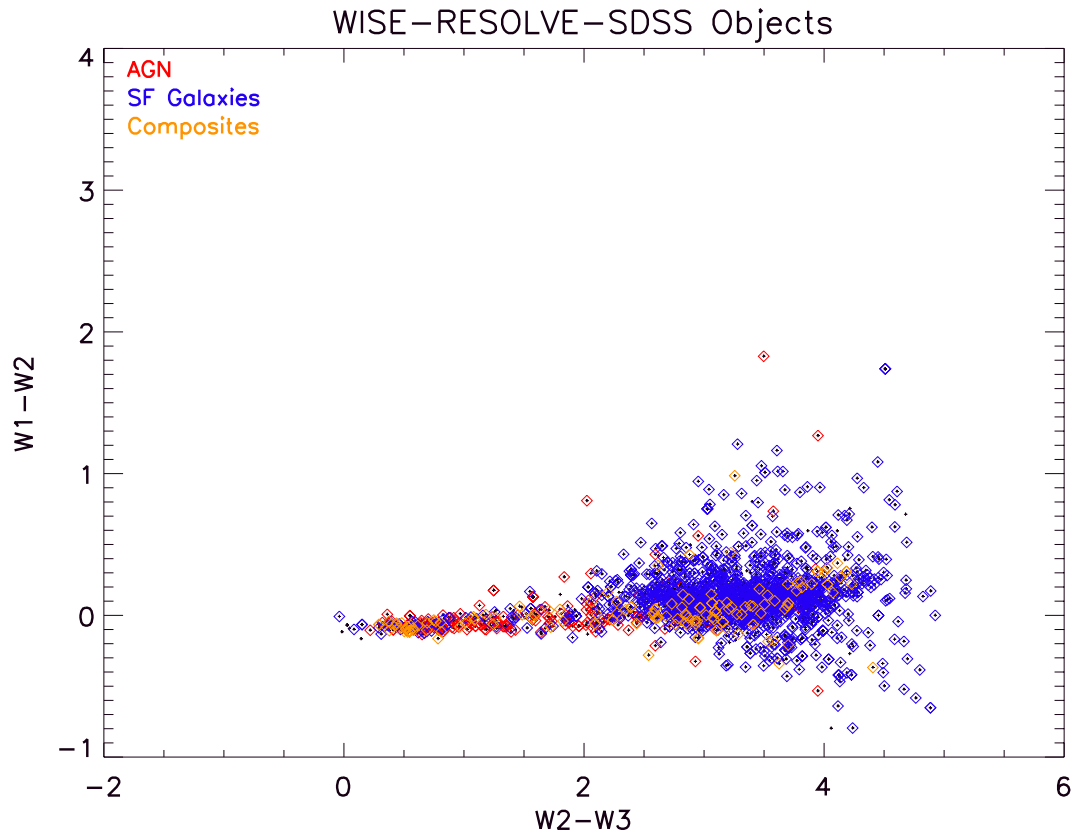


FIG. 4. This figure is the mid-infrared color-color diagram generated from our RESOLVE+SDSS+WISE sample. Objects were classified according to the Kewley et al. 2006 BPT diagnostic diagram criteria. Differences of WISE pass bands $W1-W2$ vs. $W2-W3$ are plotted against each other, yellow-orange represents composite objects, red represents AGN, and blue represents star-forming galaxies as selected from the BPT diagram.

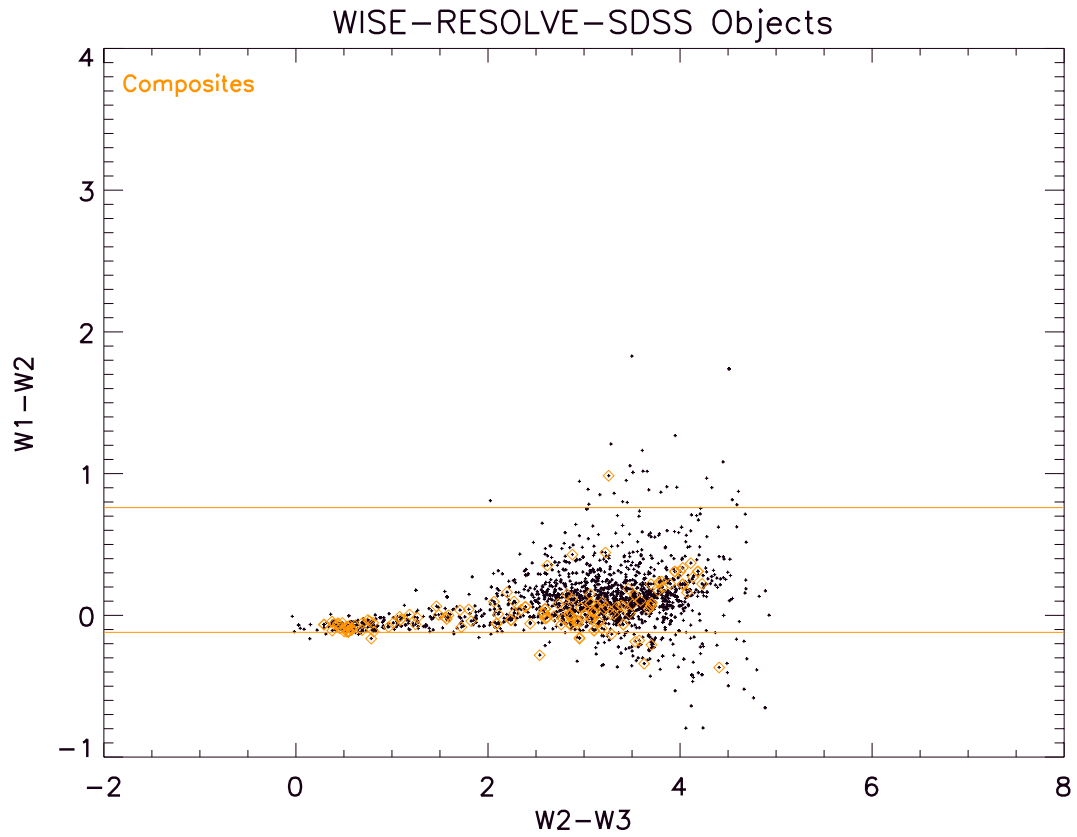


FIG. 5. This figure is the mid-infrared color-color diagram generated from our RESOLVE+SDSS+WISE sample. Objects were classified according to the Kewley et al. 2006 BPT criteria. Only RESOLVE+SDSS+WISE composite objects are displayed. Horizontal yellow-orange lines border composite object Yan et al. yellow-orange contours. Composite objects in both plots fill similar areas.

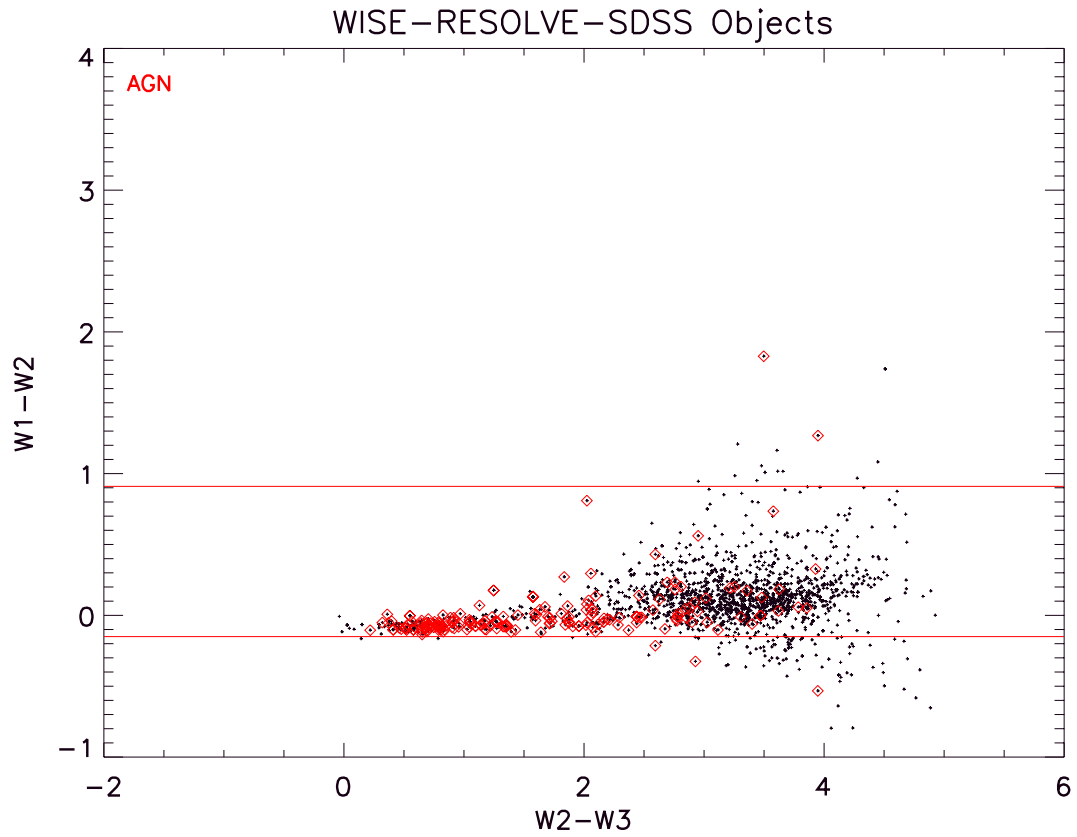


FIG. 6. This figure is the mid-infrared color-color diagram generated from our RESOLVE+SDSS+WISE sample. Objects were classified according to the Kewley et al. 2006 BPT criteria. Only RESOLVE+SDSS+WISE AGN are displayed. The red horizontal lines border AGN Yan et al. red contours. AGN in both plots fill somewhat different areas. See text for details.

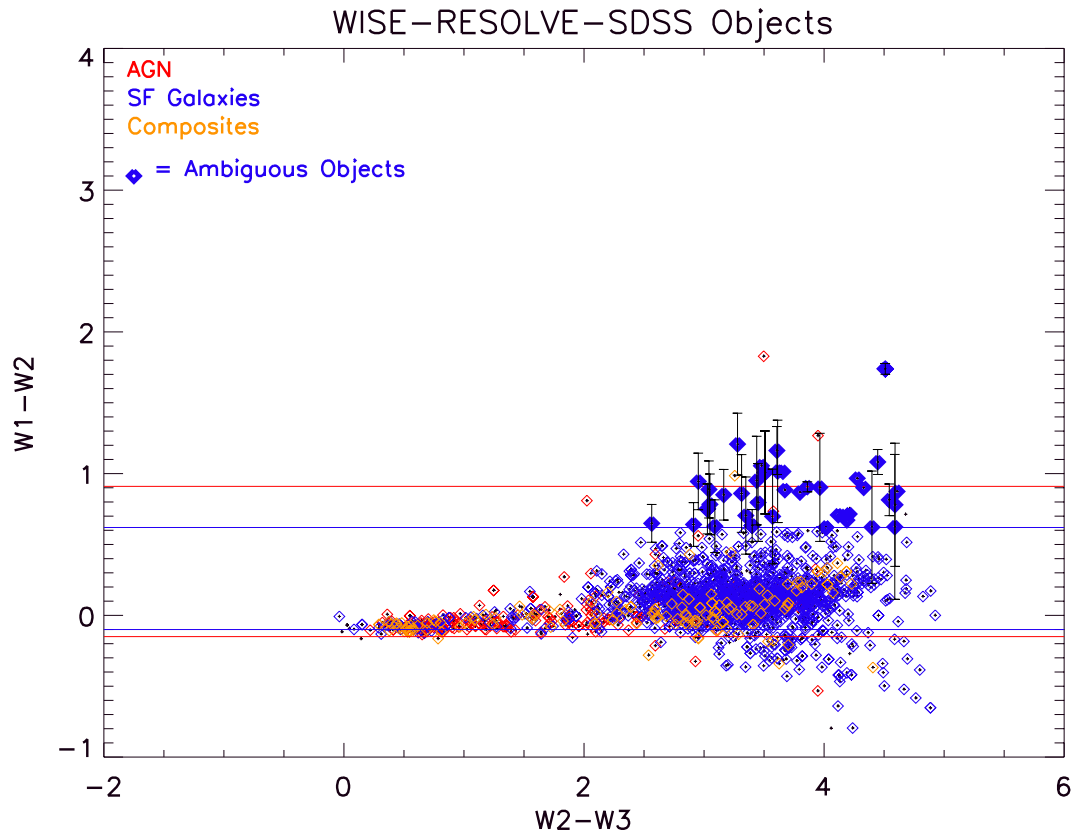


FIG. 7. This figure is the mid-infrared color-color diagram generated from our RESOLVE+SDSS+WISE sample. Objects were classified according to the Kewley et al. 2006 BPT criteria. Sources classified as star-forming by the BPT diagnostic diagram but occupy AGN regions in the mid-infrared color-color plot are highlighted in dark blue. WISE catalog errors from the W1 and W2 pass bands are over-plotted.

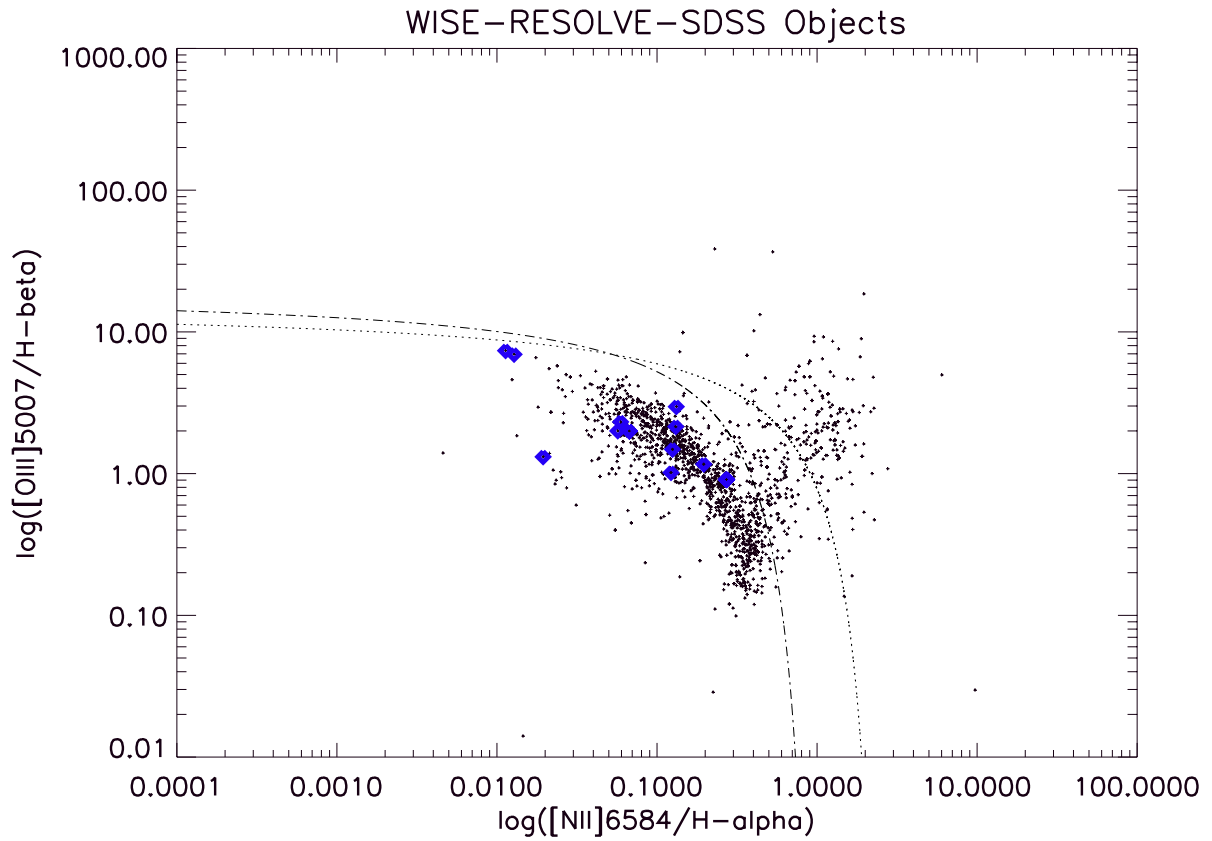


FIG. 8. The BPT plot of RESOLVE+SDSS+WISE objects, a log-log plot of $\log([\text{OIII}]5007/\text{H-beta})$ vs. $\log([\text{NII}]6584/\text{H-alpha})$ as shown in figure 2. The 14 ambiguous objects are over-plotted in blue.

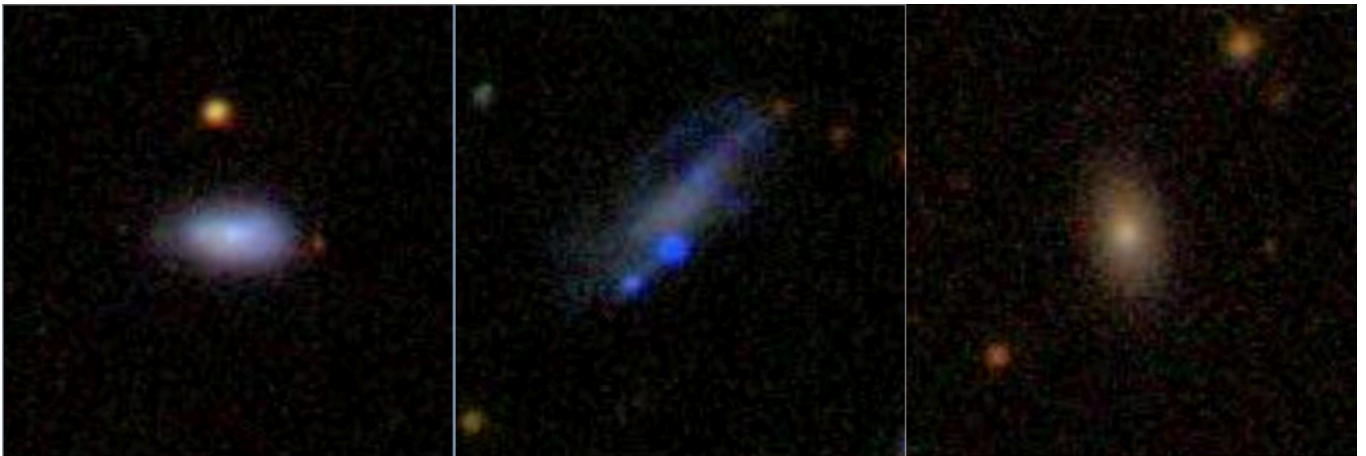


FIG. 9. SDSS optical images of three ambiguous objects. The red color and bright center of the source featured in the right-most panel suggests that it harbors an AGN.

Using Morphology to Identify Galaxy Mergers at High Redshift

Kirsten Blancato

KPNO REU 2013 and Wellesley College, Wellesley, MA 02481

Advisor: Jeyhan Kartaltepe

National Optical Astronomy Observatory, Tucson, AZ 85719

ABSTRACT

We analyzed a set of 22,003 galaxies in three of the five CANDELS fields: COSMOS, UDS, and GOODS-S, in order to determine how well automated image statistics did with classifying galaxy morphology and mergers at high redshifts ($z > 1$). For each galaxy in our set, we have multi-wavelength data, photometric redshifts from SED fitting, visual classifications from the CANDELS structure and morphology group, and automated image statistics. The redshifts of our sample range from $z = .01$ to 4 with $\langle z \rangle = 1.33$. We constructed a conservative set of 1914 galaxies that we believe to be mergers and interactions. Of this set of merging galaxies, 1343 were at a redshift greater than $z = 1$. We also identified a conservative set of 535 spheroids and a set of 2902 disks. Several different quantitative methods were then used to attempt an automated classification of these visually classified samples. Of the different image statistics, we found M20 and Gini to be the most successful at picking out high redshift mergers and morphological characteristics. Initial plots of multimode (M), intensity (I) and deviation (D) statistics appear promising and warrant further study.

Subject headings: galaxy mergers: morphology and structure, galaxy evolution, CANDELS

1. Introduction

Galaxy mergers are thought to play a critical role in both galaxy morphology and evolution. The Hubble sequence divides galaxies in four main morphological groups: elliptical/spheroidal, spiral/disk, lenticular, and irregular. Even though the Hubble sequence was developed for low redshift galaxies (before the evolution of galaxies was understood), many of the galaxies that were classified as irregular turned out to be galaxy mergers. While the traditional Hubble sequence may not be the best classification scheme for high redshift galaxies, it provides a starting point for understanding how the morphology of galaxies has changed since the beginning of the universe.

Based on galaxy morphology beyond the local universe, a theory of hierarchical galaxy evolution has become widely accepted. Two disk-type galaxies interact, merge, and eventually form a larger

spheroidal-type galaxy. As the two disk galaxies begin to interact, star formation is induced from the compression of gas. The gas then falls towards the center of the merging galaxy, feeding the central black hole, creating an active galactic nucleus. After the two disk galaxies coalesced, all merging features disappear and a single spheroidal-type galaxy is remains. Thus, it is expected that disk type galaxies and mergers were more common in the early universe and elliptical galaxies are more common in the local universe. In order to better understand the role galaxy mergers play in galaxy evolution at high redshifts, we first need to be able to identify galaxies we believe to be at different stages of the merging process throughout the history of the universe.

One way to identify galaxy mergers and morphological characteristics is by visual classification. Individuals look through thousands of galaxy images and identify which ones they believe to be

merging or interacting and note any morphological characteristics. While visual classification is robust, it is very time consuming especially since several classifiers are needed for each galaxy in order to get the most unbiased results possible.

Efforts to automatically classify galaxy mergers and morphology have been extensively developed at lower redshifts with moderate success. Several image statistics: M20-Gini and concentration (C), asymmetry (A), and clumpiness (S) have been used to classify mergers and morphology in the local universe. But automatic classification becomes more troublesome at high redshifts for many reasons including the images being fainter and having lower signal to noise. The first step towards a robust automatic system of galaxy classification is determining how well image statistics developed for use at low redshifts do when used in attempts to classify galaxy mergers at high redshifts.

2. Data Set

A sample of 22,003 galaxies from the CANDELS (Cosmic Assembly Near-infrared Deep Extragalactic Legacy Survey) project was used for this study. The CANDELS project is the largest of its kind: probing more than 250,000 galaxies in the infrared from $z = 1.5$ to 8 using the high resolution Wide Field Camera 3 on the Hubble Space Telescope (Koekemoer et al. 2011; Grogin et al. 2011). Each galaxy is imaged in the H-band (F160W) and J-band (F125W). Our sample is drawn from 3 of the 5 CANDELS fields: GOODS-S, UDS, and COSMOS, with a magnitude cut of $H < 24.5$. In our sample 4,627 galaxies are from in COSMOS, 7,274 from GOODS-S, and 10,102 from UDS. The photometric redshifts for each galaxy in our sample was obtained from SED fitting (Dahlen et. al 2013 submitted).

3. Morphological Classification

3.1. Visual Classification

For each of the 22,003 galaxies, we used visual classification information provided by the CANDELS team. The most reliable and common way to classify galaxies is by visual inspection. Although very time consuming, the human eye is particularly apt at identifying patterns in galaxy images and picking up on low surface brightness

merger features such as tidal arms, double nuclei, and asymmetric light distributions. The CANDELS team has developed an extensive visual classification scheme, encompassing numerous galaxy characteristics. There are four main classification categories: morphological class, interaction class, quality and structure, and clumpiness/patchiness. Several morphological classes, structure and quality, and clumpiness/patchiness classifications may be chosen, but only one interaction class may be chosen. Classification categories pertinent to this study are explained below:

Morphological Class

Spheroid: Spheroids are characterized as being a centrally concentrated, round or elliptical, bulge.

Disk: Disks have an extended, diffuse structure that may or may not be surrounding a central bulge. Classifiers can specify if disk is edge-on, face-on, or has spiral arms.

Irregular: Irregular galaxies are disturbed disks or spheroids, or galaxies that would not be classified as either disk or spheroid. All mergers are classified as irregular, but not all irregular galaxies are mergers.

Point Source: The object is a clear point source, compact, or unresolved.

Unclassifiable: Due to an image quality problem, point source contamination, or low signal-to-noise, the object is unable to be classified.

Interaction Class

Merger: Mergers are galaxies that appear to be a single object, but exhibit merger characteristics such as tidal arms, double nuclei, and asymmetries.

Interaction Within Segmentation Map: The central galaxy is interacting with a close companion galaxy that is within the SExtractor segmentation map. Evidence of interaction such as tidal arms, double nuclei, and/or asymmetries are present. Although two separate galaxies are visible, the photometry and image statistics are blended.

Interaction Beyond Segmentation Map: The primary galaxy is interacting with a close companion as evident by interaction characteristics, but each galaxy is within its own segmentation map. Each galaxy has its own separate photometry and image statistics.

Non-interacting Companion: The central galaxy appears to have a nearby companion galaxy, but there are no visible interaction characteristics. The companion status needs to further be determined by redshift data.

Structural Features

Double Nuclei: An object is a double nuclei if there are two bulges contained within a singular stellar envelope.

Tidal Arms: A object has tidal arms if there is disturbed debris and/or dust.

Asymmetry: An object is asymmetric if its light distribution deviates from symmetry.

Each galaxy in our data set has been visually classified by more than three CANDELS Structure and Morphology working group members in order to eliminate as much individual bias as possible. A fractional classifications catalog was created by dividing the number of classifiers per category by the total number of classifiers. Selected classification levels at 1/3, 2/3, and 3/3 for our data set are shown in Table 1. Since only one interaction class can be chosen, the galaxies classified as mergers are not also classified as an interaction class. To identify the individual morphological class, we set the criteria of the other classes having a classification level of 0/3. For example, spheroids only were determined by galaxies classified as spheroid greater than a certain fraction, but disk, irregular, unclassifiable, mergers, and interactions classification levels all equal to zero. Irregular only galaxies were not classified as disks, spheroids, merging, or interacting.

3.2. Automated Classification

To reduce the amount of labor involved in the visual classification method, a quantitative method for classifying galaxies has emerged as a hopeful option. A quantitative method of morphological classification would not only reduce the amount of time it takes to classify thousands of galaxies, but would also allow for a more continuous, rather than quantized, classification scheme. In addition, an automated classification scheme would provide a more consistent way in which to compare different data sets.

There are several different automated image statistics that have been developed in order to

classify galaxies, most which have been optimized at low redshifts ($z < 1$). In this study, we considered eight different statistics, each briefly expanded upon below:

M20: M20 is a measure of the second order moment of brightness of a galaxy's 20 percent brightest pixels. M20 is particularly good at identifying mergers and multiple nuclei (Lotz et al. 2004).

Gini (G): Gini measures the flux distribution among pixels in a galaxy image and is related to concentration. (Abraham et al. 2003; Lotz et. al 2004)

Concentration (C): Concentration is a measure of how concentrated the flux in a galaxy image is (Kent 1985; Abraham et al. 1994, 1996; Bershady et al. 2000).

Asymmetry (A): Asymmetry is calculated by subtracting a 180 degree rotated galaxy image from the original image. Measures how rotationally symmetric a galaxy is. (Abraham et al. 1996, Conselice et al. 2000)

Clumpiness (S): Clumpiness is a measure of how discontinuous the light distribution of a galaxy is (Conselice 2003).

Multimode (M): Multimode is particularly apt at identifying double nuclei (Freeman et al. 2013).

Intensity (I): Intensity is a complement to the multimode statistic, picking up on all high intensity pixel groups (Freeman et al. 2013).

Deviation (D): Deviation measures a galaxy's deviation from elliptical symmetry (Freeman et al. 2013).

Typically, there are three different subsets of these statistics used to quantify galaxy morphology: M20-Gini, CAS, and MID. The use of M20-Gini and CAS statistics has been optimized for merger and morphological identification a low redshifts by Lotz et al. 2004; Conselice 2004, and Bershady et al. 2000 (check this). MID statistics have recently been developed specifically for high redshift galaxies and seems promising (Freeman). For this study, parameter catalogs produced by the CANDELS team (Lotz et al. in preparation) for each of our three CANDELS fields were acquired. We have measures of all eight statistics for our entire set of 22,003 galaxies.

4. Results

4.1. Asymmetry

Intuitively, it seems as though the asymmetry parameter should do a decent job at picking out visually identified mergers. Even though high redshift mergers have lower signal-to-noise and are fainter, one could reasonably expect that the asymmetry parameter, which is measured by subtracting a 180 degree rotated galaxy image from the original, should be able to identify galaxy mergers which are nearly always asymmetric. At low redshifts, it has been determined that an $A > 0.35$ indicates a major merger (Conselice et al. 2003).

For our entire set of galaxies, $|\tilde{A}| = 0.07$. For $z < 1$, $|\tilde{A}| = 0.07$, $1 < z < 2$, $|\tilde{A}| = 0.06$, and $z > 2$, $|\tilde{A}| = 0.07$. In order to compare our results to results at low redshift, we plotted the asymmetry parameter versus the concentration coefficient for different classification categories: disk only, spheroid only, merger only, and both interaction classes (Figure 1). We found that the merger and morphological boundaries from Consilience 2003 and Bershady 2000 identified only 5.3 percent of all visually classified mergers at 1/3 and 9.4 percent of mergers at 2/3. Asymmetry versus Gini is also plotted (Figure 2). As expected, many of the visually classified mergers were not recovered, but there was an encouraging separation in the concentration of spheroids and disks at both the 1/3 and 2/3 levels. For disks, $\log(\tilde{G}) = -0.32$ and for spheroids $\log(\tilde{G}) = -0.29$. In both the asymmetry versus concentration and asymmetry versus Gini plots, there was no clear separation between interaction classes.

To better understand why asymmetry does not recover a majority of galaxy mergers at higher redshifts, we look at how the asymmetry parameter correlates with visually classified asymmetry. As seen in Figure 3, the median of the asymmetry parameter is highest for galaxies with a fractional classification level greater than 4/5 and for lower classification levels, the asymmetry parameter is approximately 0.2 to 0.4 lower. The difference indicates that only the most highly disturbed and asymmetric galaxies that a majority of classifiers agree upon are calculated to have a high asymmetry parameter value. This is problematic because

faint merging galaxies are not being identified from the asymmetry parameter.

4.2. M20-Gini

M20-Gini statistics have proven to be quite successful at separating out mergers, disk, and spheroidal galaxies in the local universe. In Lotz 2008, boundary lines between merging galaxies and regular galaxies and between early and late type galaxies were developed based on visual classifications of galaxies at $z = 0$. In this study, we attempt to extend the success of M20-Gini statistics to our sample of high redshift galaxies.

For our full set of galaxies, $\tilde{M}20 = -1.6$ and $\tilde{G} = 0.49$. For $z < 1$, $\tilde{M}20 = -1.6$ and $\tilde{G} = 0.50$, $z = 1 - 2$, $\tilde{M}20 = -1.6$ and $\tilde{G} = 0.49$, and $z > 2$, $\tilde{M}20 = -1.5$ and $\tilde{G} = 0.49$. Figure 4 shows M20 versus Gini for disks only, spheroids only, mergers, and both interaction classes. From these plots, it is clear that there is a separation in the concentration of disks and spheroids. There is also a slight separation between the two interaction classes, with the galaxies classified as interacting within the segmentation map being more concentrated in the merger region while the galaxies classified as interacting beyond the segmentation map being more concentrated in the disk region. We found that the merger and morphological boundaries from Lotz 2004 identified 12.46 percent of all visually classified mergers at 1/3 and 18.67 percent of mergers at 2/3. While the percentage of mergers that M20-Gini statistics recovers is still not optimal, M20-Gini identifies approximately twice as many mergers than the asymmetry parameter.

We also investigate how M20-Gini statistics evolve with redshift. For our sample of UDS and GOODS-S galaxies, we plotted spheroids only and disks only percent automatically classified at a level of 2/3 and mergers at a level of 1/3 for $z = 0 - 4.5$, 0.5 binned and an eighth bin of $z > 4.5$ (Figures 5 and 6). While these plots still need to be considered further, we initially find a possible increasing trend for mergers identified as redshift increases from $z = .05$ to $z = 3.0$. While M20-Gini does a much better job with classifying disks than spheroids, the percent correctly classified for spheroids and disks seems to remain fairly constant.

To make the first step towards eliminating con-

tamination using M20-Gini statistics, we looked at some of the objects that fell above the merger boundary but were not visually classified as merging, irregular, interacting, or as having any merger structural features. Figure 7 shows an object that is visually classified as a spheroid that fell above the merger line. The object appears to be compact/unresolved and possibly a point source. Figure 8 and 9 show objects that are visually classified as disks but both also fall above the merger boundary. The disks of both objects are very faint, and the second object’s disk is asymmetric. Introducing cuts on point source classification and a signal to noise minimum may possibly aid in reducing the contamination of disks and spheroids above the merger boundary.

Since our data set is so large, we decided that contour plotting would aid in the visualization of our plots. Figures 10 - 12 are M20-Gini contour plots for three redshift bins: $z < 1$, $1 < z < 2$, and $z > 2$. In each plot, we have mergers/interaction within segmentation map, disks only, and spheroids only contoured separately. Interaction within segmentation map was included with the mergers for two main reasons. The difference between merger and interaction within segmentation map is really a judgment call based on what stage of the merging process a classifier believes the galaxy is currently in. Interaction beyond segmentation map was not included because there was a slight separation between the interaction classes in the M20-Gini interaction plot of Figure 4 and because for interaction beyond segmentation map, the automated statistics are computed separately for each galaxy. Thus, we decided including just interaction within segmentation map and not beyond would be best. Adding in the interaction within segmentation map at 2/3 to our mergers at 2/3 increased our total number of mergers/interactions to 1902 galaxies: 225 mergers only, 688 interactions within segmentation map only, and 989 objects classified as merger + interaction within above a classification level of 2/3. As evident by the contour plots, there is a separation between the highest densities of mergers/interaction within, disks, and spheroids for all three redshift bins. The greatest separation though is for the $z > 2$ contour (Figure 12). This result needs further investigation.

4.3. MID Statistics

In addition to CAS and M20-Gini statistics, we began some initial work for MID statistics. Multimode, intensity, and deviation statistics are the newest image statistics being applied to galaxy morphology at high redshift. Freeman et al. 2013 has concluded MID statistics in conjunction with asymmetry to be the useful for identifying galaxy mergers at $z > 2$. For our data set, we saw little separation between morphologies using MID and A statistics alone. But, we did some three-dimensional plots of different MID statistics and M20-Gini parameters and did find some encouraging separations. Figure 13 shows a projection of one of our three-dimensional plots onto the multimode versus M20 plane. There is a clear separation between spheroids and mergers, and the disks appear to be concentrated at lower multimode values than the mergers, but there is considerable overlap.

5. Conclusions and Future Work

For our set of 22,003 visually classified galaxies, we were able to form a set of 1,914 galaxies we are confident to be mergers and used several different image statistics to see how well automated classification methods did with identifying mergers and other morphological features at high redshift. In general, the asymmetry parameter was the least successful at recovering mergers. This may be due to the fact that only the most disturbed galaxies, classified at a high level of confidence, have a greater asymmetry parameter value. Our investigations of M20-Gini statistics for high redshift mergers prove to be the most promising. M20-Gini statistics picked out twice as many mergers than asymmetry statistics and initial contour plots are encouraging. We also began looking at the new MID statistics and found that further consideration is merited. While an automated classification scheme is certainly preferable, our work shows that visual classification is still necessary at higher redshifts.

Future work includes selecting an even more conservative set of mergers, considering redrawing the M20-Gini boundary lines for high redshifts, and using different combinations of statistics. To optimize the data set, a signal to noise cut could be placed so that the faintest disks and spheroids

that contaminated the merger region would be removed. Further work can be done based on the M20-Gini contour plots. To optimize the comparison between the different redshift bins, ACS data for $z < 1$ can be used so that all three redshift bins are using rest frame optical data. In addition, as shown in Figure 12, new merger boundary lines can be developed that would maximize the number of mergers identified while minimizing the contamination from other classification categories. Lastly, beyond just M20-Gini statistics, MID statistics different combinations of all eight statistics can be explored to see which is optimal for picking out mergers and morphological features at high redshifts.

6. Acknowledgements

I would like to thank my advisor Jeyhan Kartaltepe for her support and guidance and the other NOAO staff and scientists that made the KPNO REU a great experience.

This research was supported by the NOAO/KNPO Research Experiences for Undergraduates (REU) Program which is funded by the National Science Foundation Research Experiences for Undergraduates Program and the Department of Defense AS-SURE program through Scientific Program Order No. 13 (AST-0754223) of the Cooperative Agreement No. 13 AST-0132798 between the Association of Universities for Research in Astronomy (AURA) and the NSF.

REFERENCES

- Abraham, R.G., Valdes, F., Yee, H.K.C. & van den Bergh, S. 1994, ApJ, 432, 75
- Abraham, R.G., van den Bergh, S., Glazebrook, K., Ellis, R.S., Santiago, B. X., Surma, P., & Griffiths, R. E. 1996, ApJS, 107, 1
- Abraham, R.G., van den Bergh, S., & Nair, P. 2003, ApJ, 588, 218
- Bershady, M.A., Jangren, A., & Conselice, C.J. 2000, AJ, 119, 2645
- Conselice, C.J. 2003, ApJS, 147, 1
- Conselice, C. J., Bershady, M. A., & Jangren, A. 2000, ApJ, 529, 886
- Dahlen et al. 2013, submitted
- Freeman, P.E., Izbicki, R., et al. 2013, MNRAS, 434, 282F
- Grogin, N.A., et al 2011, ApJS, 197, 35
- Kartaltepe, J. S., et al. 2010b, ApJ, 721, 98
- Kent, S.M. 1985, ApJS, 59, 115
- Koekemoer, A.M., et al. 2011, ApJS, 197, 36
- Lotz, J.M., et al. 2008a, ApJ, 672, 177
- Lotz, J. M., Primack, J., & Madau, P. 2004, AJ, 128, 163

TABLE 1
VISUAL CLASSIFICATION RESULTS

Classification	1/3	2/3	3/3
Merger	1396	225	29
Interaction Within Segmentation Map	2359	688	162
Interaction Beyond Segmentation Map	5028	2163	683
Tidal Arms	252	8	1
Double Nuclei	109	4	1
Spheroid Only	540	535	517
Disk Only	2926	2902	2857
Spheroid and Disk	3163	1274	337
Irregular Only	15	15	12

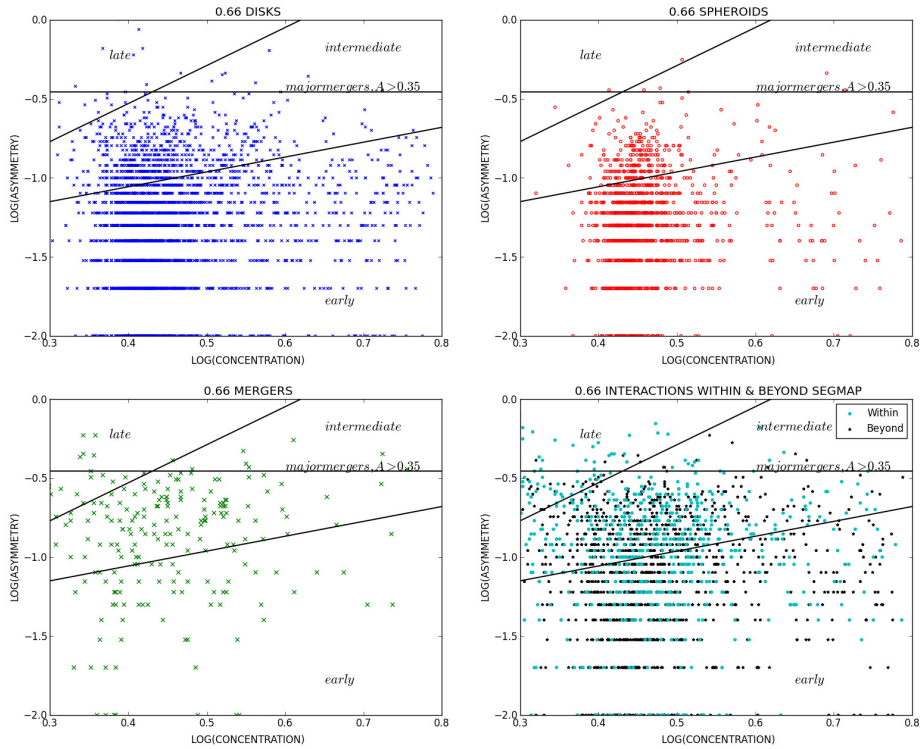


Fig. 1.— Asymmetry v. concentration for different classification categories. The sloped lines are boundaries between early, intermediate, and late type galaxies from Bershady et al. 2000. Above the horizontal line at $\log(|A|) = -0.46$ ($|A| = 0.35$) is where objects classified as major mergers are expected to fall (Conselice 2003).

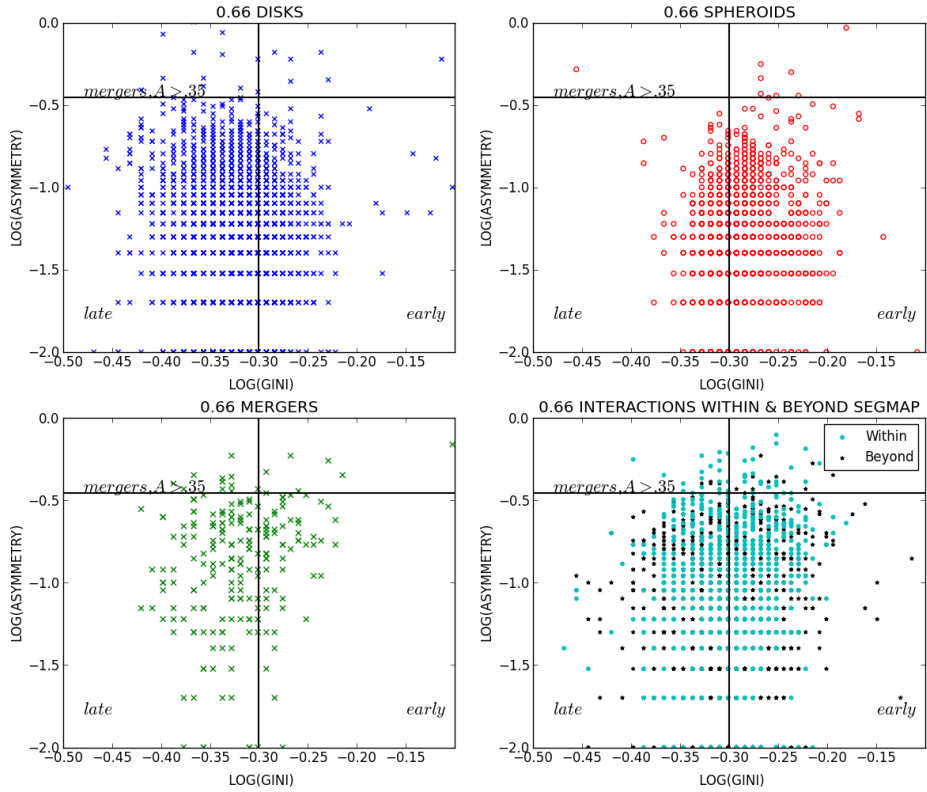


Fig. 2.— Asymmetry v. Gini for different classification categories. Above the horizontal line at $\log(|A|) = -0.46$ ($|A| = 0.35$) is where objects classified as major mergers are expected to fall (Conselice 2003). The vertical line at $\log(\text{Gini}) = -0.3$ ($\text{Gini} = 0.5$) divides where late and early type galaxies are expected to fall.

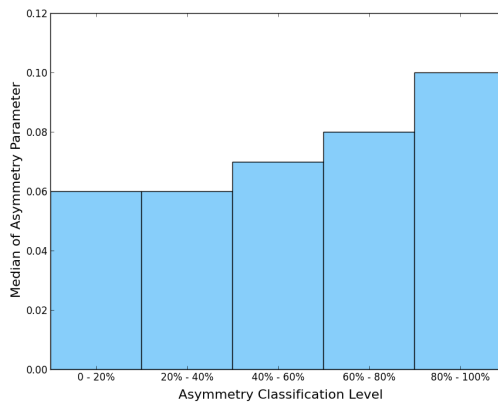


Fig. 3.— Asymmetry parameter v. asymmetry classification level. The median asymmetry parameter value increases as classification level increases. The most disturbed galaxies have the highest asymmetry values.

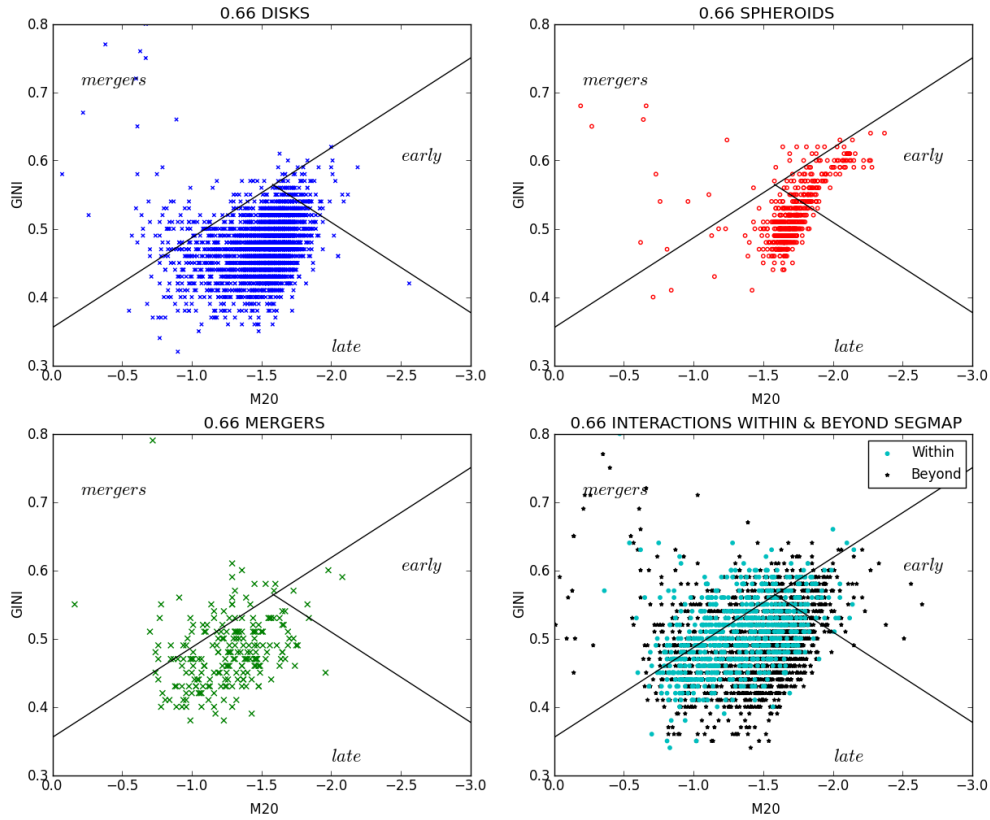


Fig. 4.— Gini v. M20 for different classification categories. The lines represent the division between early, late, and merger galaxies determined from local universe results in Lotz 2008a.

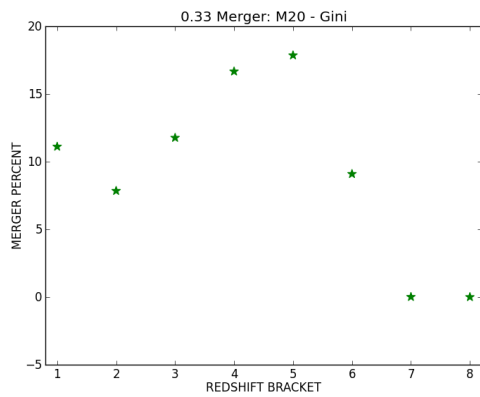


Fig. 5.— Percent classified as merger v. redshift for UDS and GOODS-S galaxies.

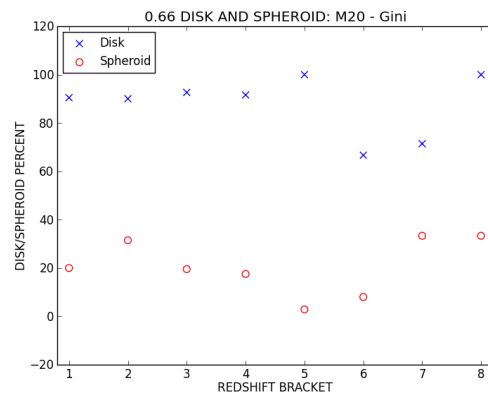


Fig. 6.— Percent classified as spheroid or disk v. redshift for UDS and GOODS-S galaxies.

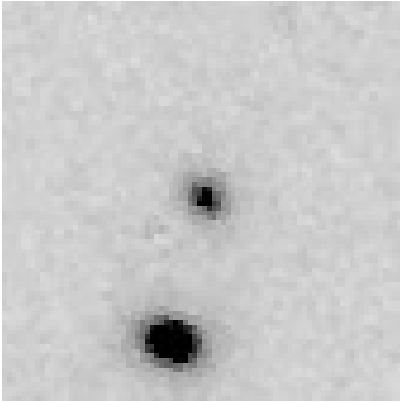


Fig. 7.— Object visually classified as spheroid, but automatically classified as merger.

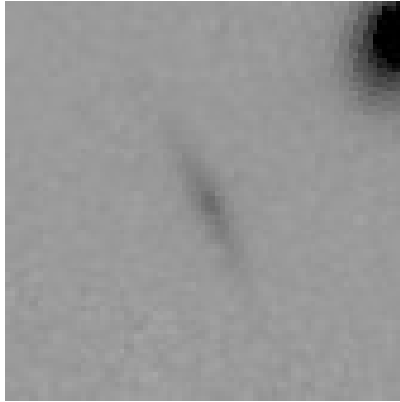


Fig. 8.— Object visually classified as disk, but automatically classified as merger.

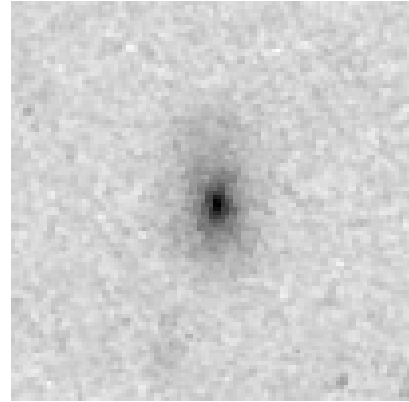


Fig. 9.— Object visually classified as disk, but automatically classified as merger.

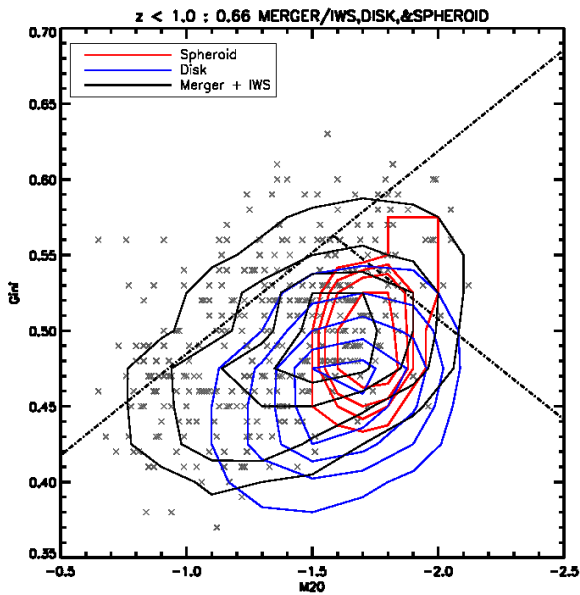


Fig. 10.— M20-Gini contour for $z < 1.0$. Note the locations of the highest concentration of spheroids, disks and mergers/interaction within segmap.

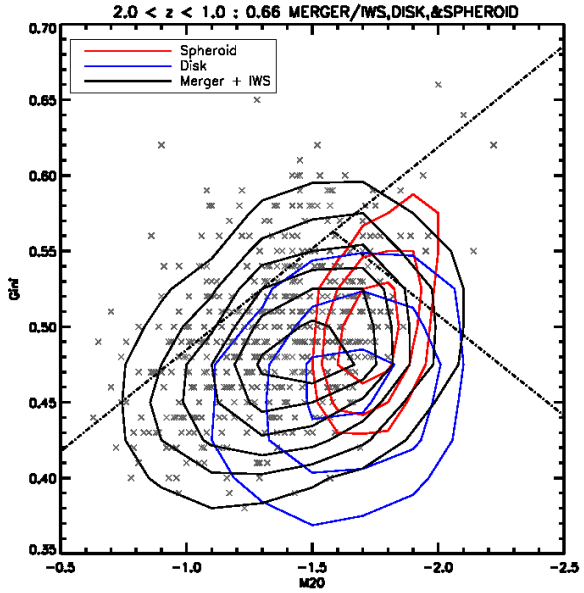


Fig. 11.— M20-Gini contour for $1.0 < z < 2.0$. Note the locations of the highest concentration of spheroids, disks and mergers/interaction within segmap.

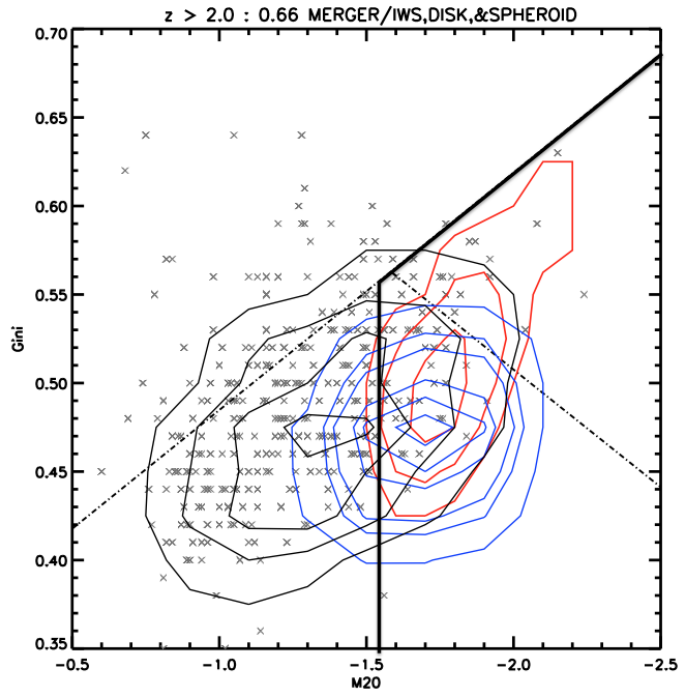


Fig. 12.— M20-Gini contour for $z > 2.0$. Note the separation between the highest concentrations of spheroids, disks, and mergers/interaction within segmap. The solid lines represent a new possible dividing line that could be used to pick out the greatest number of mergers while minimizing the amount of contamination.

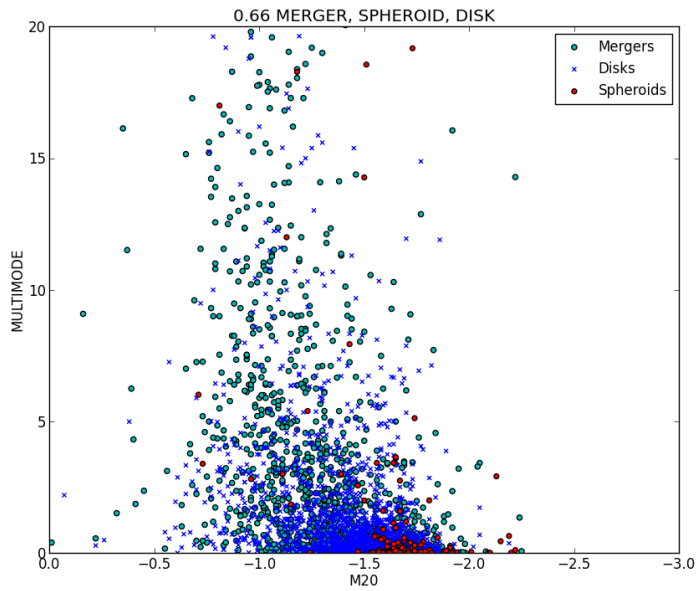


Fig. 13.— Multimode v. M20 plot.

A Light Pollution Assessment of Tucson, AZ

By: Jeanine Chmielewski
Adviser: Stephen Pompea

Abstract

The panoramic photo of Tucson taken from the top of Tumamoc Hill gives a good overview of areas of Tucson with problem lights that need to be studied more closely. These problem areas are caused mainly by poor shielding or over-illumination. A study was done at 10 locations around Tucson along the main streets of Grant, Speedway, and Broadway. Both lux readings and spectra were taken at these locations. The dominant light type seen at these locations was high pressure sodium. The majority of these locations were gas stations that had Lux levels ranging from 116.9 Lux to 481 Lux. With the exception of the first gas station, they were all lit at the level an office workspace would be lit at. The Quebedeaux Buick GMC was lit at 730 Lux which is the equivalent of what a surgery preparation room should be lit at. New LED lights were also observed on the campus of the University of Arizona. All LED lights had a significant bump in the blue region of the spectrum. This wastes energy as the human eye is less sensitive at those wavelengths. The blue emissia should be suppressed for better efficiency and to help minimize health risks.

Introduction

Light pollution has been around since man discovered fire. Since the industrial revolution and the discovery of electricity, the effects of light pollution have increased significantly. The addition of artificial light from the human population is increasing at an alarming rate. Astronomers were among the first to realize the problem because it directly affects their work.

As urban centers increase and spread out, so do the lights. This increases skyglow, the brightening of the night sky. This makes it much more difficult to see dimmer stars and galaxies. Other forms of light pollution can cause other problems as well. Glare is a form of light pollution that is most dangerous when driving. An improperly shielded light can cause significant glare. Glare often occurs when you can still see the light bulb with its high surface brightness.

This is problematic because that can cause vision impairment which can lead to accidents. Light trespass is also an unwanted form of illumination. It occurs when light is shining in an area where it is unwanted, like a bedroom or a living room. The most common occurrences are caused by incorrectly shielded lights or lights that are aimed in the wrong direction.

The evolution of lighting is also of interest. Astronomers tend to prefer that outdoor lights are low pressure sodium. "The application of low-pressure sodium lamps is considered as the most important single remedy for the interference with astronomical observations" (Crawford 1991) This is because low pressure sodium is monochromatic, or single color, and therefore more easily filtered out. They are however not used very much commercially anymore for that reason. If a light is monochromatic then colors are more difficult to distinguish from each other. This spectrum can be seen in Figure 1.

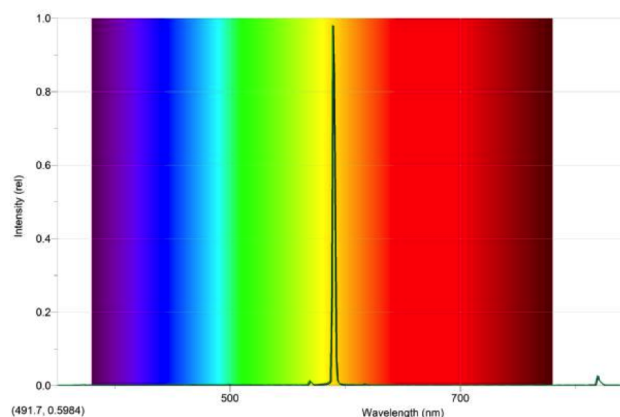


Figure 1: The spectrum of a low pressure sodium light taken from the entrance of Steward Observatory on the campus of the University of Arizona.

High pressure sodium lights fix this problem as they are not monochromatic. This spectrum can be seen in Figure 2. They are the dominant lights for street lamps currently used

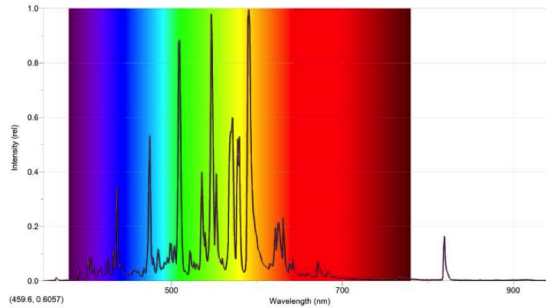


Figure 2: The spectrum of a high pressure sodium light. The other peaks in the spectrum is the addition of other metals to make the overall light output more white. This was taken at the Applebees on Grant and Swan.

in Tucson. The new LED lights are not monochromatic either and provide a whiter light source because they are full spectrum. They do unfortunately, have a massive spike in the bluer wavelengths. The human eye is less sensitive to these wavelengths however, and these wavelengths can cause medical problems like sleeping disorders (Bogard 2013).

Methods

Identifying and understanding the problem light sources in Tucson is the first step to fixing them. I took panoramic photos of the areas under study to gain a general understanding of where the problem areas are. By taking the photo from an elevated height, it is possible to determine both where over-illumination and poor shielding occurs. For this study, a panoramic photo of Tucson, AZ was taken from the top of Tumamoc Hill. The photos were taken with a Cannon EOS Digital Rebel camera. The ISO was set at 1600 and had a f/5.6 aperture for best resolution. From this photo, unusually bright areas and unshielded lights were identified.

The next step was to go to these problem areas to assess the luminaire and lighting characteristics in more detail. Both a lux reading and a spectrum was taken at all of the locations around Tucson. A Dr. Meter Digital Illuminancer Light Meter LX130B, 0-200,000 Lux Luxmeter was used to take measurements. The spectra were taken with an Ocean Optics USB650-VIS-NIR Spectrophotometer. For consistency, the lux meter was placed parallel to the gas pumps and in the center of the pumping station. The spectrometer fiber optics probe was held at a consistent height of 2 feet off the ground to reduce over-saturation.

This spectrometer was also used to study the new LED lights that have been installed along the grass area of the University of Arizona campus. The spectrometer has a fixed integration time of 15s. By determining the spectra of these lights, we can begin to study how LED lights might differ. The evolution of LED lights can also be monitored with this method, leading to a better understanding of the lights themselves.

Data and Analysis



Figure 3: The night-time panoramic view of the city of Tucson, AZ from the top of Tumamoc Hill.

As can be seen from Figure 3, there are many bright spots that indicate both poorly shielded lights and areas of over-illumination. By comparing this photo with the images of the 3D section of Google Earth, exact locations of the bright spots can be predicted. These areas are centered around the main crossroads of the city. Therefore, when closer inspection of the lights was performed, the main streets of Grant, Speedway, and Broadway were used. The east and west boundaries of the area were Swan Road and Euclid Ave. respectively. On these streets a total of 10 locations were sampled.

Number	Place	Lux Reading	Light Type
1	Apppees (No Light, on Grant and Swan)	2	None
2	Highland Ave. (Campus near 6th Street)	28.3	High Pressure Sodium
3	Applebees (Light, on Grant and Swan)	75	High Pressure Sodium
4	Fry's Gas Station (Grant and Euclid)	116.9	High Pressure Sodium
5	Shell Gas Station (Speedway and Columbus)	230	High Pressure Sodium
6	Giant Gas Station (Grant and Stone)	375	High Pressure Sodium
7	Shell Gas Station (Grant and Euclid)	415	High Pressure Sodium
8	Chevron Gas Station (Grant and Tucson)	451	High Pressure Sodium
9	Circle K Gas Station (Grant and Alvernon)	481	LED
10	Quebedeaux Buick GMC (Speedway)	730	High Pressure Sodium

Table 1: The Lux level readings taken at their respective locations. The specific spectrum of each light can be found in the Appendix.

As Table 1 shows, the lux level varies significantly among the locations. According to Di-Laura et. al. 2001, outdoor lighting does not need to exceed 200 Lux. The first four locations have light level readings that place them well within these acceptable ranges. The fifth location is just above these acceptable ranges, and compared with the later locations, it still has a respectable Lux level reading.

Locations six through nine have too much light. All of them have at least double the amount of light that is necessary. The Lux levels are close to what an office workspace should be at. An office workspace varies between needing 350 Lux and 500 Lux depending on the type of office (DiLaura et. al. 2011). The last location is the worst offender of over-illumination with almost four times the necessary amount of light. To compare, a surgery preparation

room is supposed to be lit at 750 Lux (DiLaura et. al. 2011).

These light levels are both alarming and unnecessary. By reducing the Lux levels of the offending locations, the area would still be well lit and the money saved through energy would be enormous. Even just turning off half of the lights would be a step in the correct direction. This amount of over-illumination also does not serve the purpose intend. Because these lights are so bright, it is actually more difficult to see what is beneath them. This is caused by the glare from the light bulbs.

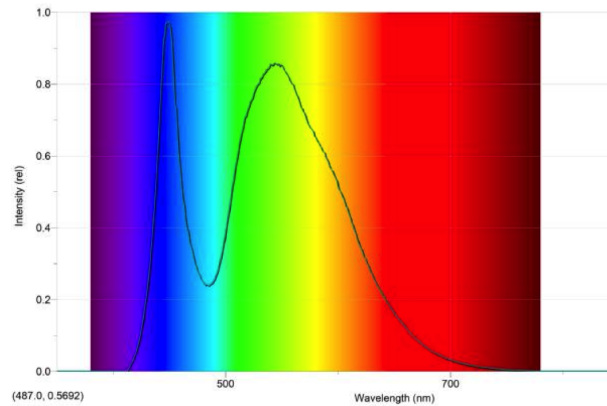


Figure 4: The LED spectrum taken from the Circle K gas station on Grant and Alvernon.

The blue spike within Figure 4 is also wasteful. The human eye is not as sensitive at those wavelengths, so the light is not helping visibility as much as the lighting companies would like. These lights need to be modified to suppress or completely remove this blue bump, if energy efficiency is valued, and glare is to be reduced.

Figure 5 is the LED spectrum from a completely different set of lights from the spectrum shown in Figure 4. Both of the spectrums have a significant bump in the blue. The reason it is dimmer in Figure 5 is because the actual light bulbs are further away and therefore, the light had more time to scatter. This is not a desired result because the scattered blue light contributes heavily to skyglow. Blue light scatters more then the lower energy wavelengths and the scattered light goes further due to Rayleigh scattering (Hecht 2002). Therefore the blue wavelengths are the most detrimental to astronomers, because of their role in skyglow.

Unfortunately, the blue wavelengths are also detrimental to human health (Bogard 2013). The blue wavelengths and light pollution as a whole, contribute to sleeping disorders, diabetes, obesity, heart problems, and cancer. (Bogard 2013) (Blask et. al. 2005) It is seen most prominently in women shift workers who work around bluer lights. "The 460nm monochromatic light causes twice the amount of melatonin suppression compared to 555nm monochromatic light, and is dependent on the duration of exposure in addition to wavelength (Lockley et. al. 2003). This decrease in melatonin levels then makes the person more

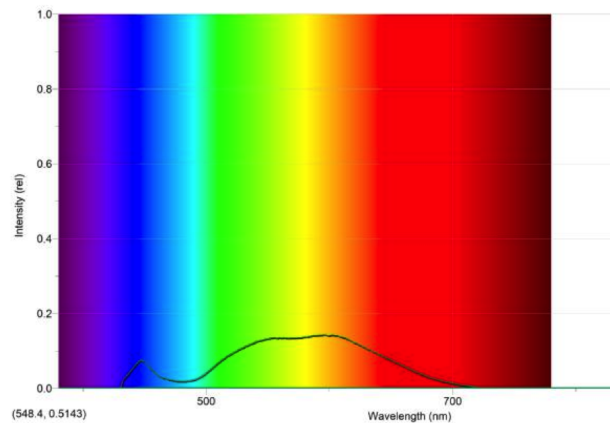


Figure 5: The LED spectrum from one of the lights on the campus of the University of Arizona.

prone to breast cancer. "Circadian melatonin signal not only inhibits human breast cancer growth, but that this effect is extinguished by short-term ocular exposure to bright, white light at night" (Blask et. al. 2005) The best way to counteract this problem is to reduce the amount of blue wavelengths being emitted from the light sources.

Conclusion

The characteristics of city lights is always changing. The migration from low pressure sodium lights, to high pressure sodium lights, to the new LED lights is a natural progression. The efficiency of the lights have improved making it more appealing for people to make the switch. Some problems however are still there and they need to be addressed.

The over-illumination of areas is both unnecessary and wasteful. Reducing lux levels by half in the offending areas is usually enough to fix the problem. Proper shielding is also a major concern. By having a properly shielded light, the area affected is limited, and the light goes where it is needed. The blue wavelengths in the new LED lights is also an issue that needs to be addressed.

The suppression of these wavelengths would improve their efficiency. Not only is the human eye not sensitive to these wavelengths, but they can also cause medical problems as well. The blue wavelengths can cause sleeping disorders which can be a potential cause of other medical problems like cancer. This is a field of study that still needs to be refined. More data must be taken at more locations to gain a better understanding on the effects and solutions of light pollution. My work on this project has identified some common problems of Tucson lighting and suggests that improved LEDs may help minimize potential biological effects of overly blue lighting.

References

Blask D.E. et. al. Melatonin-Depleted Blood from Premenopausal Women Exposed to Light at Night Stimulates Growth of Human Breast Cancer Xenografts in Nude Rats. American Association for Cancer Research. 2005

Bogard, Paul. The End of Night: Searching for Natural Darkness in an Age of Artificial Light. Little, Brown and Company. 2013. Page 93.

Crawford D.L. Light Pollution, Radio Interference, and Space Debris. Astronomical Society of the Pacific Conference Series, Volume 17. 1991. Page 28.

DiLaura, D.L., Houser, K.W., Mistrick, R.G., Steffy, G.R. 2001. The Lighting Handbook (10th Edition; Illuminating Engineering Society of North America).

Hecht, Eugene. Optics. 4th Edition; Addison Wesley. 2002. Pages 86-88.

Lockley S.W. Brainard GC, Czeisler CA. High Sensitivity of the Human Circadian Melatonin Rhythm to Resetting by short Wavelength Light. J Clin Endocrinol Metab. 2003 Sep; 88(9): 4502-5.

Appendix

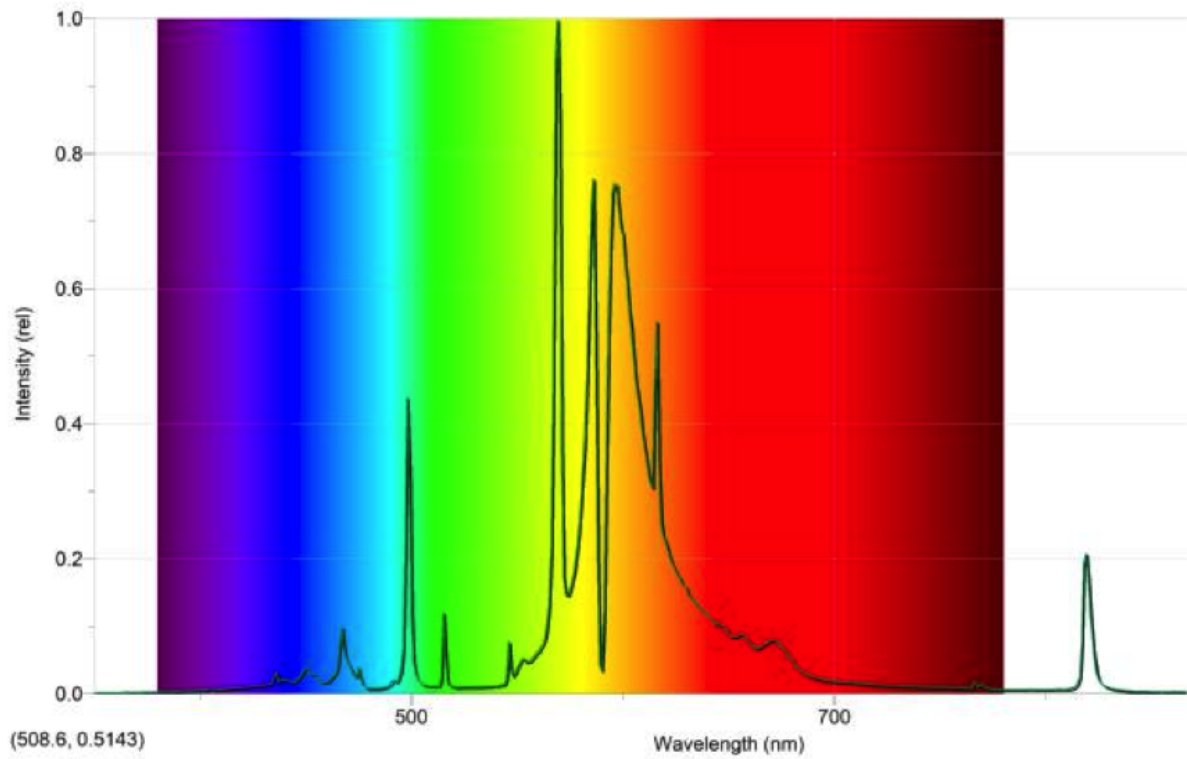


Figure 6: The spectrum taken on Highland near 6th street. It was the 5 street lamp into campus on the right side.

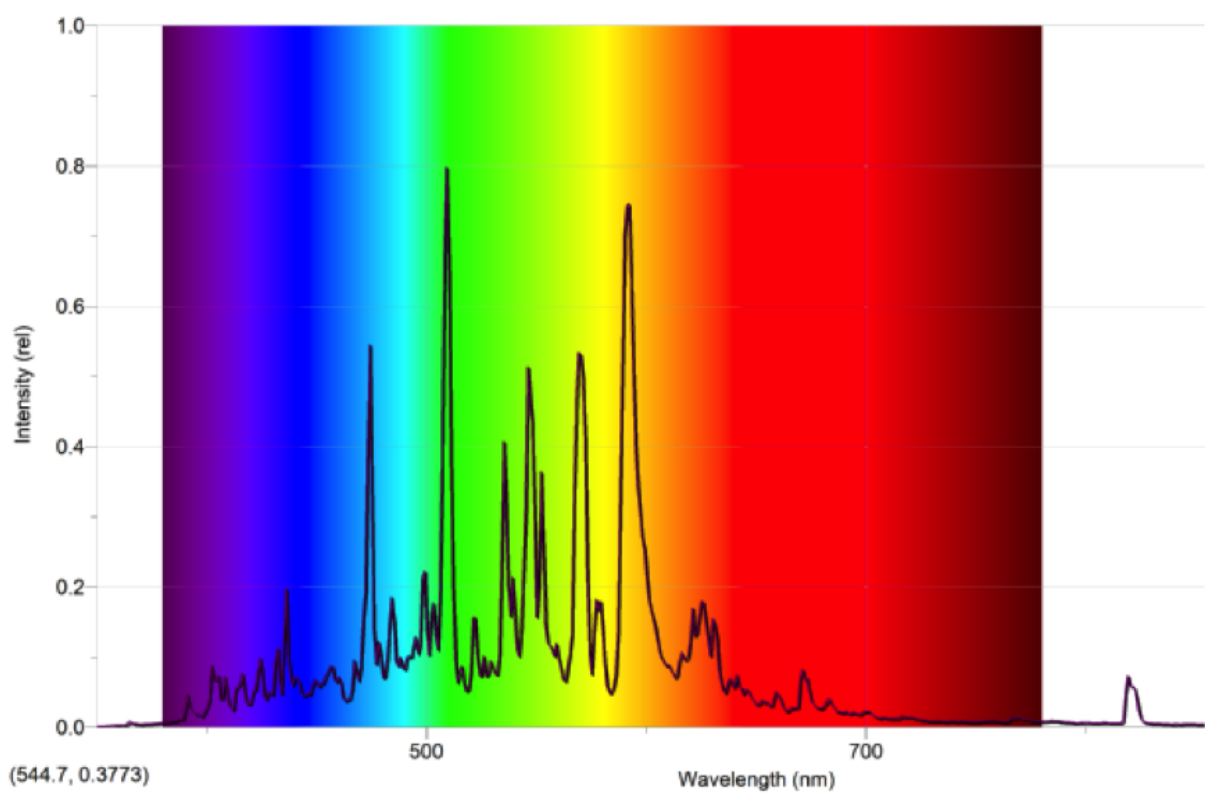


Figure 7: The spectrum taken at the Fry's Gas Station on Grant and Euclid.

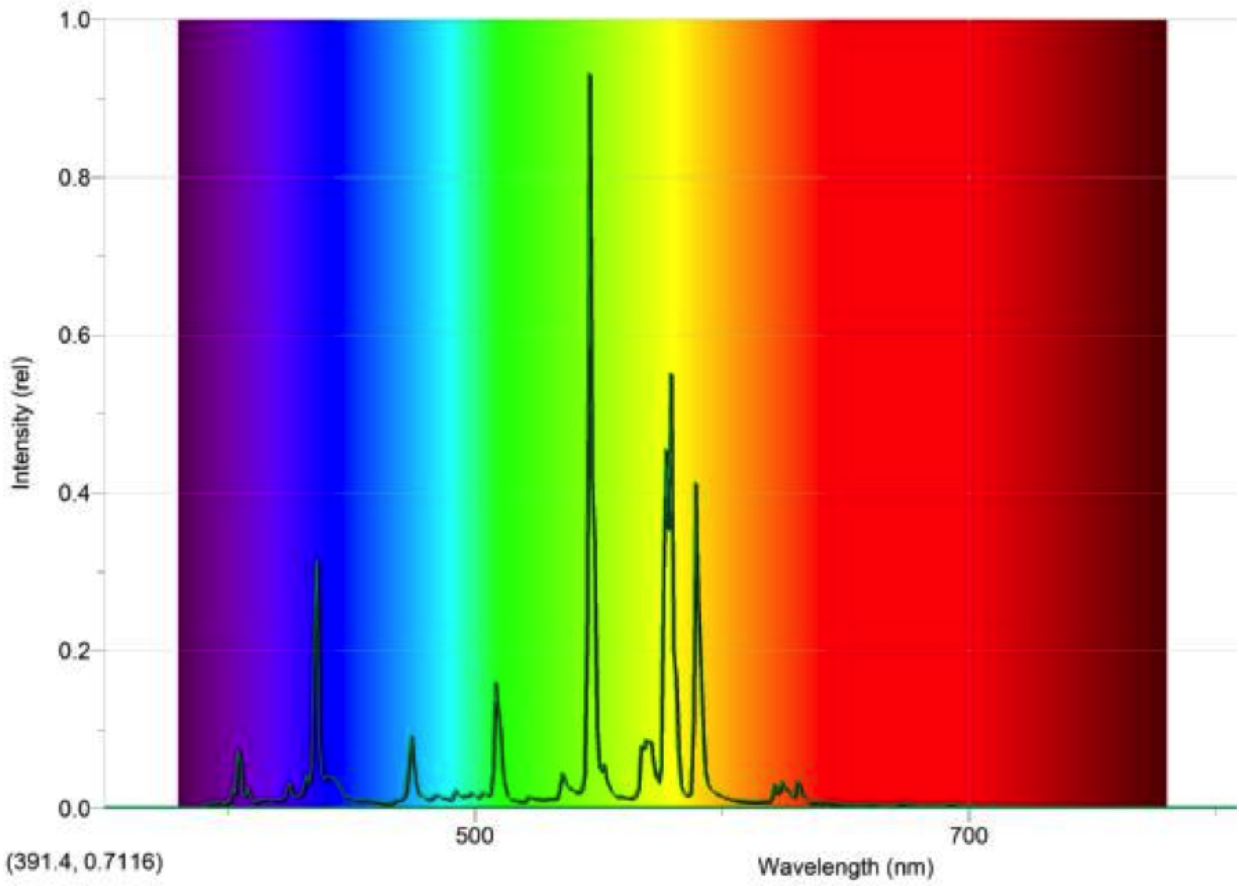


Figure 8: The spectrum taken at the Shell Gas Station on Speedway and Columbus.

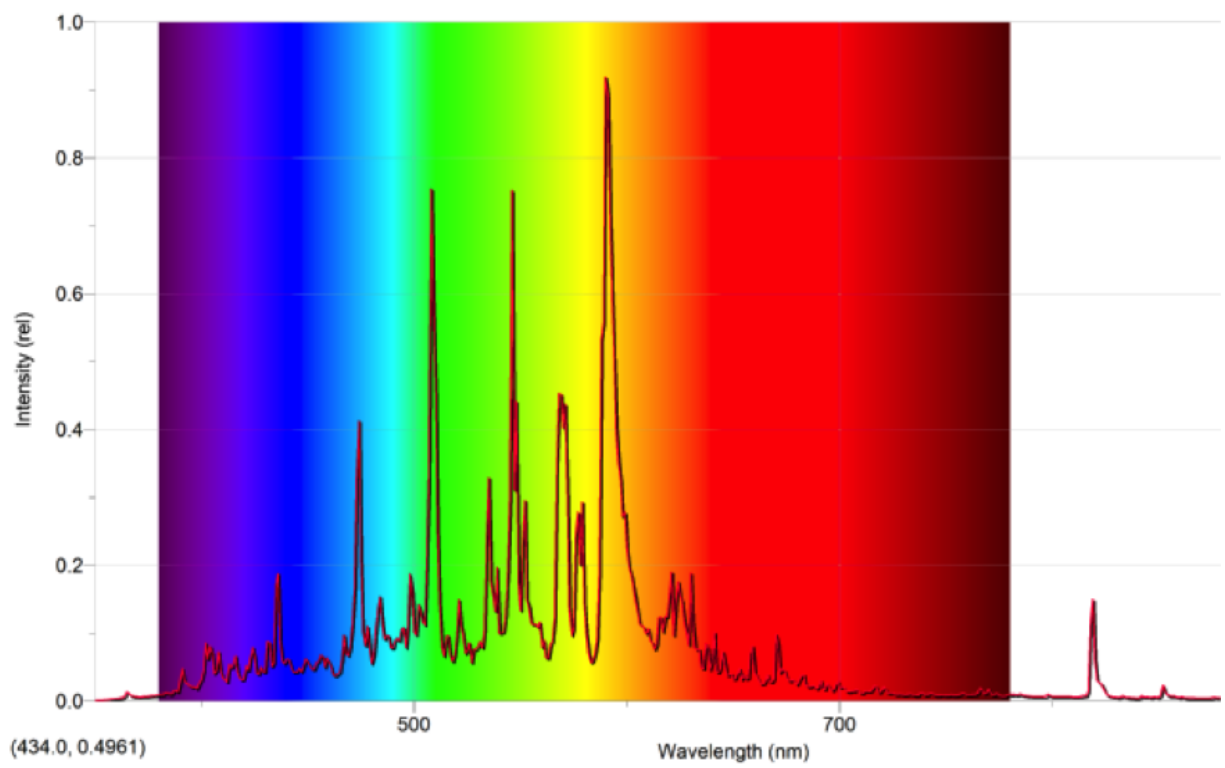


Figure 9: The spectrum taken at the Giant Gas Station on Grant and Stone.

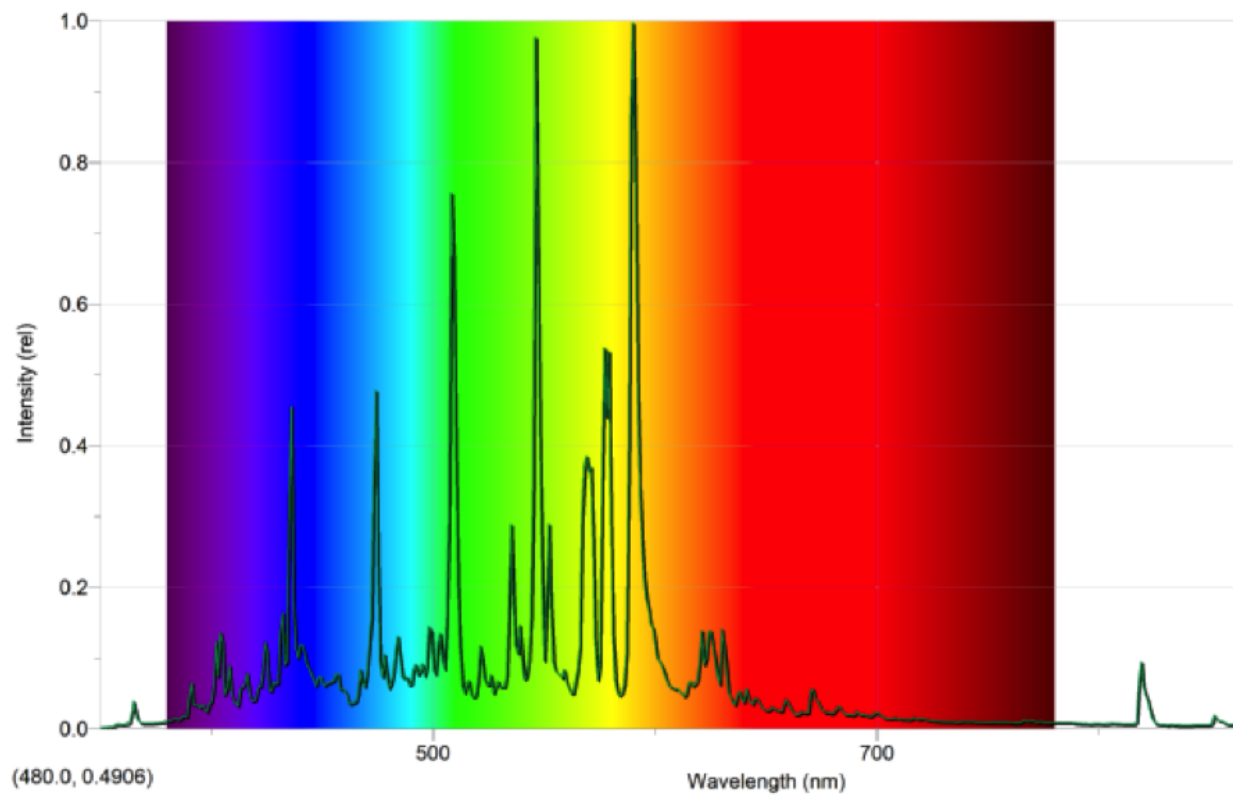


Figure 10: The spectrum taken at the Shell Gas Station on Grant and Euclid.

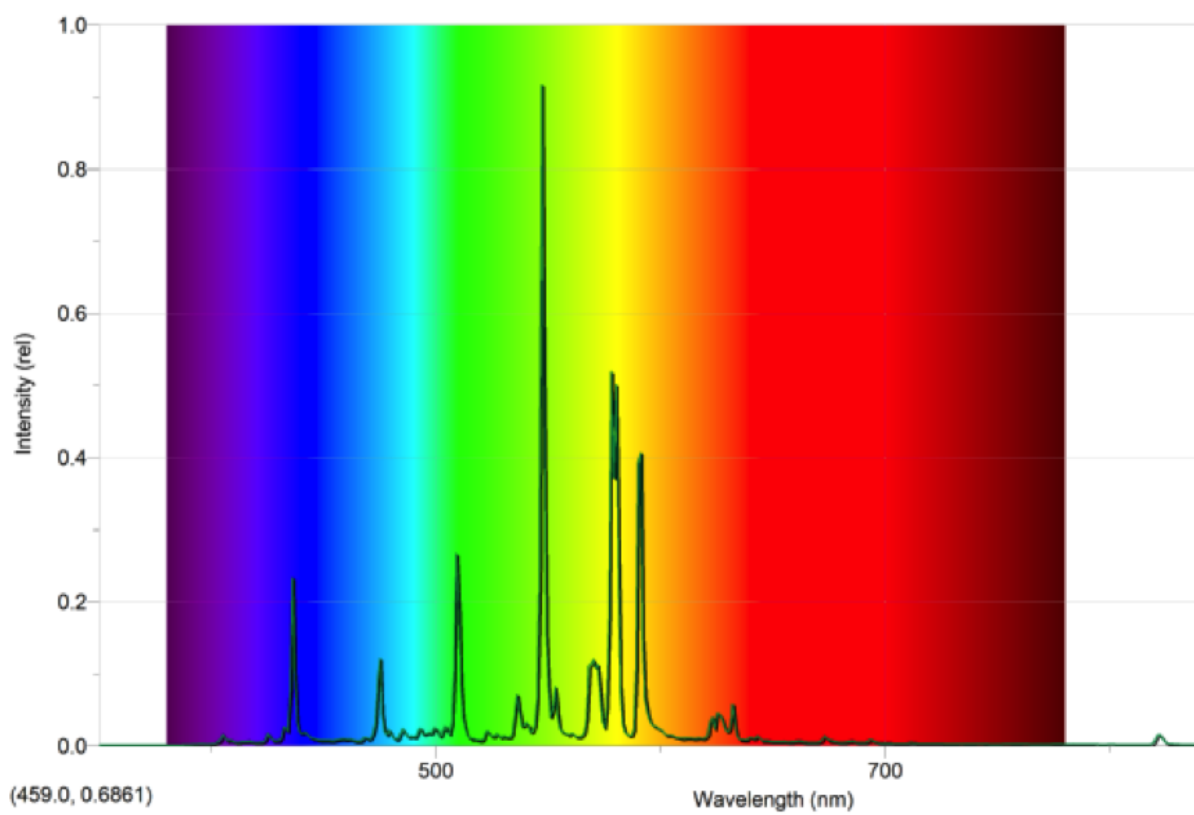


Figure 11: The spectrum taken at the Chevron Gas Station on Grant and Tucson.

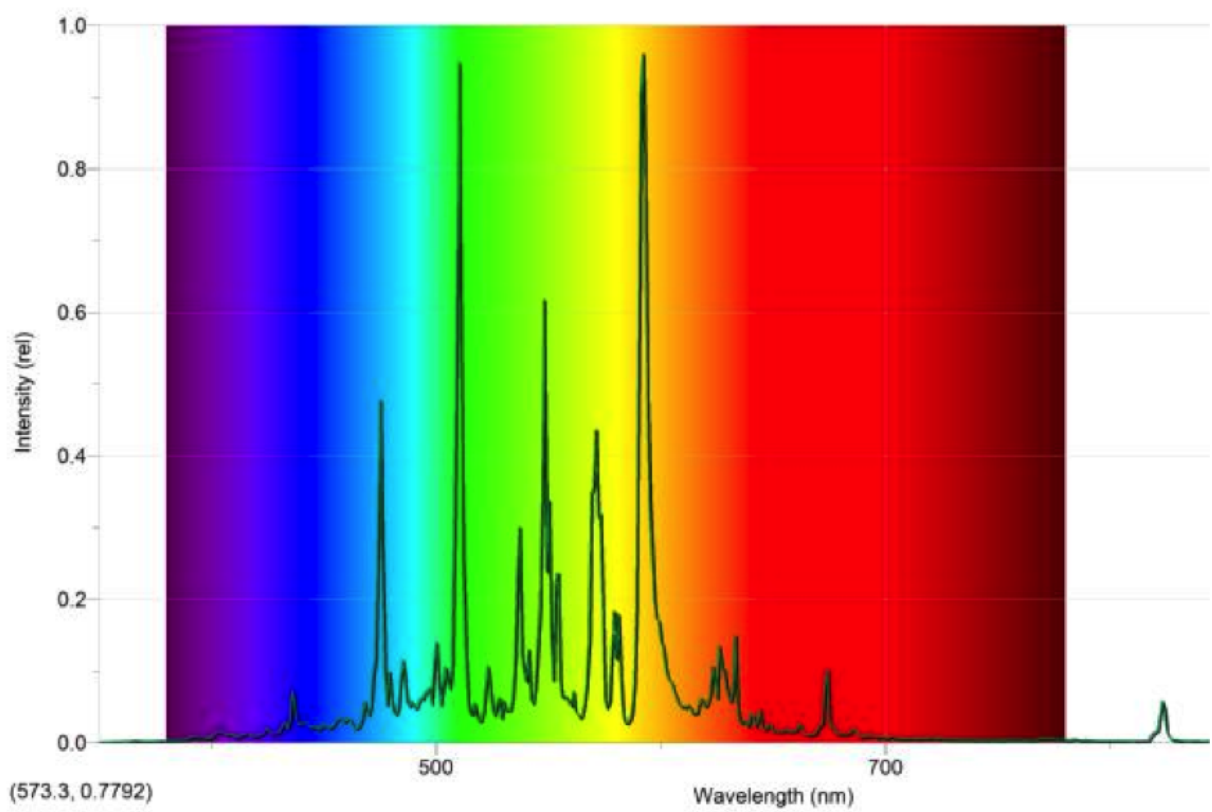


Figure 12: The spectrum taken at the Quebedeaux Buick GMC on Speedway.

ANALYSIS OF THE PHOTOMETRIC ACCURACY OF THE PHAST IDL PROCEDURE

N. W. Kutsop¹

KPNO REU 2013 and Northern Arizona University

Advisors: Dr. K. J. Mighell², Dr. L. Allen², M. Trueblood³

¹ Department of Physics and Astronomy, Northern Arizona University, Flagstaff, Arizona 86011–6010,

² National Optical Astronomy Observatory, 950 North Cherry Avenue, Tucson, AZ 85719

³ Winer Observatory, P.O. Box 797, Sonoita, AZ 85637

ABSTRACT

PhAst (Photometry and Astrometry) is an IDL program designed to solve for the photometry and astrometry of near Earth objects (NEOs) observed by ground-based telescopes. The goal of PhAst is to simplify the observation of NEOs and the reporting of their characteristics to the International Astronomical Union's Minor Planet Center with a focus on NEO astrometry. In this work, we compare the photometric results of PhAst against results from using the photometry procedures in the Image Reduction and Analysis Facility (IRAF) on CCD observation of Landolt standards. We found the photometry produced by PhAst to be nearly identical to the photometry derived using IRAF.

INTRODUCTION

PhAst is the product of the NOAO/KPNO Research Experiences for Undergraduates (REU) Program, which is funded by the National Science Foundation (NSF) REU program. Morgan Rehnberg extended the capabilities of the IDL program ATV to simplify real-time data reduction of NEOs after they have been discovered (Rehnberg et al. 2011, Mighell et al. 2012). Like ATV, PhAst can read FITS images and display them. In addition to displaying the image, PhAst offers the user a graphics user interface (GUI) to manipulate the image. This includes allowing the user to remove biases, divide by flats, align images, blink images, and overlay information about the sources onto the image, compute astrometry, and photometry, along with many more options.

PhAst was designed for Trueblood's post-discovery NEO observation project (Trueblood, Crawford, & Lebofsky 2010). NEOs are asteroids with a perihelion less than 1.3 AU. NEO follow up astrometric observations are important after a NEO's discovery because NEOs are often discovered in a brief window at the object's opposition, when it is at its brightest. The object quickly leaves opposition and by that time only a few observations may be available to use in determining the object's ephemeris. A short observational history typically leads to a poorly constrained orbit and to large uncertainty in the ephemeris. To determine whether or not an object poses any danger to the Earth, we must have a good understanding of the orbit of the object. NEO follow-up astrometric observations enable better constraints to be placed on a NEO ephemeris and orbit. This information can then be used by the International Astronomical Union's Minor Planet Center (MPC) to determine whether an object is an ordinary NEO, a Potentially Hazardous Asteroid (PHA), or a Virtual Impactor (VI). A PHA has Minimum Orbital

Intersect Distance (MOID) < 0.05 AU. A VI has observations, with error bars, that has a possible orbit that intersects Earth's orbit.

The purpose of this project was to determine the accuracy of PhAst as a photometric tool and compare it against another well-accepted photometric tool. For this comparison, we used NOAO's Image Reduction and Analysis Facility (IRAF) (Tody 1986) and its packages of photometry procedures. We also compared PhAst against the USNO-B1.0 catalog (Monet et al. 2003) and Landolt standards, and then compared IRAF measurements against the same catalogs to determine how well each program did against the standard data.

PHAST PHOTOMETRY

Since PhAst was first written in 2011, the photometry has been greatly improved by Robert Crawford. The system he used for PhAst to compute an object's photometry is

$$v = V - Z_{pt} + \text{transCoeff} * \text{transTerm} + [k' + k'' * (V - I)] * X, \quad (1)$$

where v is the instrumental magnitude, $(V-I)$ is the color of the star, V is the standard magnitude, Z_{pt} is the zeropoint for the image, transCoeff and transTerm are the transformations terms from local to standard pass bands, k' and k'' are the extinction coefficients, and X is the airmass at the time of observation.

To calculate the magnitude of any source in the field, PhAst first determines the instrumental magnitude using aperture photometry. PhAst uses the IDL routine `aper.pro`, which is the IDL version of the IRAF aperture photometry package DAOPHOT (Stetson 1987). The user selects a star in the image and PhAst uses `aper.pro` to place measurement apertures around the star. Then `aper.pro` subtracts the median background level as determined by the sky annulus from the flux contained in the aperture.

PhAst determines the standard magnitude of the star by applying the zeropoint term, extinction coefficients and filter transformations given in Equation 1. PhAst can solve automatically for the zeropoint term, using SExtractor (Bertin & Arnouts 1996), SCAMP (Bertin 2006) and the Guide Star Catalog (GSC-2.3.2; Lasker et al. 2008) by matching instrumental magnitudes for field stars in the image to the standard magnitudes in the catalog. The extinction coefficients are written into the PhAst configuration files. Each observatory has their own extinction coefficients which depend on many variables but an observatory's extinction coefficients typically do not change much from night to night. Like the extinction coefficient, the transCoeff and transTerm terms are known for the conversion from the local filters at the telescope to standard filters. The $(V-I)$ color of the star is taken to be a nominal value and can be edited by the user – if they decide to do so. The image header of our CCD observations has the value of the airmass.

PhAst takes all these variables, uses Equation 1, and then uses a weighted linear regression algorithm to determine the zeropoint (Z_{pt}) of the image. This zeropoint can be used with Equation 1 for the rest of the image to determine the standard V magnitudes of objects that are not in standard catalogs (e.g., asteroids).

PROCEDURE

In order to test the accuracy of PhAst's photometry we compared it to another well-accepted photometry program. We chose to use IRAF and its photometry packages as it has been used extensively since its development in the 1990's and is well regarded as an accurate photometry tool. Using both PhAst and IRAF, we examined the same standard star field.

We now describe our methodology. First, we would use PhAst in its default state to automatically output the stellar magnitudes as described below. We would then use IRAF in conjunction with the classic method of determining a star's standard magnitude. Using the classic method we would determine every variable by hand and every variable's associated error. This way we could methodically follow through the comparison process and if the comparison was less than ideal we could then show why it was not due to IRAF's contribution.

For this process the star field we chose was the Landolt (1992) standard field PG1323, displayed in Figure 1. We used a Landolt field because they provide excellent photometric calibrations.

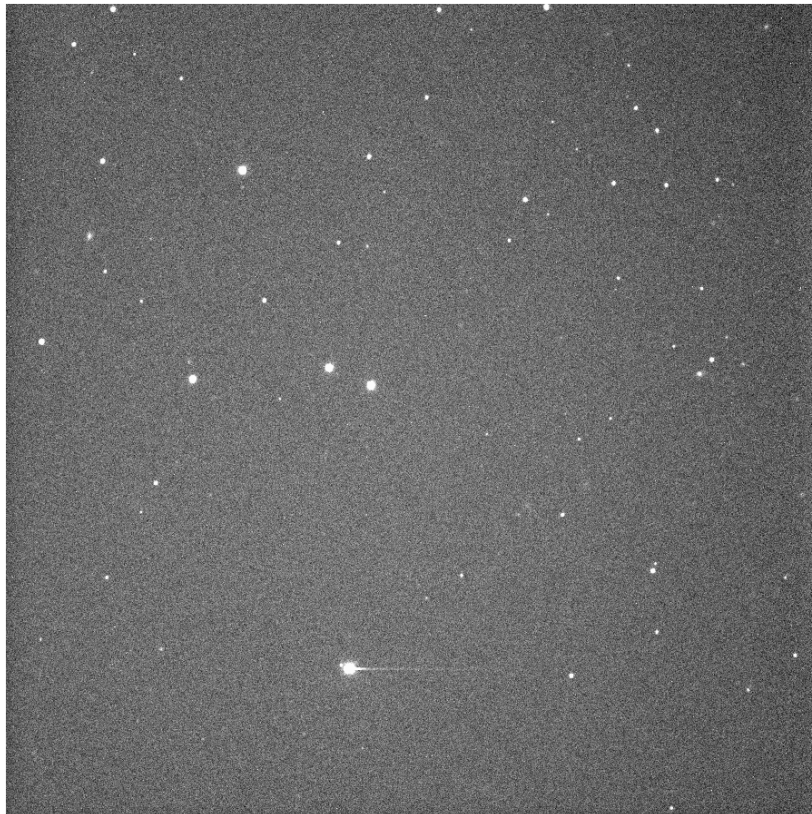


Figure 1: Landolt standard field PG1323-86. This image was taken by Trueblood et al. in April of 2012 at the 2.1-meter telescope at Kitt Peak National Observatory. The five bright stars from top to bottom and left to right are the center star PG1323, then PG1323C, PG1323A, PG1323B, and PG1323D.

This field was observed over the course of two nights, April 9–10, 2012, at the 2.1-meter telescope at the Kitt Peak National Observatory. In total between those nights there were nearly 300 images taken in the V, R, B, and Clear (“white” BK7 filter) passbands. Landolt (1992) reported the magnitudes of stars in the standard V filter along with multiple color indexes. We analyzed only the V and R observations. From the 300 images we chose the 6 images that were (1) photometric or nearly –photometric, (2) had no trailed stars, and (3) were taken with either the V or R filter. In these 6 images there are 5 stars, PG1323, PG1323-A, PG1323-B, PG1323-C, and PG1323-D, which had their magnitudes computed by Landolt. For this project we only used PG1323 (from here out referred to as PG1323-X, or X), PG1323-B (B), and PG1323-C (C). We did not use D because it is consistently saturated in our images, as can be seen in Figure 1 by the trail of light coming off of it heading towards the right. We also did not use A, because A is likely a variable star. When we did include it our calculations it returned large errors and unrealistic plots.

IRAF CALCULATIONS

We began our comparison by using IRAF’s aperture photometry package DAOPHOT to determine the instrumental magnitudes of the 3 stars throughout the 6 images. Using the parameters within DAOPHOT, we set the aperture to a 10-pixel radius, the inner sky radius to 20 pixels, and the outer sky radius to 30 pixels. An example of this can be seen in Figure 2.

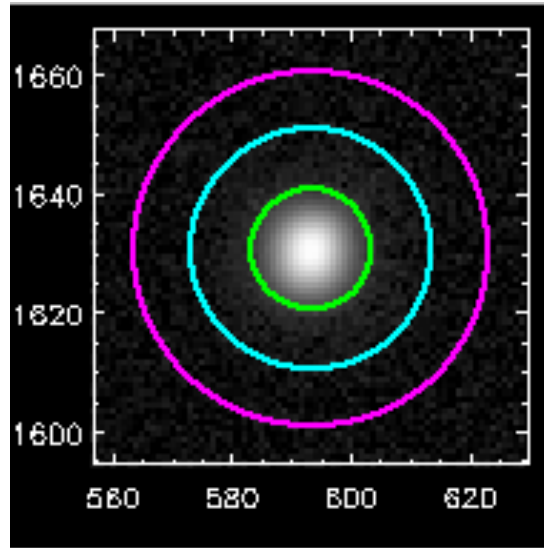


Figure 2: Aperture and annulus around the center star, PG1323 (green). The aperture at 10 pixels in radius (blue). The inner sky annulus at 20 pixels in radius (magenta). The outer sky annulus at 30 pixels in radius.

In total this generated 17 instrumental magnitudes at varying airmasses and in both filters. Using these instrumental magnitudes we determined their extinction coefficients with

$$v_0 = v_x - k_v X, \quad (2)$$

$$r_0 = r_x - k_r X, \quad (3)$$

where v_0 and r_0 are the instrumental magnitudes at a zero airmass in the V and R band respectively, v_x and r_x are the instrumental magnitudes as measured by IRAF, k_v and k_r are the

extinction coefficients in the V and R band respectively, and X is the airmass at the time the image was taken.

To determine the extinction coefficients we compared each star in its filter at a given airmass against the same stars in the same filter at a different airmasses:

$$k_v = \frac{v_{x1} - v_{x2}}{X_1 - X_2}, \quad (4)$$

where the 1s and 2s denote the instrumental magnitude with its corresponding airmass. We used Equation 4 for every combination of stars at each air mass in each filter.

Once every combination of star had been exploited we took the average of each calculation for each star to determine our estimate for the extinction coefficients of each star. To determine our error for these extinction coefficients we calculated their standard deviation using this method

$$\sigma_k = \sqrt{\frac{\sum_{i=1}^n (k_{avg} - k_{vi})^2}{n - 1}}, \quad (5)$$

where σ_k is the standard deviation of the extinction coefficient for each star, n is the total number of extinction coefficients used towards the mean extinction coefficient calculation, k_{avg} is the mean extinction coefficient of that star, and k_{vi} is one of the particular extinction coefficients calculated through some combination of instrumental magnitudes at different airmasses. We then took the mean extinction coefficients for each star in each filter and determined the true mean extinction coefficient for the two filters.

To calculate errors for means such as when we calculated the extinction error we used this equation:

$$\sigma = \frac{\sqrt{\sum_{i=1}^n a_n^2}}{n}, \quad (6)$$

where σ in this case is the error associated with the mean, where n is the total number of components used towards the calculation of the mean, and a_n are the components used towards the mean calculation. Equation 6 was used for calculating the error for the final extinction coefficients.

We then took these extinction coefficients, k_R and k_V , and used them in Equations 2 and 3 to determine the instrumental magnitude at zero airmass for each star at each associated airmass. To determine the errors for the instrumental magnitude we first calculated the error from multiplying the airmass with the extinction coefficient with

$$\sigma_c = \sigma_a * B, \quad (7)$$

where σ_a is an associated error for some measured value A and B is a constant. For our purposes, A would be the extinction coefficient and B would be the airmass. We then took the error derived from Equation 7 and used it towards our final error calculation using

$$\sigma_c = \sqrt{\sum_{i=1}^n \sigma_n^2} , \quad (8)$$

where σ_n is the error associated with the respective measured value. In this case, this would be the error associated with subtracting $k_v * X$ from v_x . We find the error by squaring the associated errors, summing them, and taking the square root of their sum. We then took the instrumental magnitude at a zero airmass for each star at each associated airmass and calculated the mean instrumental magnitude at a zero airmass for each star. We calculated the average error using Equation 6.

Using the instrumental magnitudes at a zero airmass that we determined, we now derived the remaining transformation variables necessary to transform an instrumental magnitude into a standard magnitude. To do this we used the transformation equations

$$V - v_0 = A1_v(V - R) + A2_v , \quad (9)$$

$$R - r_0 = A1_r(V - R) + A2_r , \quad (10)$$

$$(V - R) = B1(v - r)_0 + B2 , \quad (11)$$

where V is the magnitude of the star as calculated by Landolt (1992), A1 is the color term coefficient, A2 is the zeropoint, (V-R) is the color of the star as calculated by Landolt (1992), $(v - r)_0$ is the color as calculated by us using the instrumental magnitudes at a zero airmass, B1 the other color term, and B2 is the transformation term. R is the expected magnitudes of the stars in the R band as if Landolt measured them. Landolt (1992) reported the V magnitudes and colors of his standard stars. Using Landolt (V-R) colors, one can determine the R magnitude. Landolt also reported errors, so to determine the errors for our R magnitudes, we used Equation 8 along with the errors for V and the errors for (V-R).

To determine the first variables, $A1_v$ and $A1_r$, we used one star and calculated it against another one of the three stars in the same filter. For the V filter this looks like

$$A1_v = \frac{(V - v_0)_1 - (V - v_0)_2}{(V - R)_1 - (V - R)_2} , \quad (12)$$

where the 1s and 2s denote the individual stars. We used Equation 12 for every combination of stars in each filter.

To determine the error for each combination, we applied the usual rules for error propagation, using Equation 8 when adding or subtracting and Equation 13 when multiply or dividing.

$$\sigma_c = C \sqrt{\sum_{i=1}^n \left(\frac{\sigma_n}{a_n}\right)^2} , \quad (13)$$

In Equation 13, σ_n is the error associated with the respective measured value. After using Equation 8 to determine the errors from the subtractions, we used Equation 13 to propagate the errors for A1. We then took the mean value for each combination of stars in each filter and determined the mean A1 for each filter. We calculated the mean error with Equation 6. We then used these values back into Equations 10 and 11 and determined the average A2s for each filter. To calculate the error for the A2s we used a combination of Equations 13 and 8 where applicable.

To calculate B1, we developed similar formula derived from Equation 11. We used this format for each combination of stars and calculated the error for B1 in the same manner we calculated the error for A1, using a combination of Equations 13 and 8 where applicable. Once we had a B1 and an associated error for each star combination we took the mean of the combinations and used Equation 6 to determine the mean error. Once we calculated the mean value for B1 we used B1 back into Equation 11 to determine the mean B2 value. To determine the error for B2 we used the same method used to determine A2, using a combination of Equations 13 and 8 where applicable.

PHAST AND IRAF COMPARISON

Now that we had calculated all the variables needed to transform an instrumental magnitude from IRAF to a standard magnitude, we compared PhAst's photometry against IRAF's photometry. For these comparisons we reexamined all 6 images and looked for more stars. As seen in Figure 1, there are far more stars than just the five Landolt stars. To determine which stars on the fields to use, we used PhAst's option to overlay information about a star onto the image. Using this feature we had PhAst query the USNO-B1.0 catalog and overlay circles only on stars with an standard magnitude of $R = 18$ or brighter according to the USNO-B1.0 catalog. We initially chose this range as anything much fainter than $R = 18$ started to become faint in the image and were difficult for us to see by eye. We then examined each star in each image that PhAst had labeled as having an R magnitude of 18 or less to determine these stars' signal-noise-ratio (S/N). PhAst has a built in procedure to determine S/N and to determine the S/N as according to IRAF we used

$$\frac{S}{N} = \frac{F * G}{\sqrt{(F * G + N_{pix} * M_{sky} * G + N_{pix} * R_{app}^2)}} , \quad (14)$$

where F is the flux of the object as determined by IRAF, G is the gain, N_{pix} is the number of pixels within the aperture, M_{sky} is the median value of the sky pixels, and R_{app} is the radius of the aperture. Using both IRAF and PhAst we found most stars to have a signal-to-noise ratio between 70 and 100. Our brightest stars, like the five Landolt stars, had a S/N value ratio of 500 or more. The faintest star we included was 0811-0255582, which can be seen in the lower left hand corner of Figure 3, which had a S/N value of 30.1 according to PhAst and a S/N value of 26.328 according to our calculations from IRAF. We believe that all of these stars have a large enough S/N to be used towards our photometry comparisons.

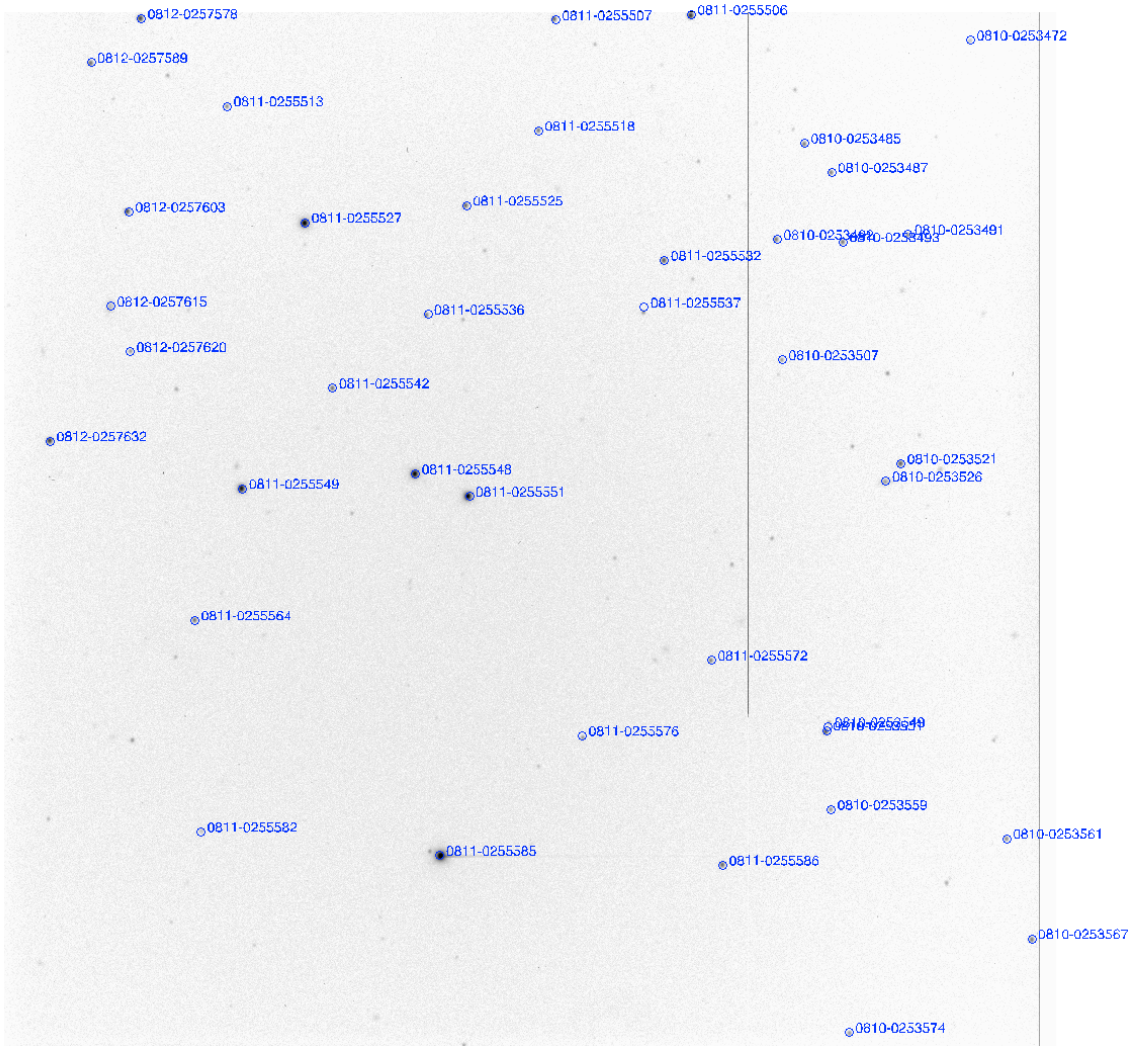


Figure 3: One of the six images used towards the comparison between PhAst and IRAF. This particular image is one of the 3 images taken in the V band. Every star in the image with a circle around it is a star with an R magnitude equal to or below 18 as reported by the USNO-B1.0 catalog. The names next to each star are the names as given by the USNO-B1.0

In total there were 42 stars occurring in either 5 or all 6 of the images. Some stars only appeared in 5 images because the images were not taken with the same center RA and Dec. As described earlier, for the comparisons we used PhAst in its default state to measure automatically the standard magnitudes. For IRAF however, we measured the instrumental magnitudes of each of the 42 stars and using the variables we calculated in the previous section along with Equations 2, 3, 9, 10, and 11 we transformed these instrumental magnitudes into standard magnitudes.

We took the average for any star that occurred in multiple images in the same filter. Basically if one of the 42 stars in the 3 V filter images had occurred in all 3 of the images we would have 3 standard magnitude measurements for that star. We took all 3 of those measurements and computed the average standard magnitude for that star. We then determined the error associated with that average standard magnitude using Equation 6. We did this for both the measurement from PhAst and IRAF, correcting for airmass.

We first compared the instrumental magnitudes from PhAst versus those from IRAF. Since PhAst and IRAF use essentially the same algorithm for determining the instrumental magnitudes, we expected that the measurements would have a one-to-one ratio. We then compared the standard magnitudes from PhAst versus those from IRAF. In both of these comparisons we included all the stars in both filters, for a total of 84 stars. Figures 4 and 5 are the plots of these two comparisons.

We then took just the 5 stars from Landolt (1992) and compared Landolt's measurements against our measurements using PhAst on the 5 stars and then again against our measurements using IRAF on the 5 stars. We chose to use all 5 stars in these comparison instead of just the 3 stars we had previously used because our concern was not with how well our measurements compare to Landolt's, though it is due some consideration, our concern is with how well PhAst compares to Landolt as compared to how well IRAF compares to Landolt. Basically if both ratios, Landolt vs. PhAst and Landolt vs IRAF, are similar then this would support the conclusion that PhAst is as good as the classic method; if the ratios are different this would be evidence against that claim. Again we include the measurements from both filters for a total of 10 stars.

We then took all the stars in just the R band and used the USNO-B1.0 catalog's measurements for the stars standard magnitudes and compared those values against those we measured using PhAst and again against those we measured using IRAF. This time we only used the R magnitudes because the USNO-B1.0 only reported their measurements in the R band.

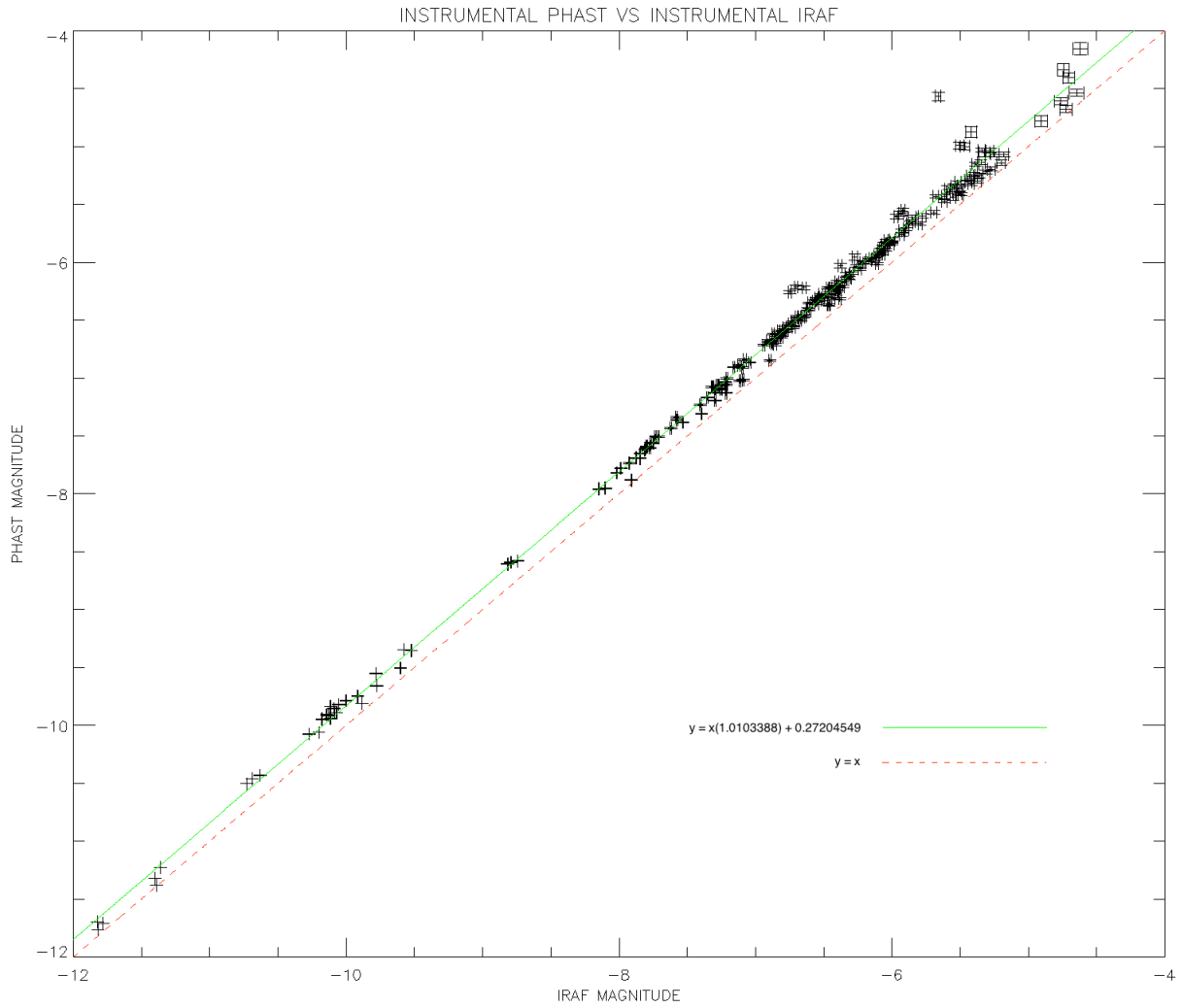


Figure 4: The instrumental magnitudes as measured by PhAst plotted against the instrumental magnitudes as measured by IRAF. Both the R and the V magnitudes are presented in this plot. In total there are 84 data points, 42 from each filter, each representing a star of R magnitude 18 or brighter. The red dashed line represents a fit with a one-to-one ratio and no offset. The green solid line represents the best fit to the data as determined by IDL. Ideally we would want the green solid line to lie exactly on top of the red dashed line. The equations for the red dashed line and the green solid line are displayed on the graph next to their respective line samples.

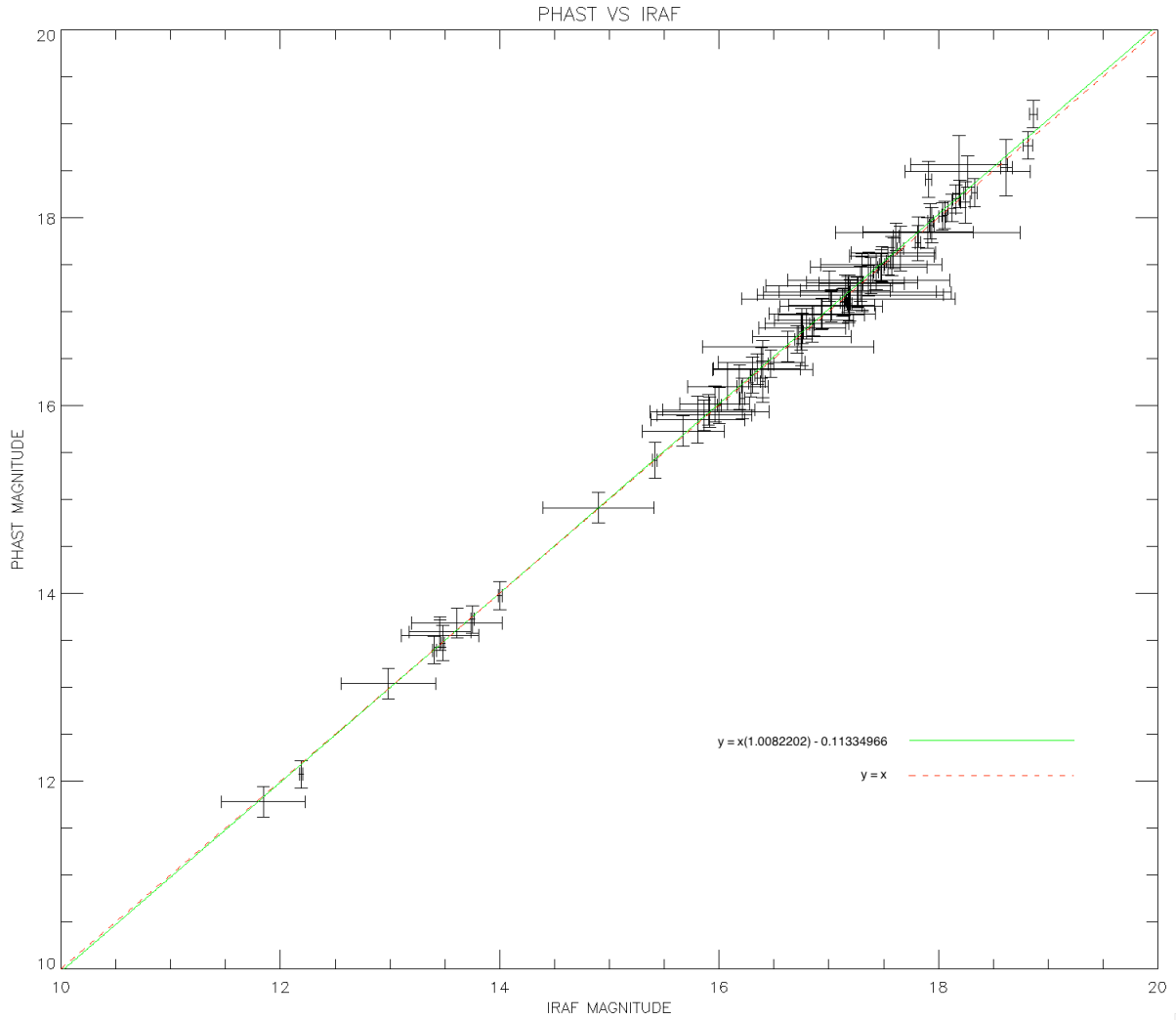


Figure 5: The standard magnitudes as measured by PhAst plotted against the standard magnitudes as measured by our classic approach. Both the R and the V magnitudes are presented in this plot. In total there are 84 data points, 42 from each filter, each representing a star of R magnitude 18 or brighter. The red dashed line represents a fit with a one-to-one ratio and no offset. The green solid line represents the best fit to the data as determined by IDL. Ideally we would want the green solid line to lie exactly on top of the red dashed line. The equations for the red dashed line and the green solid line are displayed on the graph next to their respective line samples.

RESULTS AND DISCUSSION

As can be seen in Figure 4 the slope of our best fit line to our data is 1.0103388 – very nearly one. This means that on average PhAst is measuring the same instrumental magnitude as IRAF within about 1%. This result was expected as both tools use the essentially the same algorithm to determine the instrumental magnitudes. We expected the intercept of this line to be very near zero and while it is close there is a noticeable offset when compared against the red dashed line that represents a perfect fit with a slope of one and an intercept of zero. A possibility for this offset is that PhAst and IRAF set their apertures and sky annulus radii in different ways. For IRAF the aperture and sky annulus we used was fixed for all the measurements, every source was measured using an aperture of 10 pixels, an inner sky annulus at 20 pixels, and an outer sky annulus at 30 pixels. PhAst on the other hand uses a neural network to decide what is the best aperture and sky annulus to use for each source. This was described in detail in the PHAST PHOTOMETRY section. This means nearly every source had a different aperture and sky annulus used for the instrumental magnitude measurement. This was also likely the cause of the significant outliers in our data. Those were probably galaxies or extended sources which the neural network had difficulty handling.

In Figure 5 the slope of our best fit line to our data is very nearly 1. In this plot the slope of our line is 1.0082202 – even closer to one than that of plot in Figure 4 for the instrumental magnitudes. The intercept of our best-fit line is also now closer to zero. This means that PhAst is measuring the standard magnitudes almost identically to IRAF, again within about 1%. When we compared the standard magnitudes as seen in Figure 5 we noticed that comparison was more similar than when we compared the instrumental magnitudes in Figure 4. We believe this is because the differences in the apertures and annulus, which likely gave rise to the offset in Figure 4, was removed or accounted for within our zeropoint, color term, and transformation term calculations. We would expect this as the standard magnitudes should not depend on the apertures used to calculate their instrumental magnitudes.

For our comparisons between Landolt-and-PhAst, and Landolt-and-IRAF we used IDL to determine the relationship in the data by fitting a linear best fit to the data. For these comparisons the slopes of the best fit lines are respectively 0.98038448 and 1.0391524 – noticeably farther from one. However both slopes are nearly the same offset from one. This fact is significant because it shows that while both PhAst's results and IRAF's results are not exactly similar to those of Landolt, they are both dissimilar in a similar way. Basically that means that while neither is perfect when compared to Landolt they are either just as good (or bad) when compared to Landolt. This gives evidence to the claim that PhAst is as good as IRAF. A possible explanation for the offset is that we included bad data in the form of the 4 data points from PG1323-A and PG1323-D. Another possibility is that we are seeing a difference in the level of accuracy that the original data was taken with. Landolt's data was taken under the best of conditions with the goal of retrieving very clear and accurate photometry measurements. Our data, on the other hand, was obtained under less than perfect photometric conditions. While these

comparisons are not identical, they are still close and are in good agreement compared to Landolt's data.

In the final two comparisons, we compare USNO-B1.0-and-PhAst, and USNO-B1.0-and-IRAF. In these comparisons the slopes of the best fit linear lines to the data are respectively 0.90484384 and 0.91641534 – even further from a slope of one. Once again they are nearer to one another than they are to one. These results are very similar to the comparisons between Landolt-and-PhAst, and Landolt-and-IRAF. We see again that while both PhAst's results and IRAF's results are not exactly similar to those of the USNO-B1.0, they are both dissimilar in a similar way. This further supports the claim that PhAst is as good as IRAF.

CONCLUSION

From our results we can conclude that PhAst is indeed comparable to IRAF and the classical approach to determining the magnitude of an object. When we compared them against one another they were nearly identical. When we compared them to the catalogs they were offset from the catalogs but these offsets were nearly identical. The fact that these offsets were nearly identical in either catalog strongly suggests that both programs yield comparable results.

Of note though is how long each method took to go from the raw data to a plotable standard magnitude. Using PhAst just as it was in its default setting took roughly 2 hours to go from the raw frames to our standard magnitudes. Using the classic method on the other hand, including calculating all the zeropoints, color terms, transformation terms, and all the associated errors for everything took at least 3 weeks. A significant portion of those 3 weeks were devoted to propagating errors and determining the transformation variables, but those were all necessary to compare PhAst against a tried and true method with everything solved for from the ground up with good precision. The fact that PhAst can produce similar results in a few hours to the results done by hand over the course of 3 weeks should be taken into account when evaluating the usefulness of PhAst.

Our overall evaluation and conclusion on PhAst's photometry is that it is very good. In terms of what PhAst is used for, its photometry is more than good enough for asteroid observations. Since PhAst's photometry is already good for a photometric program, when the photometry is considered secondary as in the case of typical NEO astrometric observations, then the accuracy of PhAst's photometry is more than sufficient.

Possibilities for improving PhAst's photometry could include the application of elliptical apertures instead of the circular ones currently being used. Sometimes during these asteroid observations, the asteroid will get trailed, when that occurs it is difficult to use circular apertures on the asteroids. Elliptical apertures on the other hand could allow the user to more accurately determine magnitude of an asteroid. Another improvement is to prescribe that observers obtain images of both their target asteroids and of standards star

fields, such as our Landolt field. These observations taken between asteroid observations can be used towards better calibration of the zeropoint in Equation 1. However whether or not the photometry of these asteroids is critical will be determined by the observer and by their individual project goals. If the photometry is critical than likely the photometry of PhAst is already good enough but these suggestions could be utilized to further improve PhAst's photometry.

ACKNOWLEDGEMENT

Kutsop was supported by the NOAO/KPNO Research Experiences for Undergraduates (REU) Program which is funded by the U.S. National Science Foundation's Research Experiences for Undergraduates Program (AST-1262829).

REFERENCES

- Bertin, E. 2006, *Astronomical Data Analysis Software and Systems XV*, 351, 112;
Automatic Astrometric and Photometric Calibration with SCAMP.
- Bertin, E., and Arnouts, S. 1996, *A&AS*, 117, 393;
SExtractor: Software for source extraction.
- Landolt, A. U. 1992, *AJ*, 104, 340;
UBVRI photometric standard stars in the magnitude range 11.5-16.0 around the celestial equator.
- Lasker, B. M., Lattanzi, M. G., McLean, B. J., et al. 2008, *AJ*, 136, 735;
The Second-Generation Guide Star Catalog: Description and Properties.
- Mighell, K. J., Rehnberg, M., Crawford, R., Trueblood, M., and Lebofsky, L. A. 2012, *PASP*, 124, 1360;
PhAst: And IDL Astronomical Image Viewer Optimized for Astrometry of Near Earth Objects.
- Monet, D. G., Levine, S. E., Canzian, B., et al. 2003, *AJ*, 125, 984;
The USNO-B Catalog.
- Rehnberg, M., Crawford, R., Trueblood, M., Mighell, K. 2011, American Astronomical Society, AAS Meeting #219, #145.02;
PhAst: A Flexible IDL Astronomical Image Viewer.
- Stetson, P. B. 1987, *PASP*, 99, 191;
DAOPHOT - A computer program for crowded-field stellar photometry
- Tody, D. 1986, *Proc. SPIE*, 627, 733;
The IRAF Data Reduction and Analysis System.
- Trueblood, M., Crawford, R., and Lebofsky, L. A. 2010, NOAO Proposal ID #2010B-0030;
Long-Term Follow-up of Near Earth Objects.

Studying Light Pollution in and around Tucson, AZ

KPNO REU Summer Report 2013

Rachel K. Nydegger

*Utah State University, Kitt Peak National Observatory,
National Optical Astronomy Observatory*

Advisor: Constance E. Walker

National Optical Astronomy Observatory

ABSTRACT

Eight housed data logging Sky Quality Meters (SQMs) are being used to gather light pollution data in southern Arizona: one at the National Optical Astronomy Observatory (NOAO) in Tucson, four located at cardinal points at the outskirts of the city, and three situated at observatories on surrounding mountain tops. To examine specifically the effect of artificial lights, the data are reduced to exclude three natural contributors to lighting the night sky, namely, the sun, the moon, and the Milky Way. Faulty data (i.e., when certain parameters were met) were also excluded. Data were subsequently analyzed by a recently developed night sky brightness model (?). During the monsoon season in southern Arizona, the SQMs were removed from the field to be tested for sensitivity to a range of wavelengths and temperatures. Future work might include further validation of the accuracy and precision of these devices by comparing to the Suomi Visible Infrared Imaging Radiometer Suite (VIIRS) as well as the Globe at Night (GaN) data.

1. Introduction

Though the view of city lights is considered a modern beauty, it is the cause of an assortment of negative effects (?). Most street lights emit light radially, sending large portions of the light into the sky, leaving the ground dim. The excess light - light pollution - directed upwards destroys our ability to view beauty of the night sky and represents a loss of energy and money. An-

imals are often attracted to or repelled by light, disrupting their hunting and mating patterns as well as other behaviors. Similarly, human health is negatively impacted by the the change in circadian rhythm. Studies have shown that women who are exposed to light while working at night have a much higher risk of breast cancer (?). Other negative effects of light pollution include depression, insomnia, and other forms of cancer.

Quantifying the light pollution with housed data-logging Sky Quality Meters (SQMs) can give a sense of how much excess light there is in Tucson, and therefore provides a starting point to address this issue. These meters have a FOV FWHM of 20° and are able to collect data either automatically based on time and darkness or manually through a USB connection. For this project, each SQM takes data every five minutes whenever the sky is darker than 12 mag/arcsec^2 . To better analyze the data collected by these devices, the sensitivity of the devices was tested in regard to various visible wavelengths. Results from these tests called for inspection of the filter inside each SQM and the glass atop the housing of the device.

To focus analysis on anthropogenic light pollution, raw data are reduced through a series of python scripts that remove readings taken when the moon, sun, or Milky Way is overhead. These scripts also remove erroneous readings. The goal of this paper is to present and discuss spatial and temporal trends in the anthropogenic sky glow over Tucson from 2012-2013 using these reduced data.

2. Laboratory Testing

To measure the effect outdoor lighting in Tucson has on light pollution, one SQM is placed at each of the following sites: the National Optical Astronomy Observatory (NOAO), each cardinal point at the outskirts of Tucson, Kitt Peak, Mt. Lemmon, and Mt. Hopkins. Population varies greatly by location, thereby changing the outdoor lighting and, consequently, the sky brightness. Observatories often use low-pressure sodium lights, whereas Tucson contains LED sources, the SQM detector is not as sensitive to. Therefore, knowing how the meter responds to specific wave-

lengths of light assists in interpreting light pollution data.

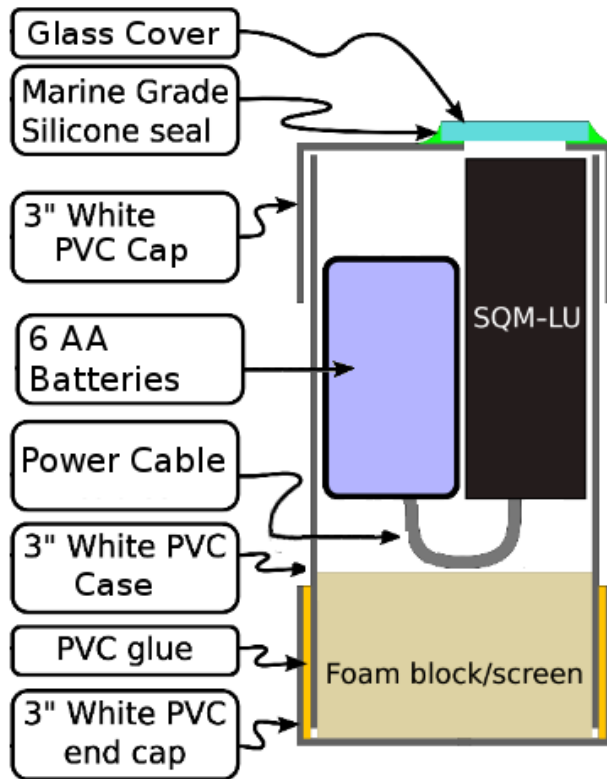


Fig. 1.— Diagram of an SQM

2.1. Wavelength Sensitivity

In order to characterize readings from each SQM, the meters were placed within an integrating sphere to ensure uniform exposure from sources of varying wavelength. Diodes emitting light of wavelengths 365 nm, 470 nm, 570 nm, 655 nm, 770 nm, 850 nm, and 950 nm were used to represent the visible spectrum. The source outputs were held at constant voltages corresponding to SQM readings of approximately 20 mag/arcsec^2 , as described in Table 1. Voltage was reported by a reference sensor inside of the integration sphere. Once the output voltage was stabilized, 25 readings were taken for each SQM with and without housing, cover, and glass filter (see Fig.

1 for a visual representation of these components). Unihedron, the manufacturer of this device, reports that the first reading is often erroneous due to temperature calibration (?), and so it should be removed for the sake of validity. As readings were collected every second, the first five readings were taken out of each data set.

λ (nm)	Voltage (eV)
365	.0400
470	.0435
570	.0810
655	.1030
770	.1160
850	.1190
950	.1470

Table 1: Source output was kept constant to ensure valid data comparison for each wavelength. Output was varied according to wavelength to avoid over-saturation of the SQM detector.

The intensity readings in the integration sphere were dependent upon which each SQM was used, leading to the discovery that the reflectivity of the SQM caps varied. The meters were exposed to different levels of UV radiation at their respective sites, causing the housing of some devices to yellow more than others (see Fig. 2). To address this inconsistency, light masks were made to cover all of the caps except for the openings during laboratory testing. Data collected during this time were not used for error analysis. Eventually, the housings of these SQMs will be coated on the outside with a glossy white paint to prevent UV yellowing and maintain a cool temperature within the case. To reduce light scattering within the housing, the inside of the case will be coated with a dull black paint.

The HOYA-CM500 filter located within



Fig. 2.— Weatherproof housing units have varying levels of reflectivity due to UV yellowing in the field.

the meter should have no transmission between 730 nm and 1020 nm (?), but readings of roughly 20 mag/arcsec² were obtained for wavelengths within this range. These readings, however, required a higher source output voltage to achieve. This finding prompted further testing on the filter, outlined in section 2.2.

Table 2 provides the results from two of the six test combinations for each SQM and wavelength. In test 'A', the SQM alone collected results, whereas test 'B' included the glass filter, housing, and cover. The presence of these accessories darkened SQM readings by approximately 0.1 mag/arcsec².

The manufacturer of these devices reports a zero-point offset of up to ± 0.1 mag/arcsec² (?), which is much greater than the 95% confidence range presented in the table. Therefore, the standard deviations are not indicative of the accuracy of the measurements, but of the precision.

2.2. CM500 Filter

The filter inside of the SQM should prevent exposure to wavelengths longer than 700 nm, but laboratory results showed that near infrared sources are detected. Fig. 3 shows the standard deviation of measure-

ments taken for each of eight wavelength sources, thereby giving a measure of SQM agreement for each wavelength. Between 365 nm and 570 nm, the meters are in good agreement. The standard deviation increased when the SQMs were exposed to longer wavelengths, which prompted examination of the CM500 filter.

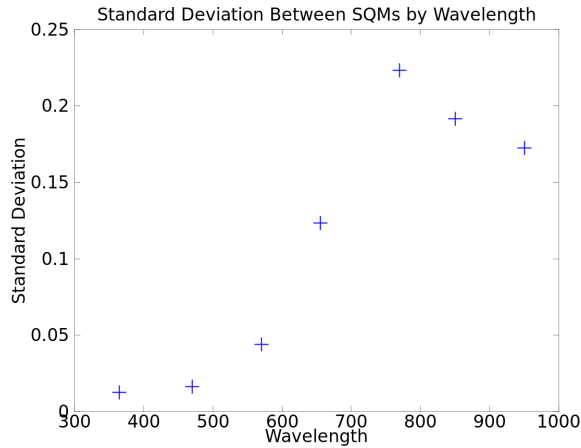


Fig. 3.— Standard deviation of readings between each SQM at each wavelength tested.

With the cooperation of the manufacturer, one of the SQMs was opened in order to inspect the filter. As seen in Fig. 4, the blue-green (square) filter is held within a plastic case; the detector would be at the top of the plastic case as shown and the lens is seen at the bottom. There is a chance that the filter is too small for the detector so that light is effectively leaking around it. The leak is made worse by the fact that the detector is tilted with respect to the optical axis. The large standard deviation between SQMs in measurements for wavelengths greater than 700nm indicates an inconsistency in the effectiveness of the filtering apparatus in each SQM.

While the manufacturer of this filter reports that the filter transmits photons between 1000 nm and 4000 nm (?), this is not

an area of concern as the SQM’s detector, a TSL237, has a spectral responsivity between 300 nm and 1100 nm (?).



Fig. 4.— Filter from inside the SQM stationed at NOAO.

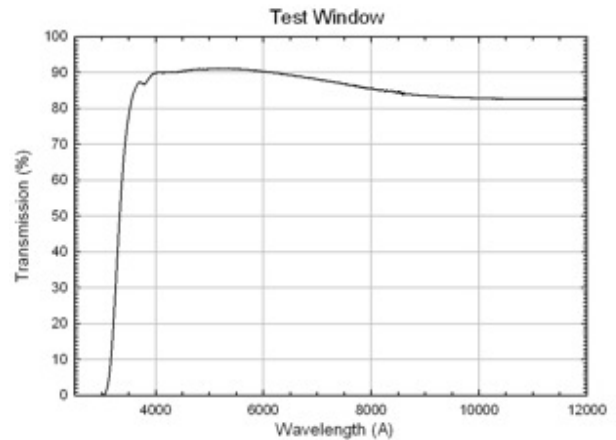


Fig. 5.— Transmission curve of the glass filter analyzed by Dick Joyce

2.3. Glass Cover Filter

Results from aforementioned testing showed that the glass filter consistently affected the light integration of the SQM. The transmission curve found for this glass cover illustrates a loss of roughly 10% around 400 nm, as seen in Fig. 5. The transmission steadily drops down to about 83% around 900 nm. Data with and without glass taken during the wavelength sen-

sitivity testing were compared and produced a trend that is in agreement with the transmission curve (see Fig. 6).

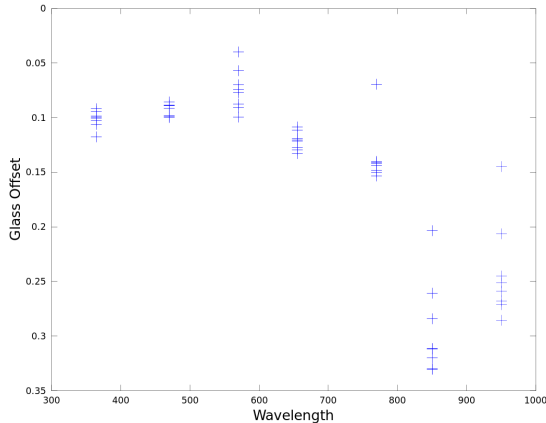


Fig. 6.— Offset between tests taken with the SQM alone and with glass covering the detector.

3. SQM Data

While the SQMs are at their respective sites, they begin collecting data every five minutes once the sky is darker than 12 mag/arcsec². The SQMs are able to accurately measure sky brightnesses as dark as 24 mag/arcsec². After the data are retrieved, they are reduced by a series of python scripts. While these newly created codes are used locally in Tucson and the surrounding areas, there is potential for implementation into a Globe at Night (GaN) GUI to assist citizen science studies in anthropogenic sky glow. After reduction, the data are analyzed for spatial and temporal trends.

3.1. Data Reduction

Each SQM reports the time a measurement was taken, the sky brightness value, the temperature, and the voltage. When

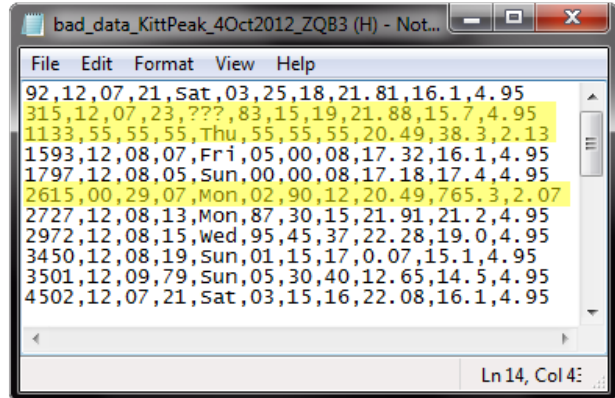


Fig. 7.— A file of faulty data from Kitt Peak.

the voltage of the device is too high, it automatically prevents the use of faulty data by replacing the data with fives (seen in the second highlighted row of Fig. 7); however, most other errors in the data are salvageable. Occasionally, the data will be saved with unrealistic years, days, hours, minutes, SQM readings, etc. Often, the errors can be identified by comparing to the lines of data recorded five minutes prior and afterwards and consequently can be fixed. Others, specifically the faulty SQM readings, must be removed from the data. The first script in the pipeline amends usable data and creates a file listing the bad data to be investigated at a later time.

Once erroneous data are fixed or removed, any remaining data taken during twilight or while the sun, moon, or Milky Way are overhead are removed via secondary scripts for analysis. This is done in order to help isolate the anthropogenic contribution to sky glow.

To assess the the validity of the reduction, and ensure that the integrity of the data is preserved, comparisons are made between the pre and post faulty measurement reduction such as in Fig. 8. These plots show the average night of each sea-

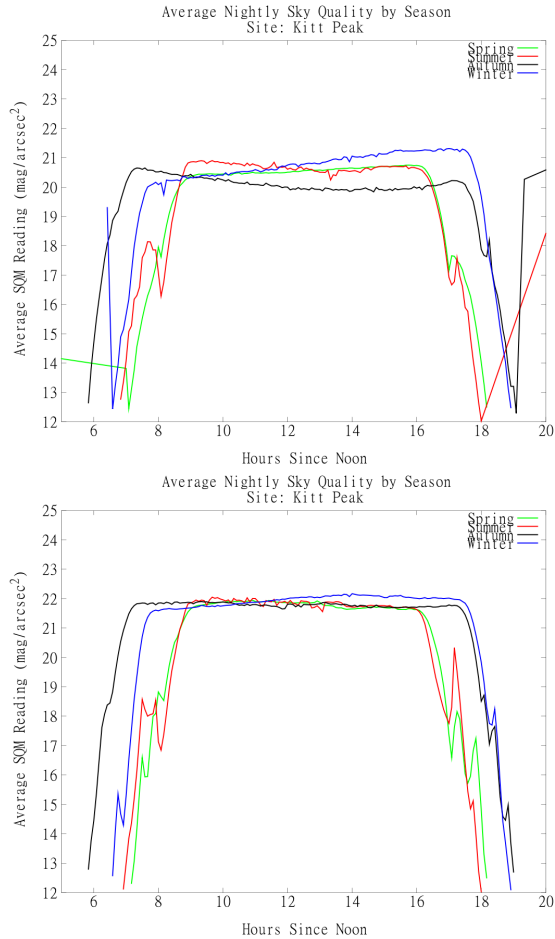


Fig. 8.— The average seasonal raw (top) and reduced (bottom) data collected from Kitt Peak

son. Fig. 8b shows the SQM measurements have much less variation after reduction.

3.2. Sky Brightness Model

To further focus on the contribution of artificial lights, twilight is removed and compared to the results of Dan Duriscoe’s sky brightness model. The National Park Service uses a silicon-based device to measure light pollution as well, and Dan Duriscoe’s model addresses the distinction between natural and artificial light pollution for this device (?). Therefore, this model provides a good representation of

light pollution measurements taken by an SQM. This model uses information about the position of the moon, Milky Way, stars, and planets based on time of an SQM reading and uses latitude, longitude, airglow, and degree from zenith to determine what the natural sky glow should be in terms of nanolamberts as well as mag/arcsec². Fig. 9 compares the average predicted natural sky brightness at Mt. Lemmon to the corresponding field data.

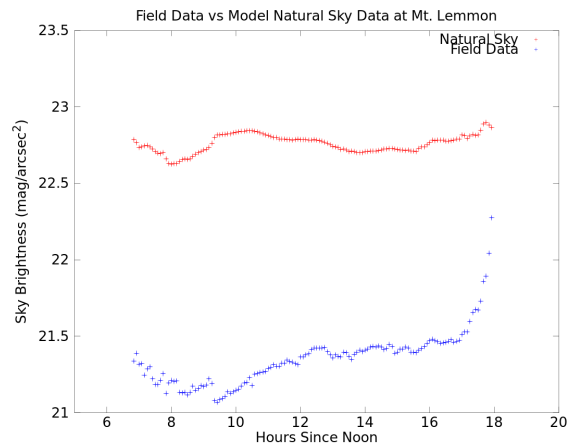


Fig. 9.— Comparison of the modeled natural sky glow (red) and the field data (blue).

As shown in Fig. 9, the anthropogenic contribution to sky glow brightens the sky by as much as 2 mag/arcsec² even when the location is as removed as Mt. Lemmon, which is over 61 km away from Tucson.

The TSL237 detector inside the SQM not strictly V band (?) and the filter inside the meter is not blocking near IR wavelengths (see Table 2). This is a problem since this model calculates sky glow based on V band sky glow. It is also important to note that this model does not account for the effect of the sun or the moon, causing the determined sky glow to be too dark during twilight and moonlight. Data taken while the moon was up and during sun or moon twilight were not included in the

comparison to the model.

3.3. Trends

Analysis of temporal trends is done by comparing data from each season, each day of the week, and each month. Further investigation is accomplished via Fourier analysis. Spatial trends are examined by comparing data from the various sites in and around Tucson. To better understand the strength of anthropogenic light contribution, the sites are put into three categories: NOAO (near the center of Tucson), Cardinal Point Sites (four SQMs located in outskirts of the city, each in a cardinal direction), and Observatory Sites (three SQMs located at observatories well outside the city of Tucson). As seen by comparing the graphs in Fig 3, artificial lighting can brighten the sky by as much as 3 mag/arcsec^2 .

To better analyze the periodic features of the sky glow in the Tucson area, a Fourier analysis is undertaken. First, nightly averages of the reduced SQM data are taken and used to generate a time series. The average of this time series is then subtracted and a Hann window function is applied with zero padding. The discrete Fourier transform is computed, and the resulting data are interpolated with a cubic spline method. Converting from the frequency domain to the period domain gives the periodograms in Fig. 11. This process is applied to both raw and reduced data sets. Most of the SQM data collection sites were established in autumn 2012 and were brought in for during the winter for recalibration. Due to the limited amount of data, the periodograms do not include periodicities greater than 50 days.

The most notable difference between these is the presence of a very strong 28 day period in the raw data, which is less

pronounced in the reduced data, illustrating the effect of the moon on sky glow. The increased power of the lunar period for the raw data at sites farther away from Tucson suggests that artificial light greatly decreases the effect of the moon relative to sky glow within Tucson. After data taken while the moon is overhead and during moon twilight are removed, the trend correlated with the moon does not completely disappear. This means that there might also be a relation to the atmospheric tidal effects of the moon. A fifteen day trend found is also correlated to moon twilight and is dependent on distance from Tucson. The fifteen day trend as well as a ten day trend are suggested by the raw and reduced Fourier transforms (Fig. 12), but it is important to note that the amplitudes of these periods are near the noise-level and there may not have significance. Averaged nights of each day of the week are also plotted to analyze variation of light pollution throughout the work week.

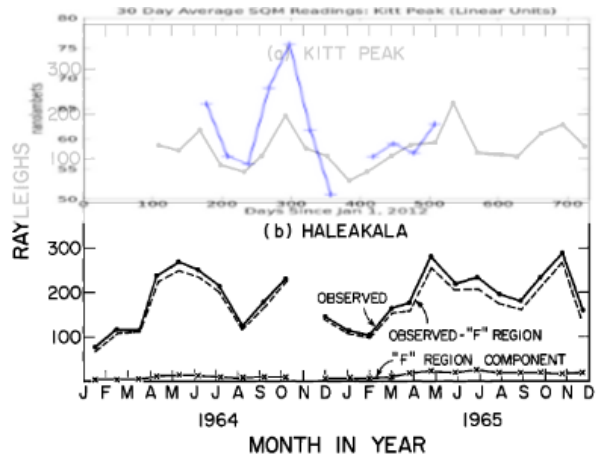


Fig. 10.— SQM data overlaying OI 557.7 nm airglow data at Kitt Peak. The SQM readings were converted to nanolamberts for better comparison to airglow intensity, which is traditionally given in Rayleighs.

Comparisons of the average night per

season are made in Fig. 3. Autumn is consistently darker in Tucson by about one mag/arcsec², but there is substantially less variation seen at the observatory sites. To examine seasonal variation in greater detail, SQM readings averaged over 30 day periods are found for the entire data set. These variations were found to correlate strongly with annual-scale variations in 557.7 nm OI airglow intensity. Fig. 10 compares 557.7 nm OI airglow data from Kitt Peak (?) with SQM data taken at the Kitt Peak site. Because the OI 557.7 nm airglow is the brightest airglow emission line in the visual range ? and the peak sensitivity of the TSL237 detector is around this wavelength, the OI 557.7 nm line is the most significant photochemical contributor to SQM readings. To obtain a more complete understanding of the role airglow plays in light pollution, future work might include comparisons to other airglow emission lines within the range of the SQM detector.

4. Conclusion

Light pollution is a source of various environmental, economic, and astronomical problems. To better understand light pollution, SQMs have been used to measure sky glow in and around Tucson since June 2012. Wavelength sensitivity tests were done with the SQMs to help interpret these data and revealed that the weatherproof housing affects the readings in a very predictable way. To compensate for how the housing affects the SQM readings, a constant offset can be added to the readings for each SQM. To minimize the needed offset, the housing will be painted in such a way as to reduce UV yellowing and internal light scatter. A less understood result of laboratory testing of the SQMs is the affect the CM500 filter has on the SQM

detector. The filter itself may lay at different angles with each SQM, and the density distribution of plastic in the casing determines what percent of light bypasses the filter altogether.

Newly written and implemented python scripts analyze and reduce the data in a consistent and repeatable way. Data taken when the moon, sun, or Milky Way is up are removed, as are data taken during twilight or moon twilight. There are future plans to implement these scripts into a GUI for the GaN light pollution campaign, in an effort to facilitate citizen science contributions to the field of light pollution study.

The anthropogenic contribution of the reduced data is measured by Dan Duriscoe's sky brightness model. The difference between the natural sky glow and the field readings (which gives a measure of the anthropogenic sky glow) is typically on the order of one mag/arcsec². This model, however, assumes a constant airglow contribution, which is not the case; the time series of data taken from Kitt Peak showed a strong long term correlation to the annual variation of the OI 557.7 nm airglow.

Several other trends were found in the light pollution in and around Tucson. Both the 28 day and the 15 day trend are correlated with the moon, though the cause of the ten day trend is unknown. Autumn is consistently darker in Tucson, but there is little variation at the observatory sites.

As more data are collected, trends and periodicities of greater length or weaker strength might be identified with greater confidence. In the meantime, due to the strong correlation of SQM data with the OI 557.7 nm line airglow intensity, other airglow contributions will be investigated - specifically the OI 630.0 nm line and the Na 587.3 nm line. Inconsistencies between

SQMs might be further investigated in the laboratory and validation of the SQM data will be pursued via comparison with VIIRS data.

λ (nm)	NOAO	East	West	North	South	Kitt Peak	Mt. Hopkins	Mt. Lemmon
365 A	20.27±0.000	20.25±0.008	20.23±0.005	20.26±0.005	20.23±0.000	20.26±0.005	20.27±0.000	20.24±0.006
365 B	20.15±0.009	20.15±0.000	20.12±0.008	20.14±0.000	20.11±0.008	20.13±0.000	20.14±0.010	20.12±0.000
470 A	19.78±0.009	19.75±0.005	19.74±0.000	19.75±0.010	19.74±0.014	19.75±0.000	19.75±0.009	19.73±0.006
470 B	19.66±0.000	19.63±0.008	19.61±0.000	19.64±0.008	19.62±0.010	19.62±0.008	19.64±0.009	19.61±0.008
570 A	18.60±0.000	18.56±0.006	18.69±0.010	18.60±0.000	18.71±0.006	18.58±0.012	18.58±0.008	18.73±0.010
570 B	18.62±0.005	18.57±0.000	18.52±0.011	18.48±0.010	18.52±0.010	18.47±0.009	18.50±0.012	18.51±0.009
655 A	19.91±0.005	19.90±0.000	20.25±0.008	20.07±0.009	19.97±0.000	20.08±0.006	20.03±0.010	20.15±0.010
655 B	19.65±0.015	19.71±0.010	20.03±0.000	19.82±0.012	19.82±0.010	19.93±0.006	19.77±0.005	19.99±0.000
770 A	19.68±0.010	19.62±0.010	20.22±0.000	19.90±0.000	19.87±0.010	19.90±0.000	19.80±0.010	20.06±0.000
770 B	19.43±0.000	19.54±0.000	20.19±0.000	19.67±0.008	19.60±0.012	19.70±0.010	19.55±0.010	19.87±0.040
850 A	20.13±0.010	20.13±0.005	20.72±0.006	20.40±0.005	20.29±0.006	20.40±0.000	20.35±0.010	20.51±0.009
850 B	19.92±0.012	19.92±0.000	20.50±0.010	20.04±0.009	20.08±0.008	20.20±0.000	20.15±0.010	20.35±0.014
950 A	20.07±0.008	20.10±0.013	20.67±0.000	20.34±0.006	20.27±0.011	20.37±0.010	20.29±0.008	20.48±0.000
950 B	19.90±0.006	20.13±0.017	20.46±0.010	20.08±0.010	20.04±0.006	20.14±0.008	20.11±0.028	20.24±0.010

Table 2: Wavelength sensitivity data for SQMs with and without glass filter and housing (A and B resp.) in mag/arcsec².

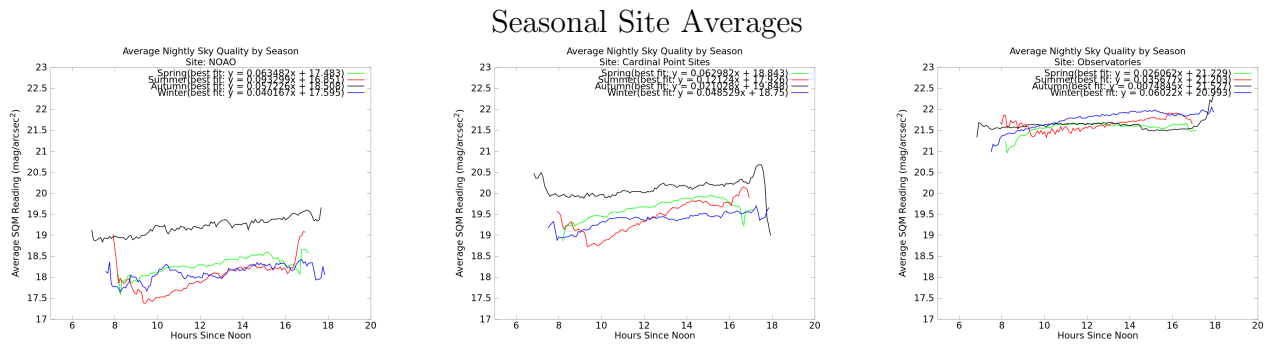


Table 3: Seasonal comparison plots of NOAO, Cardinal Point Sites, and Observatory Sites.

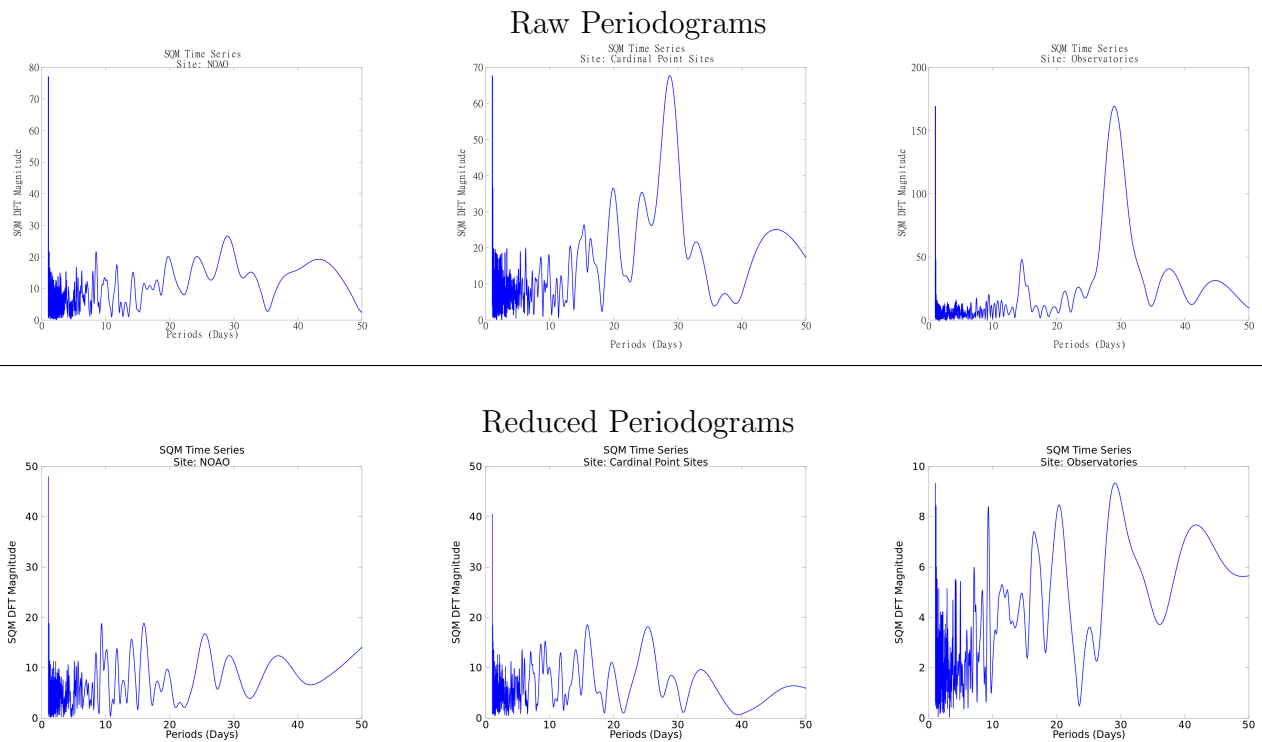
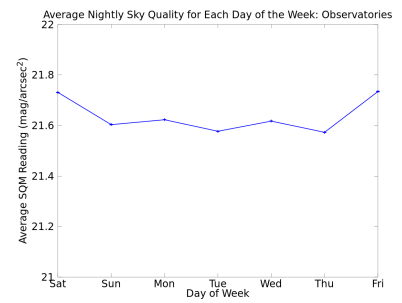
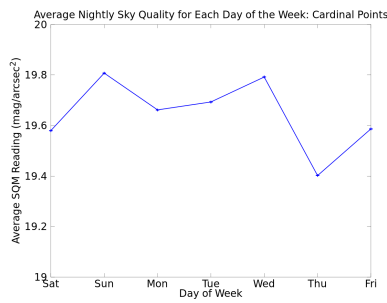
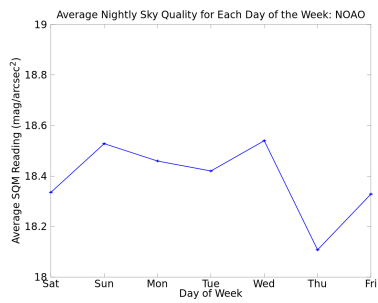


Fig. 11.— Periods in nightly averaged SQM readings at NOAO, Cardinal Point Sites, and Observatory Sites before and after reduction.

Seven Day Trends



Ten Day Trends

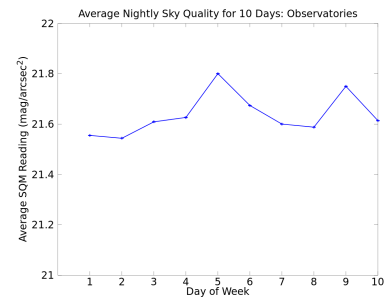
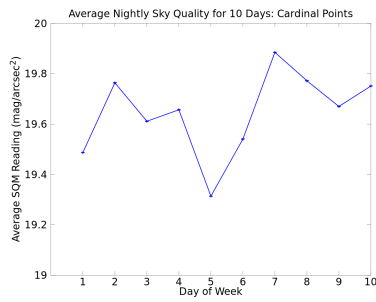
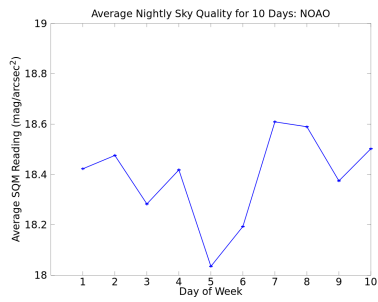


Fig. 12.— Temporal trends for NOAO, Cardinal Point Sites, and Observatory Sites.

Finding Satellite Galaxies of ESO 243-49

Rachel Smullen

KPNO REU 2013 and University of Wyoming

Advisors: Dr. Janine Pforr (NOAO)

Abstract

We present two satellite galaxies found around ESO 243-49, the host of an off-center intermediate-mass black hole. We began the search for satellite galaxies with nine Hubble Space Telescope images, extracted sources using Source Extractor, and finally, fit the type and redshift of our sources using HyperZ. Of the roughly 725 objects detected, two are identified as candidate satellite galaxies.

These identified satellite galaxies may provide insight into the nature of intermediate-mass black holes and the environments in which they form.

1. Introduction

In modern astronomy, there exists a discrepancy between stellar-mass black holes and supermassive black holes. The formation of the stellar-mass variety is fairly well understood: when massive stars collapse, if the core is large enough, a black hole may form. These can be 3-80 M_{\odot} , depending on the mass of the initial star. There exists no proven mechanism, though, to form supermassive black holes. One proposed theory is the merger of intermediate-mass black holes. The problem with this explanation: no intermediate-mass black hole has ever been confirmed. Astronomers have been looking but are unable to identify any candidates in the locations where they are expected. Therefore, the unexpected find has yielded the first potential intermediate-mass black hole.

This first candidate intermediate-mass black hole is HLX-1, located in the galaxy ESO 243-49. With an x-ray luminosity of about 10^{42} ergs/s, this object is around 400 times more luminous than can be explained with a stellar-mass black hole undergoing super-Eddington accretion (Farrell et al. 2012). Farrell proposes that this object is the cannibalized core of a dwarf galaxy with a mass of roughly 500 M_{\odot} . As this is the first intermediate-mass black hole ever found, it becomes imperative to understand the environment in which this host galaxy and its satellites have formed. Perhaps by quantifying the environment of ESO 243-49, we can identify what created this intermediate-mass black hole. We have thus searched for satellite galaxies around ESO 243-49 in the hopes of finding a unique feature that points us to the origin of HLX-1 and gives insight into the characteristics of intermediate-mass black holes.

1.1 ESO 243-49

ESO 243-49 is a S0a galaxy that lies in the Phoenix constellation. This galaxy is a member of the Abell 2877 galaxy cluster but lies toward the outer region of the cluster. It subtends roughly an arcminute of sky and lies about 92 Mpc distant at a redshift of 0.02239. Other than HLX-1, the galaxy has no notable features.

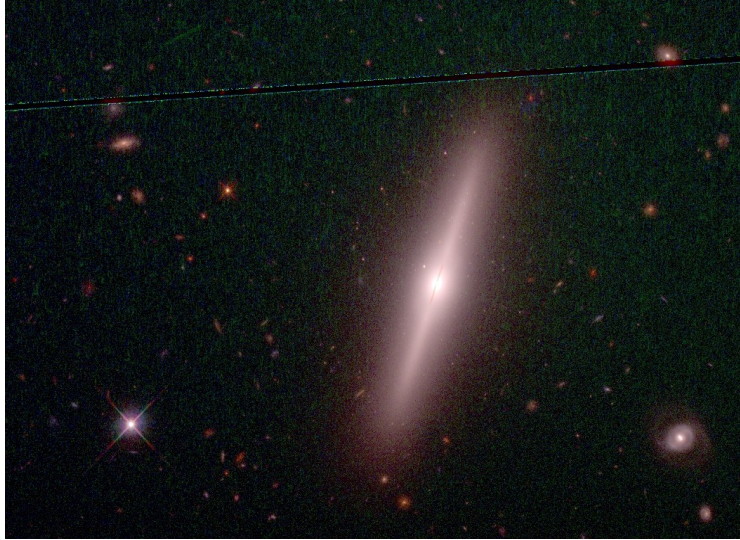


Figure 0. A three color image of ESO 243-49. Note the variety of objects in close proximity to the central galaxy.

1.2 Satellite Galaxies

As a proxy for what we might find around ESO 243-49, we looked at our own Milky Way and Andromeda. We found that there are between 14 and 26 satellites reported around the Milky Way and 32 around Andromeda (Yniguez et al. 2013). These satellites can be found from 5-400 kpc from the central galaxy and may range in mass from $10^4 M_{\odot}$ to $10^7 M_{\odot}$. Armed with this information, we can extrapolate our expected findings to ESO 243-49. Shown in Figure 1 are contours depicting a 2D distance from the centroid of the galaxy. Because of the nearness of this galaxy, we can only see out to a radial distance of roughly 30 kpc. Therefore, we are only probing the very central regions of where we expect to find satellite galaxies. We should be able to see the entire range of redshift space, around this galaxy, though, so we have the ability to find more than the four reported within 35 kpc of the Milky Way.

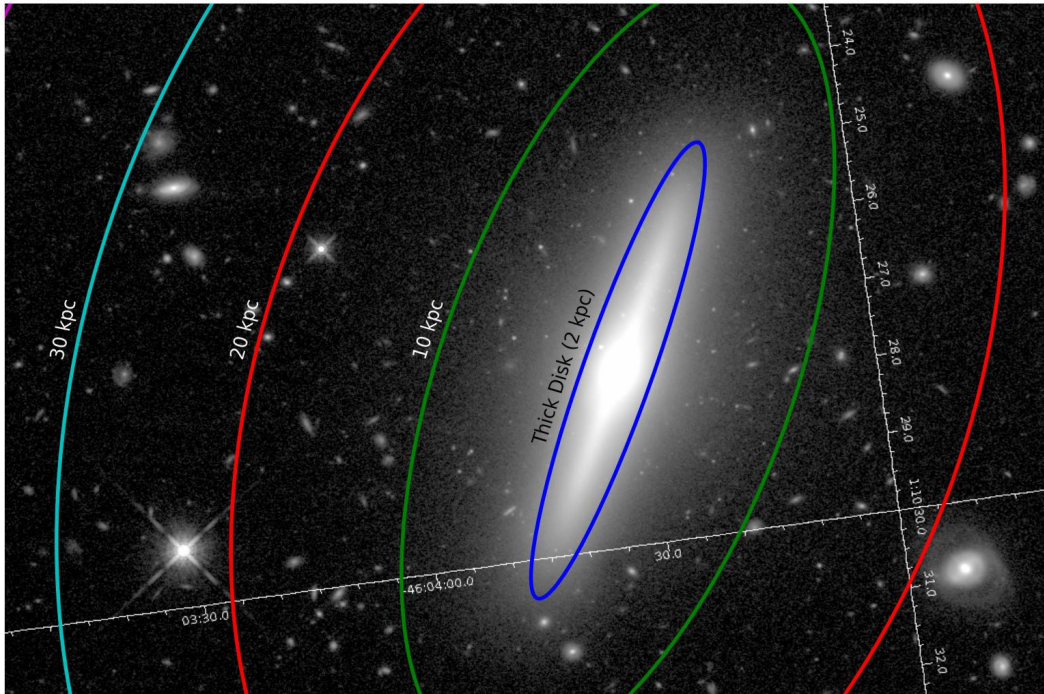


Figure 1. An image of ESO 243-49 with extrapolated distance contours overlaid. Also shown are the thin and thick disk of the galaxy.

2. Data and Reduction

We used nine images taken with the *Hubble Space Telescope* (*HST*). These images were observed in November of 2011 using the UVIS and IR detectors on WFC3. The images were centered on HLX-1 but contain roughly one arcminute of additional space to the north and south of the galaxy. Images from the F140LP, F300X, F336W, F390W, F555W, F621M, F775W, F105W, and F160W filters, listed from blue to red, were used. F140LP and F300X are far and near ultraviolet, respectively, and F105W and F160W are both near infrared images; the rest span the visible regime. All nine images, arranged from blue to red, are shown in Figure 2. Note that more objects become visible in the redder images. Also, note that there is a scale discrepancy between the infrared and visible images.

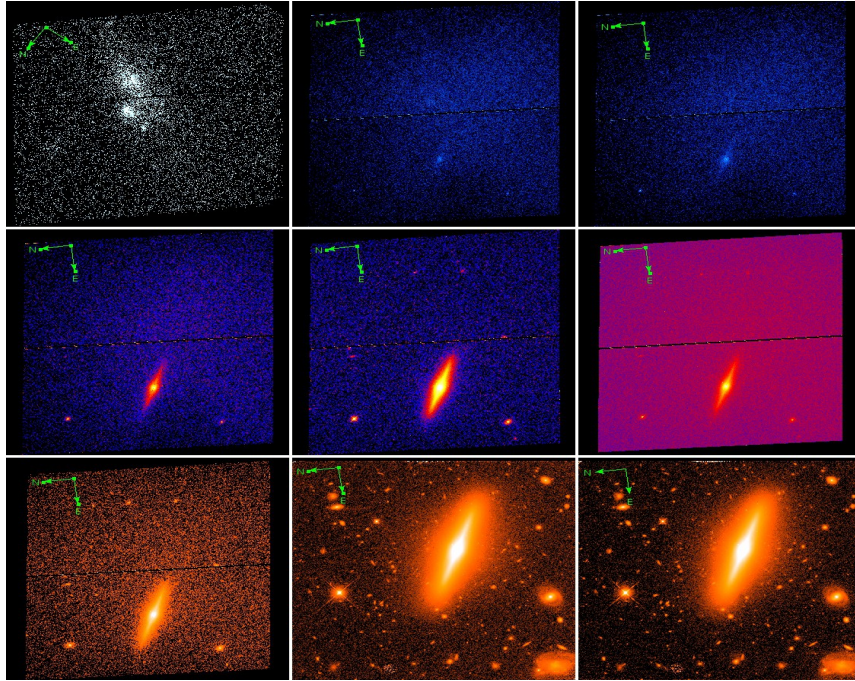


Figure 2. The nine raw images taken with HST. From left to right, top to bottom, they are F140LP, F300X, F336W, F390W, F555W, F621M, F775W, F105W, and F160W. Note that more objects become visible as the images get redder.

2.1 Astrometric Calibration

To ensure the most precision in our measurements, we first calibrated our HST images to the astrometric standards of UCAC4. We used the Gaia package of the Starlink “Namaka” release to perform these calibrations. Because our field of view is so small, we used an intermediary image taken with the ISPI imager on CTIO. This intermediary image contained enough sources that we were able to calibrate it to an absolute precision of less than $0.1''$ when compared to the UCAC4 sources. We then created a catalog of sources (both stars and galaxies) from this intermediary image and used this catalog to astrometrically align the HST images. We aligned the point sources in the ISPI image with the corresponding sources in the HST images and made minor corrections to the positions of our DRIZZLED HST images. See Farrell, et al. 2012 for a more complete description of this method. At this point in the calibration process, the two ultraviolet images, the F140LP and the F300X images, were thought to have too much of an astrometric uncertainty to be included in the final data set. Therefore, we made the decision not use them for any further steps; they did not contain enough sources to be critical to our finding satellite galaxies. The rest were calibrated such that the total astrometric error after all corrections was determined to be less than $0.15''$ for each image. This error is small enough to ensure that any aperture used in source extraction would not identify different sources in a given set of images.

2.2 Image Sizing and Smoothing

Because of the different sizes and pixel scales of our images, we were required to match all dimensions in the images before extracting sources. As the images with the smallest pixel

dimensions and largest pixel scales, the IR images became the template for the five remaining visible images. The images were trimmed to a 1057x720 size. This was the best fit rectangle for the similar regions between all images. We then used the “wregister” task in IRAF to smooth the pixel scale of all images to the 0.12825”/pixel pixel scale of the infrared images. In doing this, we conserved the flux of each source. While we may have lost some small amount of resolution on the finest scales in the five visible HST images, we were able to better fit our spectral energy distribution (SED) because of the wide extent of our wavelength coverage.

3. Source Extraction

To extract the galaxies from our image, we used the Source Extractor (SExtractor) package from Emmanuel Bertin (1996). We used SExtractor in dual image mode, meaning that one image was used for aperture detection and those apertures were then used to extract fluxes for the second image. We determined that the infrared F160W images were the best detection images to use, as they contained over 200 more sources than any other image in our data set.

3.1 Hot and Cold Detection

We adopted a method used by the CANDLES team to extract our sources: the “hot” and “cold” detection method (see Galametz et al. 2013 for a full description of this process). The “hot” detection is optimized to detect small, faint objects. With this, we were able to find apertures for the multitude of small objects around the galaxy. Unfortunately, the hot detection is so sensitive that it will break up extended sources into multiple apertures. For instance, the spiral arms of galaxies are often detected separately from the central region, as shown below in the left hand panel of Figure 3. This destroys the information about the total flux coming from an extended galaxy. To overcome this problem, we used a “cold” detection optimized to detect bright extended sources as a single source. The cold detection, though, does not have enough sensitivity to detect the small, faint, high-background objects in close proximity to the galaxy. Therefore, the combination of hot and cold detections provides a full sampling of the variety of objects found in our images. As a final step, we combined the catalogs of the two detection types to eliminate doubly-counted sources.

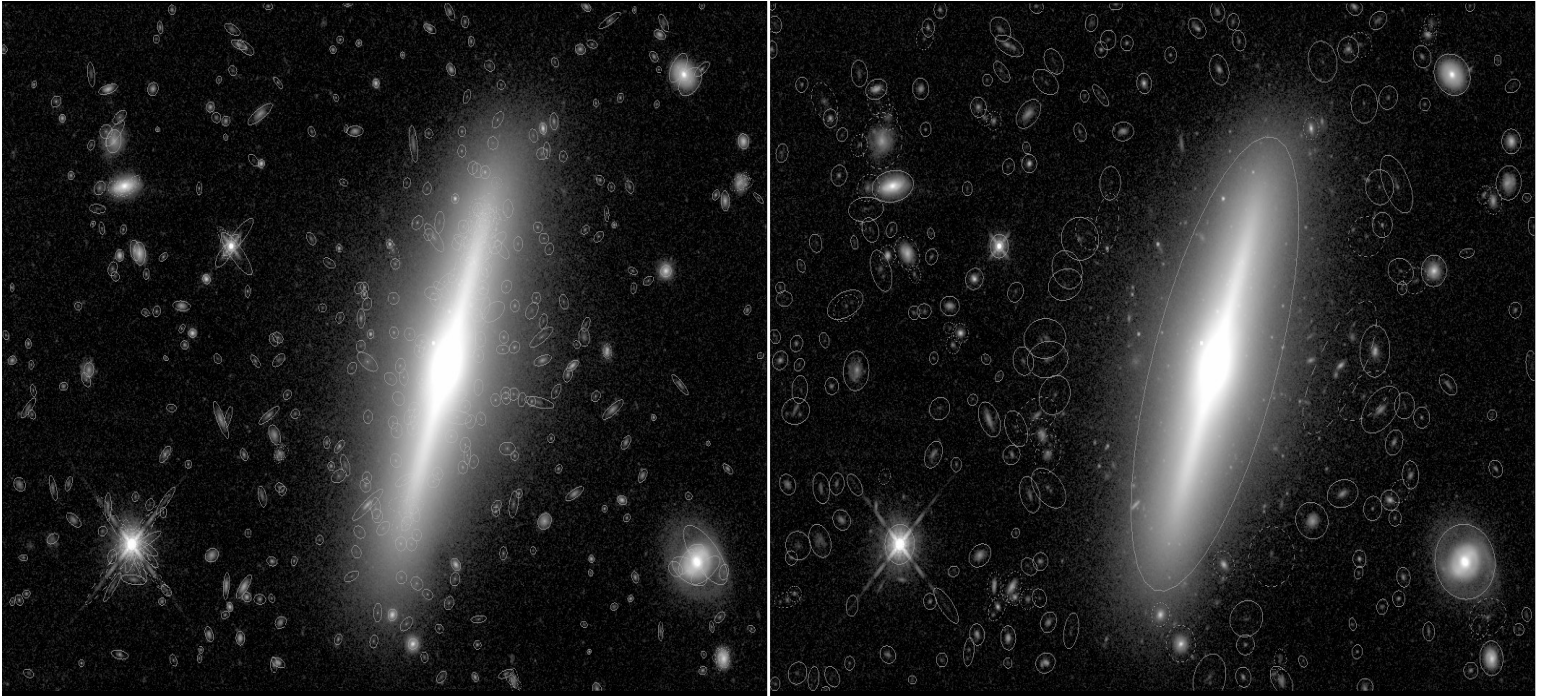


Figure 3. Hot (left) and cold (right) detections of the F160W images of ESO 243-49.

4. SED Fitting

Once all sources were detected and our combined catalog was created, we fit galaxy types and distances using the HyperZ photometric redshift package. We used synthesized templates from Pforr 2012 to fit the parameters of the catalog. We input our catalog of 724 objects and received an output containing best fit galaxy types, redshifts, and ages at the 99%, 90%, and 68% confidence levels. The results, color coded by redshift, are shown in Figure 4 below. We did attempt a comparison with the EAZY photometric redshift package, but we did not find physical results.

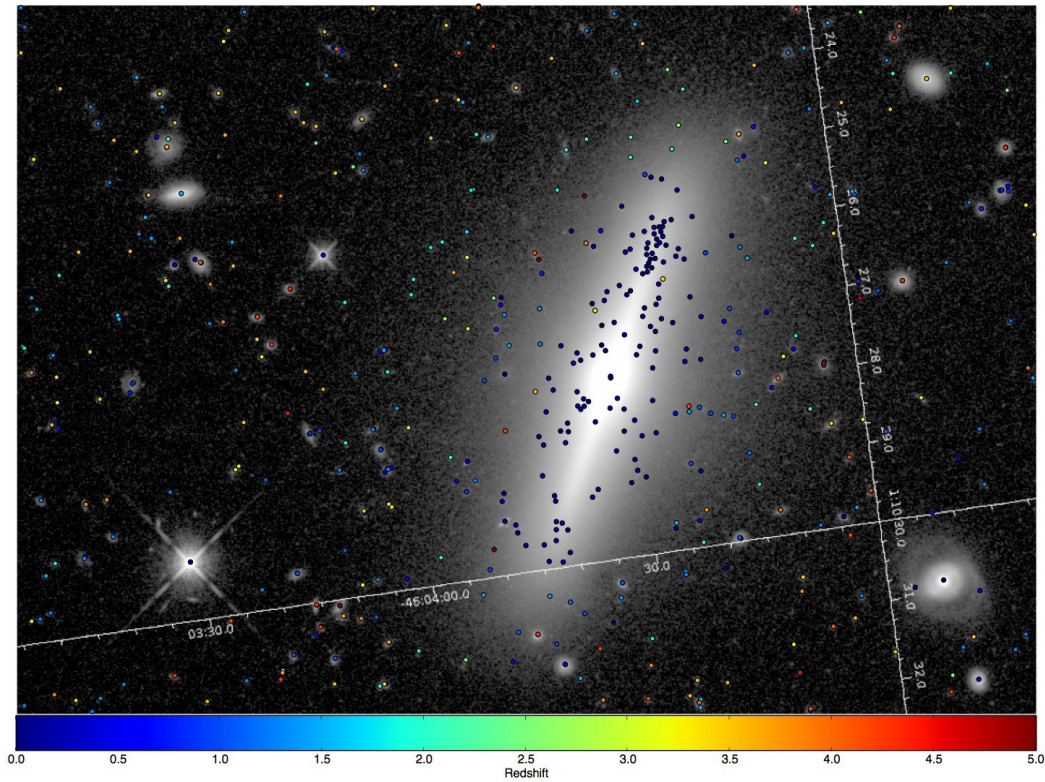


Figure 4. All detected objects color coded by best fit redshift.

4.1 Object Elimination

To reduce our objects from the entire catalog to those that might be satellite galaxies, we first removed all objects that lay within the thick disk of the galaxy. While there may be satellite galaxies within this region, the objects within are swamped by the high background of the galaxy and are therefore inherently uncertain. We also eliminated all objects whose reported redshifts did not overlap with the reported redshift of ESO 243-49 at $z=0.022395$. We were left with the roughly 500 objects shown below in Figure 5. In this image, yellow corresponds to a 99% confidence level, cyan to a 90%, and magenta to a 68%. We then sequentially narrowed the width of our confidence interval until we were left with only two objects. If we narrowed our confidence width any more, we were left with no objects at the approximate redshift of our galaxy. Our final confidence width was $\Delta z=0.1$. While wide in absolute redshift space, this width is less than three times the absolute minimum error on photometric redshifts reported by HyperZ.

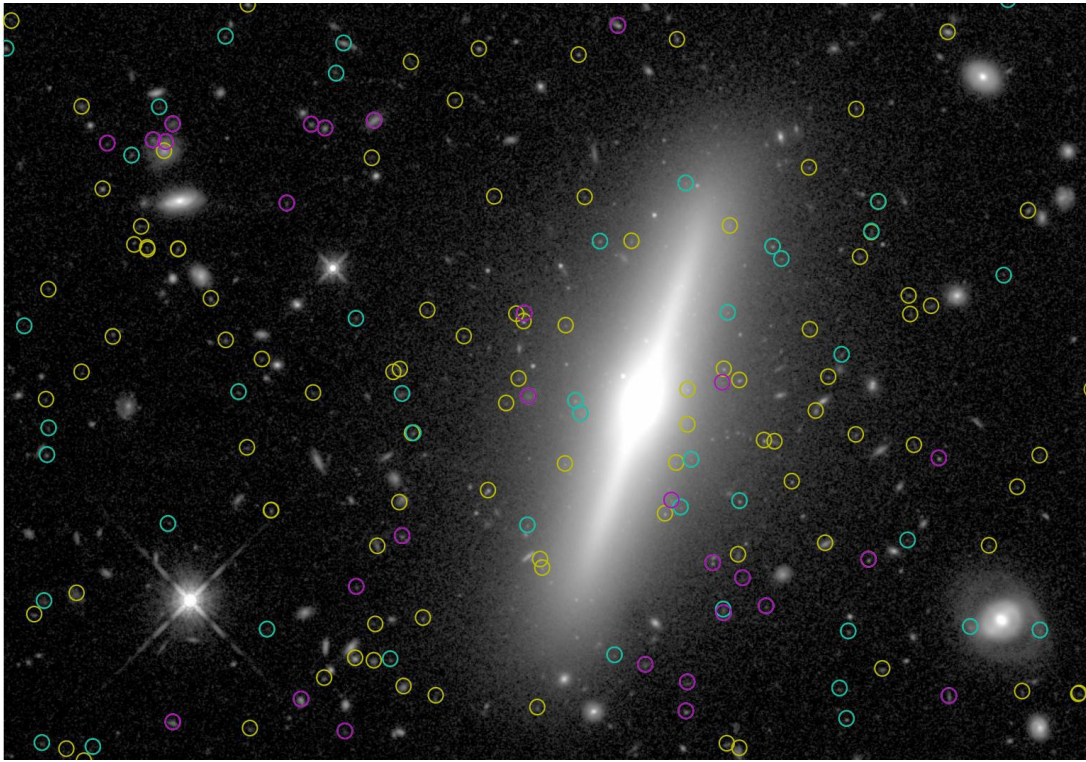


Figure 5. Confidence levels for those objects overlapping with the redshift of the central galaxy. Yellow corresponds to a 99% confidence level, cyan to a 90%, and magenta to a 68%.

5. Results and Conclusions

We found two satellite galaxies, shown below in Figure 6. Both of objects these have uncertainty widths less than $\Delta z=0.1$. We have termed the galaxy to the upper left Object 11 and the galaxy to the lower left Object 321.

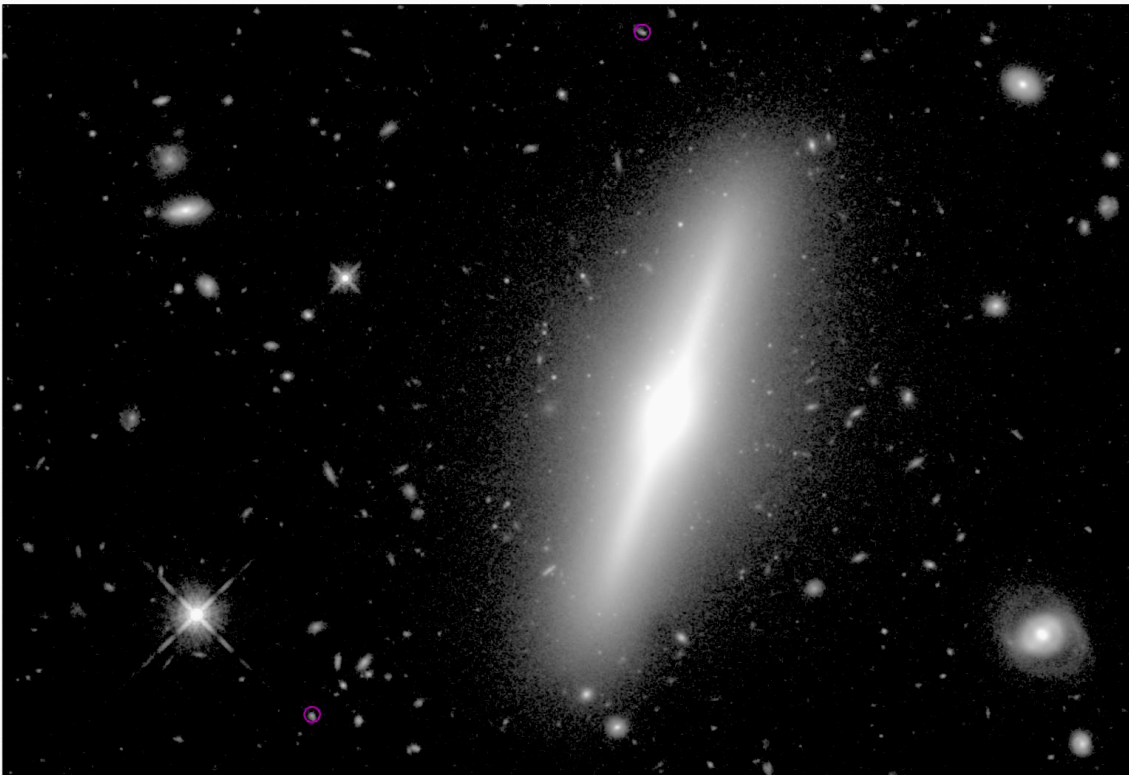


Figure 6. The two satellite galaxies we found. The objects are circled in magenta and found to the upper and lower left of ESO 243-49.

5.1 Object 11

This object lies to the southwest of ESO 243-49. A zoomed image and the best fit SED are shown in Figures 7 and 8. This object has a measured redshift of $0.0504 +0.0536/-0.0344$. Also, HyperZ reported an age of 0.3602 Gyr and a stellar mass of $10^{7.2} M_{\odot}$. These are both consistent with what we expected to find in a satellite galaxy, per Yniguez et al. 2013. The best-fit SED of this galaxy shows a galaxy with a rise in flux in the blue part of the spectrum. This feature is normal to a star-forming galaxy, which might suggest that this object underwent a recent interaction with ESO 243-49. In addition, the galaxy itself shows a more elongated shape, which may be indicative of an infall if this object truly is a satellite galaxy.



Figure 7. A zoomed image of Object 11.

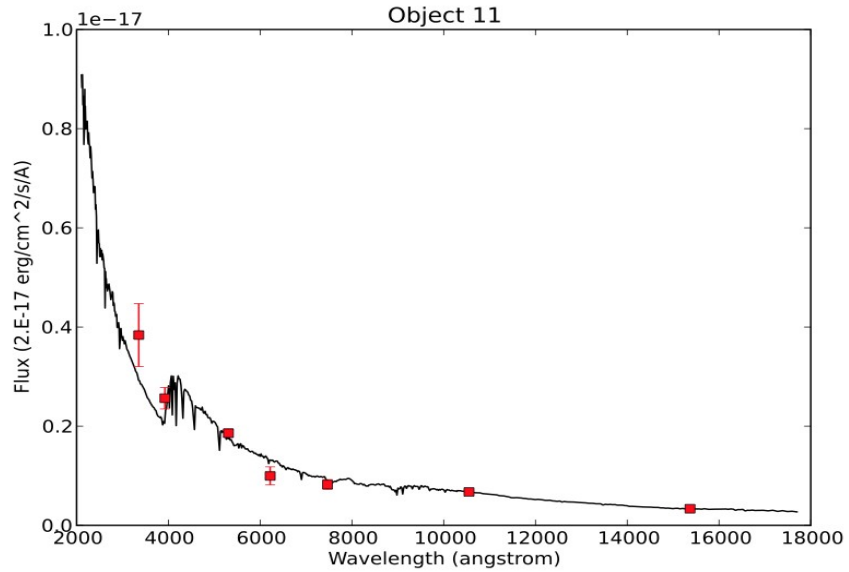


Figure 8. The best fit SED of Object 11. The red points are the measured fluxes fed into HyperZ.

5.2 Object 321

Object 321 lies to the southeast of ESO 243-49. A zoomed image and the best fit SED are shown in Figures 9 and 10. This object has a measured redshift of $0.0168 \pm 0.0551 / -0.0168$. Also, HyperZ reported an age of 0.8064 Gyr and a stellar mass of $10^{6.1} M_{\odot}$. This object has the same best-fit SED as Object 11: it shows a spate of recent star-formation. The morphology of this object is standard for a small galaxy: it looks more like a blob than anything else.

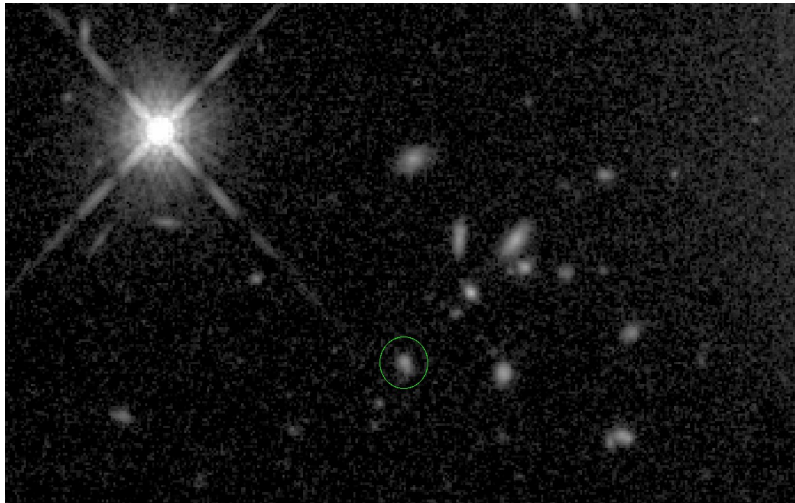


Figure 9. A zoomed image of Object 321.

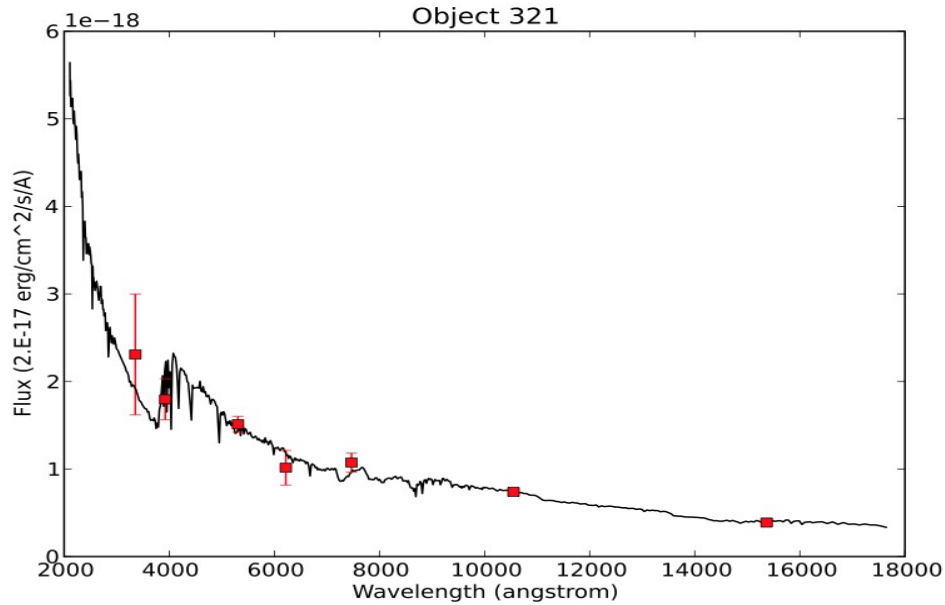


Figure 10. The best fit SED of Object 321. The red points are the measured fluxes fed into HyperZ.

5.3 Conclusions

In conclusion, we find two potential satellite galaxies around ESO 243-49. We find comparable numbers and characteristics of satellite galaxies around this galaxy when compared to similar regions of the Milky Way. Unfortunately, our two satellites have errors so large that we cannot conclusively state that these are actually satellite galaxies. Therefore, we require more follow up observations to confirm the redshift of the objects. Also, we would like to probe the outer regions where we should find satellites to gain a more complete census of the satellite population around ESO 243-49. Doing this might suggest a reason for the existence of the intermediate-mass black hole candidate, HLX-1, and provide more detailed insight into the formation of satellites and their central galaxies.

References

- Bertin E., Arnouts S., 1996, A&AS, 117, 393
- Farrell S. A. et al., 2012, ApJ, 747, L13
- Galamez, A., Grazian, A., Fontana, A., et al. 2013, ApJS, 206, 10
- Pforr J., Maraston C., Tonini C., 2012, MNRAS, 422, 3285
- Yniguez, B. et al., 2013, MNRAS, submitted